Electroabsorption Investigations of Advanced Polymer Light-Emitting Diodes

Vladimir Bodrožić

A dissertation submitted for the degree of Doctor of Philosophy at the University of London

University College London

August 2005

ProQuest LLC
789 East Eisenhower Parkway
P.O. Box 1346
Ann Arbor, MI 48106-1346

Abstract

In this thesis we employ electroabsorption (EA) spectroscopy in the study of encapsulated blue polymer light-emitting diodes (PLEDs), introduced generally in Chapter 1, that also incorporate a hole injection layer, poly(3,4-ethylene dioxythiophene) doped with poly(styrene sulfonate) (PEDOT:PSS). In addition to providing valuable information about the polymer film, EA, described in Chapter 2, allows the probing of the built-in voltage, V_{BI}, generated through the equilibration of the chemical potential across the PLED heterostructure. Typically, V_{BI} is measured by applying a voltage of the form $V = V_{dc} + V_{ac}\sin(\omega t)$ across the diode, and finding V_{dc} (or V_{null}) at which the EA signal vanishes. In Chapter 3, apart from describing our EA experimental set-up, we measure the EA response of a simple one-layer PLED (without PEDOT:PSS), and find full agreement between the experimental results and the Stark theory. In devices with PEDOT:PSS (Chapters 4-6), the Stark electroabsorption signal is mixed with a smaller intensity signal, not predicted in the Stark effect. In some devices, this causes deviation from the expected behaviour, for example by introducing V_{null} dependence on the photon energy and on ac frequency. Although this poses a potential problem for accurate V_{BI} measurements, the effect is minimal at energies near the Stark response peak and high frequencies, which makes the measurement of V_{BI} possible. We also consider the origin of the 'other' signal, and present evidence which strongly suggests that it is generated by trapped charge at the PEDOT:PSS/emitting-polymer interface. We use V_{BI} measurements to probe energy level alignment across the PLED heterostructure, in a series of devices which vary only in the composition of the emitting polymer layer. Our results, which show that V_{BI} is polymer dependent, in full account with the theory of alignment of the chemical potential across the PLED heterostructure, suggest Fermi level pinning to the polymer bipolaron levels. Finally, we investigate the effects of electrical driving on these devices, and find strong evidence for degradation of PEDOT:PSS (particularly near the interface) and its work function, in full agreement with the available literature.

Acknowledgements

I would like to thank my supervisors Dr. F. Cacialli and Dr. N. Skipper, and other members of the UCL Condensed Matter Group, especially Dr. A. H. Harker, Dr. A. Kerridge, Professor A. J. Fisher, Professor A. M. Stoneham, for their help and guidance during the course of this work. I would also like to thank Dr. M. Roberts of Cambridge Display Technology (CDT), for providing polymer light-emitting diodes, and for helping me during my visit to CDT. I am also grateful to other members of the CMMP group in UCL, who have made my stay more enjoyable, especially to L. Parrot, O. Fenwick, Dr. A. Downes and C. Bird. I also wish to thank Dr. Daren Caruana of the UCL Department of Chemistry for his help with the cyclic voltammetry experiments, and Dr. John de Mello from the Department of Chemistry in Imperial College London for his explanation of modulation of the trapped charge density at the PEDOT:PSS-polyfluorene interface.

Most of all, I would like to thank my parents, to whom I dedicate this work.

I confirm that the work presented in this thesis is my own. Where information has been derived from other sources, I confirm that this has been indicated in the thesis.

Contents

List of Figures

List of Tables

Chapter 1

An Introduction to Semiconducting Conjugated Polymers and Polymer Light-Emitting Diodes

We begin this thesis by introducing the reader to conjugated polymers and polymer light-emitting diodes (PLEDs). The chapter begins with an outline of prominent historical landmarks that have led to PLED development. We then provide a more detailed description of conjugated polymers, accounting for concepts such as energy gap, solitons and polarons. The discussion is first centred on the archetypal conjugated polymer trans-polyacetylene, and then extended to polyparaphenylene, which is more typical of currently-used light-emitting polymers. We then focus on the basic physical processes governing PLED operation, such as charge injection and light emission. We discuss the relevance of the metal-semiconductor interface in controlling PLED currents, together with other factors that govern PLED efficiency. Lastly, the chapter concludes with an outline of the rest of the thesis.

1.1 Background of Polymer Light-Emitting Diode (PLED) Technology

It has been reported[1] that the first observed electroluminescence ('the generation of light by electrical excitation other than black-body radiation'[2]) in organic materials was made by Bernanose[3] in the 1950s, who applied a high-voltage alternating current to thin crystalline films of acridine orange and quinacrine. A more widely cited report is that of Pope *et al.*[4], who in 1963 reported electroluminescence from anthracene single crystals. Electrical conduction in conjugated polymers was discovered in 1970s[5], leading to a surge of interest in conjugated polymers. In 1983, R.H. Partridge of the National Physical Laboratory in the UK reported the first electroluminescent polymer devices, based on poly(N-vinylcarbazole) (PVK), that emitted blue light visible in artificial room lighting conditions[6]. However, owing to the poor electron injection and transport characteristics, luminance was very low and the results did not attract much attention[7]. Then, in 1989, following the fabrication of small-molecule organic light-emitting diodes few years earlier by Tang *et al.*[8], Burroughes *et al.*[9] developed the first conjugated polymer-based PLEDs, using poly(phenylene vinylene) (PPV). This opened a flood of research in the field, in both academia (interested in investigating the physics behind PLEDs), and in industry (attracted by the PLEDs' potential for developing cheap but high-performance displays)[10,11].

Over the last fifteen years, considerable progress in understanding the PLED physics has been achieved, leading to improved brightness, efficiency and durability of the devices, with some products, such as those shown in Figure 1.1[12], already able to compete with the traditional inorganic technology. The principal advantage of PLED displays is the reduced manufacturing process complexity, and the resulting lower cost of the commercial products[2,13]. In addition, polymer films are intrinsically flexible, less prone to breakage, and may eventually lead to the development of thin flexible displays[14]. Another advantage is that polymers can be synthesised from a wide variety of chemical species, chosen to obtain a specified set of physical

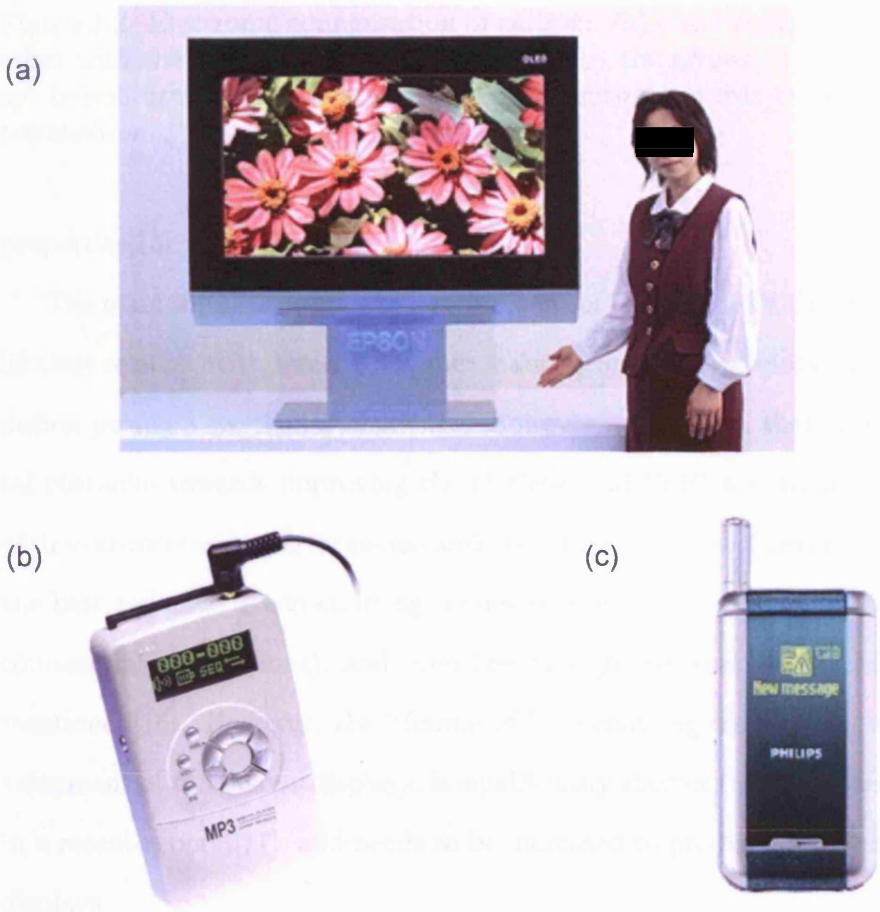

Figure 1.1: Examples of displays based on organic light-emitting diodes (OLEDs)[12]: (a) 40 inch full colour OLED display prototype produced by Seiko Epson Corporation, (b) MP3 music player launched by Delta Electronics incorporating a green PLED display, (c) mobile telephone from Philips with an organic display.

Figure 1.2: Electronic configuration of carbon: (a) outer energy levels of a single C atom with the electron occupancy indicated by the arrows, b) a sketch of the four sp^3 hybrid orbitals of a C atom, each one pointing towards the corner of a regular tetrahedron.

properties[15].

The main limitations for the development of full-colour PLED-based displays are lifetime related, with limited polymer stability and susceptibility to electrical degradation posing a particular challenge. However, at present, there are no fundamental obstacles towards improving the lifetime, and PLEDs continue to be developed with ever-increasing performance and operating lifetimes. Currently, the lifetime of the best red- and green-emitting diodes is in excess of 10,000 hours (sufficient for commercial applications), and even lifetimes greater than 40,000 hours have been mentioned[16]. However, the lifetime of blue-emitting diodes, required for the development of full-colour displays, is significantly shorter (for instance, $\sim$ 4000 hours in a recent report)[17], and needs to be increased to produce competitive full-colour displays.

1.2 Semiconducting Conjugated Polymers

1.2.1 Basics of Carbon Bonding

The chemistry of light-emitting polymers, and organic molecules in general, is based on the covalent bonds between the carbon atoms, whose ground state electronic configuration is $1s^2 2s^2 2p^2$. In the simplest of organic molecules, methane (CH_4), one C(2s) and three C(2p) orbitals are mixed to form a set of four equivalent degenerate hybrid orbitals, sp^3, arranged in a tetrahedral arrangement, as illustrated in Figure

1.2[18]. Each hybrid orbital contains a single electron, paired with one H electron.

In ethene (C_2H_4), each carbon atom forms three sp^2 hybrid orbitals, in which one C(2s) and two C(2p) orbitals are mixed[18,19]. The axes of all three orbitals lie in a single plane, and the axes of the third p orbital ($2p_z$) not included in the hybridisation, is perpendicular to the plane. The sp^2 orbitals have a rotational symmetry around the internuclear axis, and, since they resemble an s orbital when viewed along the internuclear axis, are called σ-orbitals (σ is the Greek equivalent of s)[18]. Similarly, a $2p_z$ orbital, which when viewed along the internuclear axis resembles a p orbital, is called a π-orbital. π-orbitals are characterised by delocalisation of electronic charge, whereas σ-orbitals in contrast are highly localised[20]. Because they have different symmetry properties, it follows from group theory that the overlap and Hamiltonian matrix elements between these two sets of orbitals are zero[19]. In other words, σ- and π-orbitals are non-interacting and can to a good approximation be considered independently of one another[19]. In ethene, both sets of orbitals interact with the corresponding orbital on the neighbouring carbon atom, forming the bonding (symmetric) and the antibonding (antisymmetric) σ- and π-orbitals, as illustrated schematically in Figure 1.3(b). In a π bonding orbital, the charge is concentrated between the nuclei, so that it attracts the nuclei and holds them together, as shown in Figure 1.3(a). A bonding orbital has a minimum in the energy versus nuclear separation curve (see Figure 1.3c). In contrast, in an antibonding orbital the charge density is minimal between the nuclei, and nuclei tend to repel one another (no minimum in the energy curve in Figure 1.3c). In ethene, and in π-bonded molecules in general, the energy gap E_g between bonding and antibonding orbitals in the σ-system is significantly larger than in the π-system. As a result, electrical and optical properties of π-bonded molecules are largely determined by π-bonded electrons. The role of the strongly bonded σ-electrons is to keep the molecules intact[21].

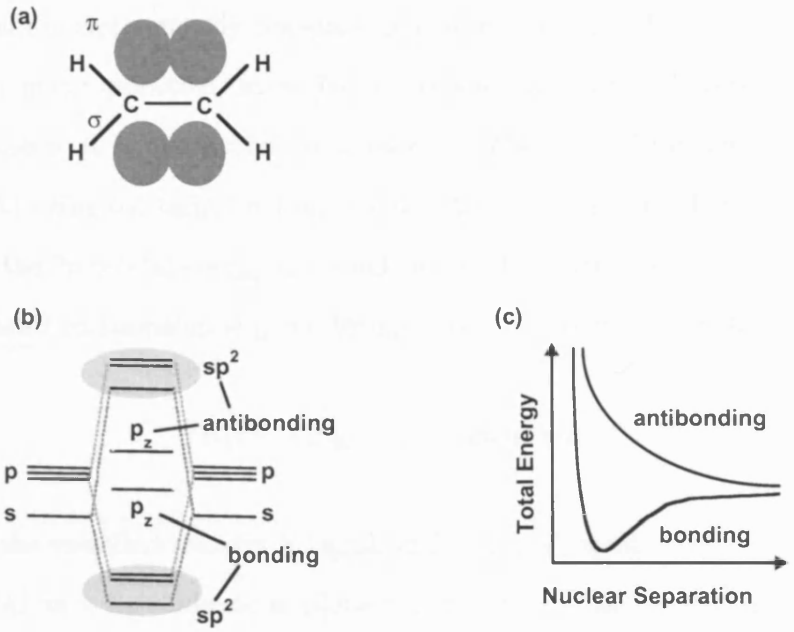

Figure 1.3: Sketch of chemical and electronic structure of ethene: (a) The shape of the π bonding orbital is indicated. (b) Schematic diagram of the bonding and antibonding $\sigma-$ and $\pi-$ energy levels. (c) Total energy versus nuclear separation of a bonding and an antibonding orbital.

Figure 1.4: (a) Chemical structure of trans-polyacetylene. (b) A one-dimensional chain of p_z orbitals spaced a apart.

1.2.2 Trans-Polyacetylene

The archetypal conjugated polymer is trans-polyacetylene (t-PA), whose chemical structure is shown in Figure 1.4(a). The term conjugated refers to the alternating sequence of single and double bonds shown in the structural representation[20]. As in ethene, the outer shell carbon electrons are sp^2-hybridised, with one p_z electron per carbon atom. Each carbon atom is σ-bonded to two neighbouring carbon atoms, and to one H atom.

In a t-PA film, electronic and optical properties of individual chains are usually preserved because of strong intrachain bonding and weak interchain interactions[22].

A t-PA chain is electronically one-dimensional in nature, and π-electrons are delocalised over many monomer units. To understand its energy (E) versus wavevector (k) relationship, it is instructive to consider its *E(k)* vs k dependence obtained in appendix A1 using the tight binding model[22,23]. If the spacing between the atoms is a, and if the 2p orbital energy in a single isolated C atom is E_{pz}, the energy versus the wavevector relationship is given by equation 1.1 (see appendix A1):

$$E(k) = E_{pz} - \beta - 2t\cos(ka), \tag{1.1}$$

where t is the so-called transfer integral, and β is a constant.

The *E(k)* vs k dependence is plotted in Figure 1.5, in the first Brillouin zone ($-\pi/a \leq k \leq \pi/a$). Since each Brillouin zone contains the same number of k-states as the total number of primitive unit cells, for a chain of N atoms, with the size of a primitive unit cell equal to a, the first Brillouin zone contains N k-states. Thus, in t-PA, which has one carbon atom per primitive unit cell (despite its zig-zag structure)[24], there are N π-electrons in a chain of N atoms. Since every k-state can accommodate 2 electrons, the bonding states (corresponding to the bottom half of the k-states in Figure 1.5) can accommodate all the p_z electrons.

In this case, the band would be precisely half-filled and t-PA would be a metal. However, due to the existence of an energy gap at the edge of the Fermi distribution, t-PA behaves as a semiconductor. The energy gap opens up due to Peierls distortion (which we next discuss), and the simultaneous presence of a Mott-Hubbard transition[7] (not discussed here as it is not within the scope of this thesis).

1.2.3 Peierls Distortion[22,23,25,26]

According to Peierls's theorem, a one-dimensional metal with a half-filled band can lower its energy by doubling the size of its primitive unit cell[25]. In the case of t-PA, this can occur by the displacement of each carbon atom by $u_n = (-1)^n|u_0|$, where n is the atom number, and u_0 is the amount of displacement in the chain direction. This means that every atom moves by the same amount along the chain axis, but in the opposite direction to its nearest neighbours, as indicated in Figure 1.6(b).

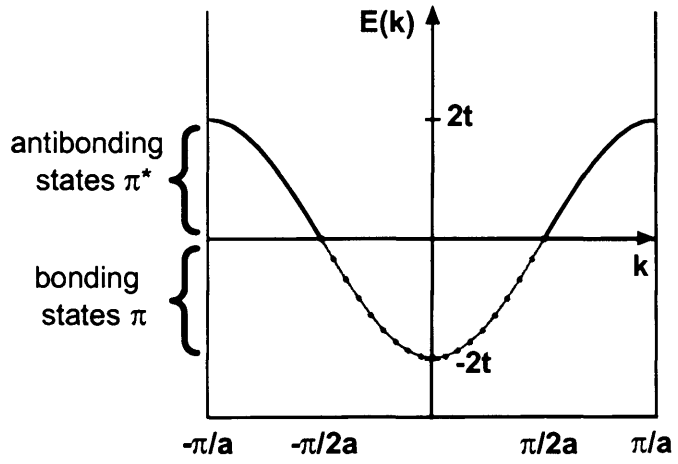

Figure 1.5: Energy versus wavevector of a one-dimensional chain of atoms, derived using the tight binding model. For one electron per primitive unit cell, the band is exactly half-filled, with filled states marked in red. ($E_{pz} - \beta$ is taken to be zero in energy.)

As a result, the Brillouin zone becomes halved, so that it lies in the range $-\pi/2a \leq k \leq \pi/2a$. This is illustrated in Figure 1.6(a), where $E(k)$ vs k dependence with the Peierls distortion is depicted by the full line, and, for comparison, the dependence without the distortion is indicated by the broken line. The two curves are similar near $k = 0$, but as k approaches the Brillouin zone edge ($\pm\pi/2a$), dE/dk of the full line tends to zero, so that an energy gap (E_g) opens up at the edge of the Fermi distribution. Near $\pm\pi/2a$, π-orbitals are concentrated in the region towards which the positively charged C atoms are drawn, so that, due to electrostatic interaction, π-orbitals are lowered in energy. Conversely, π*-orbitals are concentrated away from this region, resulting in an increase of π*-orbital energy. This leaves the completely filled π band (full red line), separated in energy from the completely empty π* band (full black line). Note that as carbon atoms are displaced, an equilibrium is established between the forces acting to lower π-electron energy, and the forces acting to reduce the elastic energy stored in σ-bonds. At equilibrium, C bonds in t-PA (1.22 Å long[23]) are distorted by 0.03 to 0.04 Å[22].

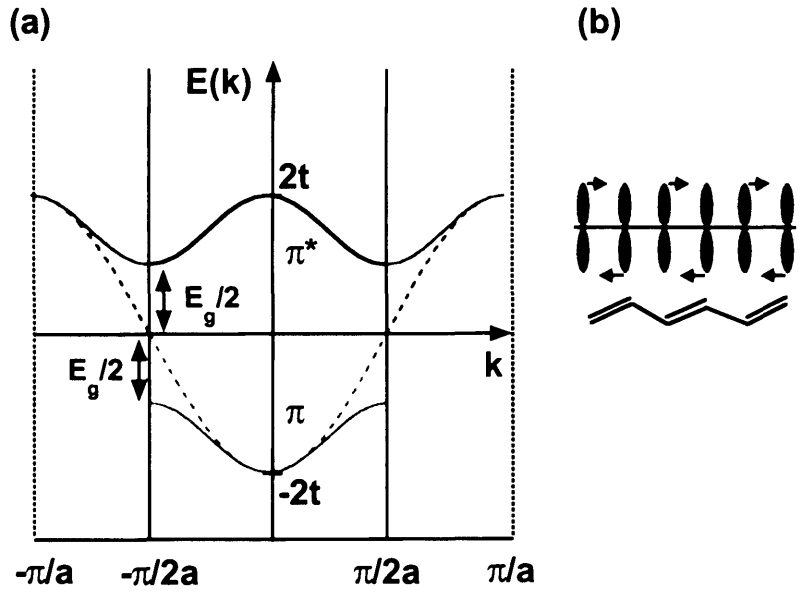

Figure 1.6: (a) Comparison of the energy vs the wavevector dependence with (full line) and without (broken line) Peierls distortion[22,25]. The Brillouin zone is halved after Peierls distortion, and lies in the range $-\pi/2a \leq k \leq \pi/2a$. (Again, $E_{pz} - \beta$ is taken to be zero in energy.) (b) The distortion in t-PA occurs by shifting of C atoms along the chain, as indicated by the arrows.

1.2.4 Non-Degenerate Conjugated Polymers: Polyparaphenylene

Conjugated polymers can be classified either as degenerate or non-degenerate, depending on whether the total energy at the two values of the displacement parameter ($-u_0$ and u_0) is the same or different respectively, as illustrated in Figure 1.7. Apart from t-PA which is degenerate, virtually all other conjugated polymers are non-degenerate[24].

Here, we consider polyparaphenylene (PPP), which is an archetypal non-degenerate polymer, with structure closely related to that of polyparaphenylene vinylene (PPV), and poly(9,9-dioctylfluorene) (F8), which (together with their derivatives) are among the most widely used light-emitting polymers. The common structural component in these polymers is the benzene ring, from which the basic arrangement of the polymer energy levels, as well as the energy gap, is derived. In benzene, carbon atoms are sp^2 hybridised, with one p_z orbital per C atom. Each C atom is σ-bonded to two neighbouring C atoms, forming a hexagonal arrangement, as shown in Figure

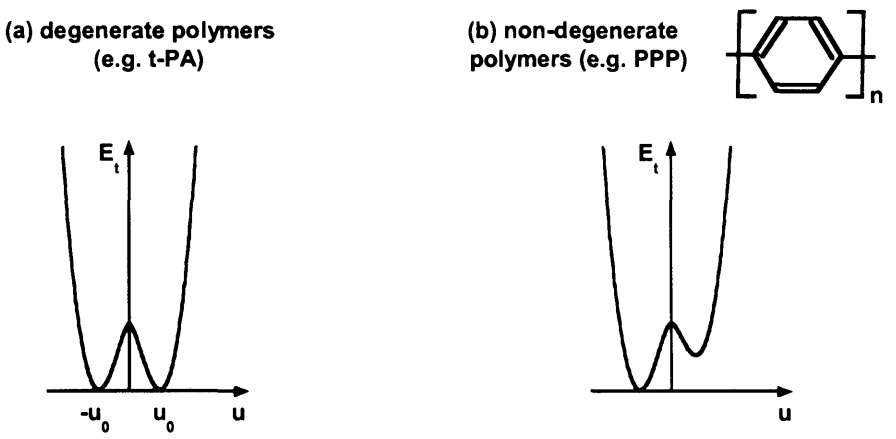

Figure 1.7: Total energy (E_t) as a function of the displacement parameter u, in (a) degenerate polymers, and (b) non-degenerate polymers. Chemical structure of polyparaphenylene (PPP) is also shown.

1.8. The six π orbitals, whose axis are perpendicular to the hexagonal plane, overlap and form six new orbitals that extend through the whole benzene ring[18,19]. Their energy levels, together with the schematics of the molecular orbitals are shown in Figure 1.8. The three energetically lowest orbitals are fully occupied (as indicated by the arrows), whereas the upper three orbitals are completely empty. Note that the orbitals marked with the letter N have nodes at para (1,4) positions.

When many benzene rings are linked in a chain, as in PPP, due to weak interaction between orbitals on neighbouring atoms, bands of energy levels are produced, centred at the level of the original benzene orbital, as illustrated in Figure 1.9. Note that the orbitals with nodes at para positions do not interact, so that their energy levels are unchanged. As a result of band broadening, which is further increased by disorder and electron-phonon coupling, the energy gap between the lowest unoccupied molecular orbital (LUMO) and the highest occupied molecular orbital (HOMO) is smaller in the polymer than in the individual benzene ring. For example, PPP optical energy gap is reportedly close to 3 eV[27,28], whereas the energy gap in benzene is approximately 6 eV[20].

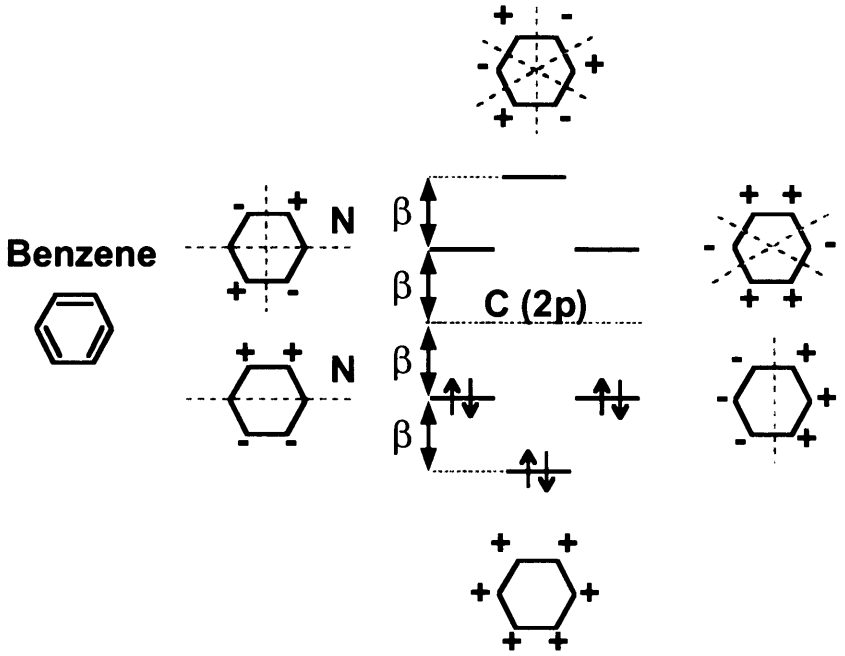

Figure 1.8: A sketch of benzene energy levels and the associated molecular orbitals. The broken lines indicate nodal planes, and + or - indicates the sign of the electron wavefunction. Orbitals marked with the letter N have nodes at para (1,4) positions. (Adapted from reference[19])

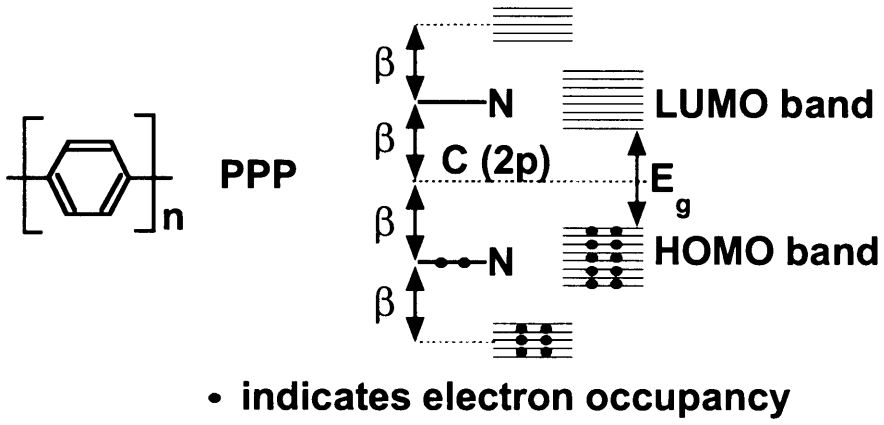

Figure 1.9: Schematic PPP energy level diagram. See text for discussion.

1.2.5 Charge Carriers in Trans-Polyacetylene[22,24,29,30]

In conjugated polymers, an electronic charge injected into the chain interacts strongly with the local lattice, inducing displacement and polarisation of the neighbouring atoms. When the electronic charge moves along the chain the atomic displacement and polarisation move together with it. The combination of the electronic charge with the atomic displacement and polarisation is called a polaron[29].

A related type of a charge carrier is a soliton, which can be either charged or uncharged. Soliton is a feature of degenerate polymers, and, in t-PA, it can be described as a 180° shift in dimerisation, in which the displacement parameter changes from u_0 to $-u_0$ (or the other way around). In Figure 1.10(a), going from left to right, the soliton (S^0) is represented by an abrupt shift from phase 1 to phase 2, and the antisoliton (S^0_A) is represented by the shift from phase 2 to phase 1. (Note that although this soliton representation is commonly used[24,29-31], in reality the solitons have a width of approximately seven CH groups[22,23,26].) The boundary between the two phases can be considered as a local suppression of Peierls transition, where the local carbon atom has zero displacement, i.e. $u = 0$. This leaves a localised C(2p) electron, not included in either the HOMO or the LUMO band, so that both bands are depleted by one-half of an energy state[22,24,26]. The energy level of this state is at the midpoint of the energy gap, as shown in Figure 1.10(a).

In an isolated t-PA chain, two solitons (S^0 and S^0_A) that are far apart but on the same chain would not interact, but in a solid, due to interaction between the chains, there is an attractive force between them[24]. If the two solitons approach each other, they interact and form two new energy levels, pushed symmetrically towards the edges of the antibonding and the bonding band, as illustrated in Figure 1.10(b). When the two solitons are neutral, they annihilate each other. However, if one of them is charged they cannot annihilate, but instead they form a polaron[24]. A negative soliton interacting with a neutral antisoliton produces a negative polaron, whereas a positive soliton interacting with a neutral antisoliton produces a positive polaron. If both solitons have the same charge bipolarons are created, as shown in

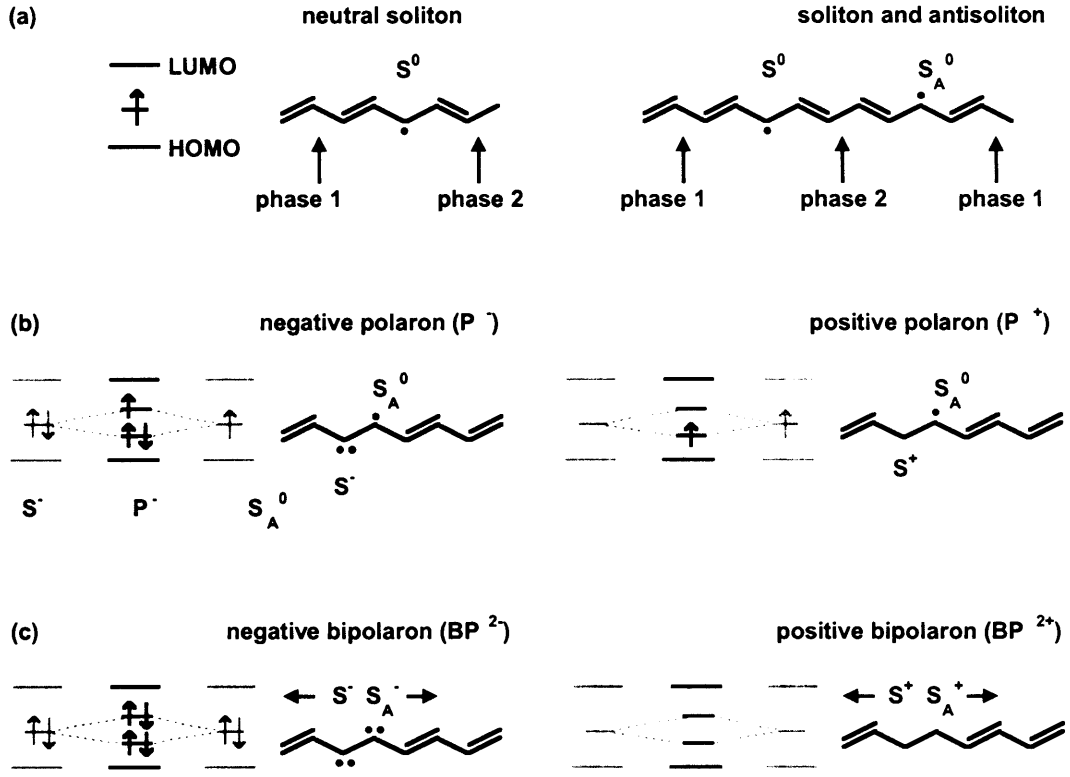

Figure 1.10: Schematic illustration of solitons and polarons in t-PA, and the associated band diagrams[24]: (a) neutral soliton and antisoliton, (b) negative and positive polarons, and (c) negative and positive bipolarons. See text for discussion.

Figure 1.10(c). However, in t-PA, the bipolaron is not stable and the two solitons tend to separate due to electrostatic repulsion, as indicated by the horizontal arrows in Figure 1.10(c).

1.2.6 Charge Carriers in PPP

In non-degenerate polymers such as PPP, polarons and bipolarons are the intrinsic charge carriers. An excitation such as a single soliton, which separates two phases with different energies, is not stable since the lower energy phase is preferred over the higher energy phase[22,31]. In Figure 1.11, where a topological representation of solitons, polarons and bipolarons in PPP is shown, phase 1 is the lower and phase 2 is the higher energy phase. Thus, phase 2 is not stable and the two neutral solitons S^0 and S^0_A (shown on the top panel) attract and annihilate one another. On

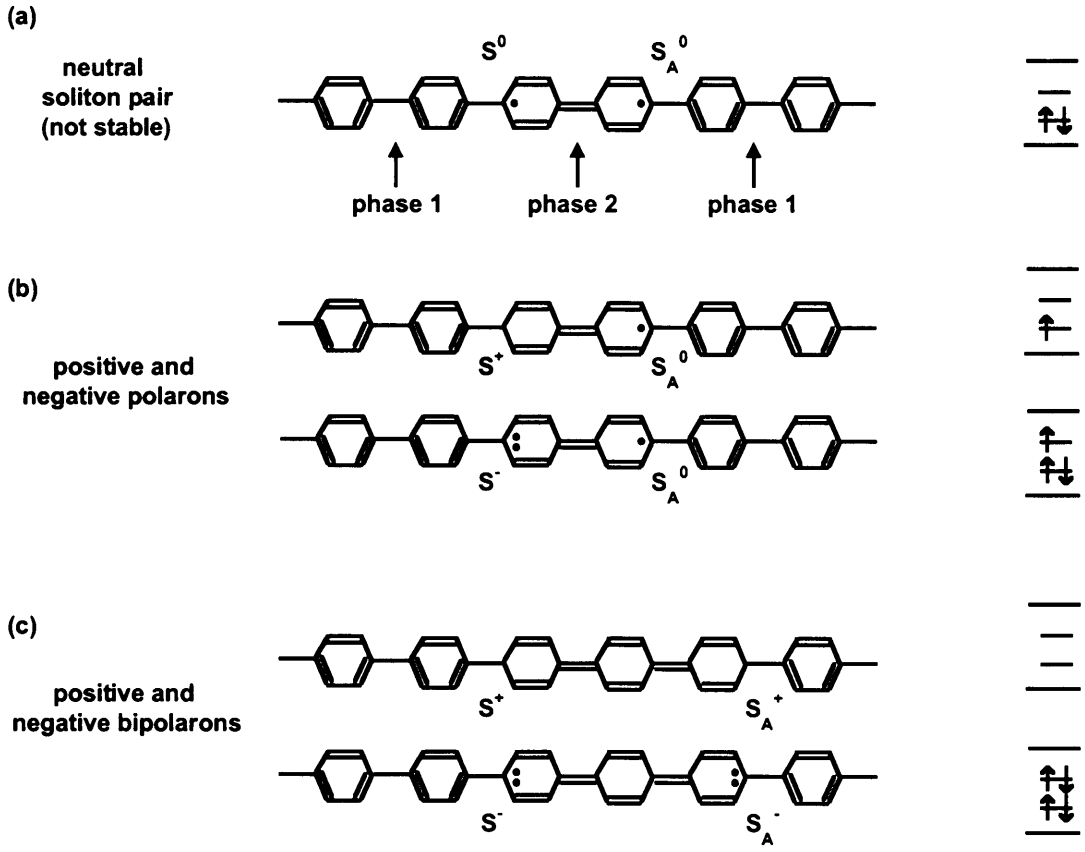

Figure 1.11: Topological representation of solitons, polarons and bipolarons in PPP, together with schematics of the associated band diagrams.

the other hand, a single polaron, shown schematically in Figure 1.11(b), is stable since it carries a unit of electronic charge which can not be annihilated. When the concentration of polarons is high, two equally charged polarons can lower their total energy by getting closer together to form a bipolaron[22], shown schematically in Figure 1.11(c). Although this increases the electrostatic energy, the width of the high energy phase decreases, so that the overall energy decreases[22]. Bipolarons are thought to play a major role in charge formation and transport in light-emitting polymers, especially at high charge concentration. Incidentally, we note that the lowest triplet excited state can be created from a bipolaron, for example by removing one electron (with the same spin) from each gap state of a negative bipolaron[22].

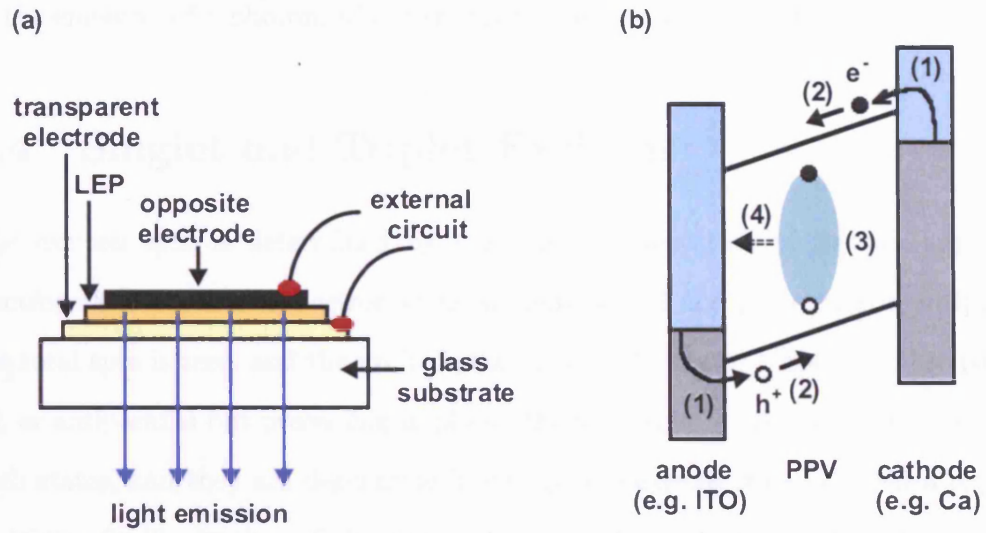

Figure 1.12: (a) Structure of a single-layer PLED. (b) Schematic diagram illustrating the main processes during operation of a typical PLED: (1) charge injection, (2) charge transport, (3) exciton formation, and (4) radiative decay of the exciton.

1.3 Basic Operation of Polymer Light-Emitting Diodes

The structure of a simple PLED, similar to the one reported by Burroughes *et al.*[9] in 1990, is shown in Figure 1.12(a). It consists of a single polymer layer sandwiched between two electrodes, one of which is transparent to allow the emission of light. Typically, indium tin oxide (ITO) is used as the transparent electrode, and metals such as Al or Ca are used as the other electrode. When a sufficiently large bias is applied across the electrodes, electrons are injected from one of the electrodes (the cathode), and holes are injected from the opposite electrode (the anode), as illustrated in Figure 1.12(b). Note that injection occurs into the polymer polaron levels, rather than conduction or valence bands[32]. As the polaronic carriers move towards the opposite electrode, under the influence of the electric field (or diffusion if the field is screened[33]), they may meet with oppositely charged carriers and form electron-hole pairs (excitons)[34], bound by electrostatic attraction. Unlike in crystalline semiconductors where exciton binding energy is relatively small (e.g. 4 meV in GaAs[35]), exciton binding energy in conjugated polymers is considerably larger (hundreds of meVs). Radiative recombination of the electron-hole pair results

in the emission of a photon, whose energy is specified by the exciton energy gap.

1.4 Singlet and Triplet Excitons

The exciton spin is determined by the relative orientation of its two unpaired electrons[36]. If the two electron spins are antiparallel and precessing in antiphase the total spin is zero, and the excited state is a singlet state. If the spins are parallel, or antiparallel but precessing in phase, the total spin is one. As there are three such states, and they are degenerate in energy, the excited state is called a triplet. A schematic illustration of the energy levels of the first excited singlet (S_1) and triplet (T_1) states, relative to the ground state (S_0) is shown in Figure 1.13. Under electrical operation, both singlets and triplets are generated, and their transition to the ground state can in principle occur both by radiative or non-radiative decay. However, owing to the spin selection rules, the T_1 - S_0 transition is forbidden and must be achieved via an additional spin-flipping process, induced for example via interaction with impurities or defects. Consequently, triplets have relatively long decay times, which means that they are more likely to diffuse to quenching sites[37]. Even if the triplet lifetime is reduced to several microseconds, for example by introducing heavy atoms with large spin-orbit coupling (such as Pt) into the chain, the non-radiative decay rate ($\sim 10^5$ - 10^6 s^{-1}) is still orders of magnitude larger than the radiative decay rate ($\sim 10^3$ s^{-1}), which means that only one in 1000 of the triplets emit light[36,37]. Therefore, emission in most polymers occurs via radiative decay of the singlet exciton.

Note that, due to spin-flipping, S_1 excitons can transform into T_1 excitons in a process called intersystem crossing. Since the energy separation between S_1 and T_1 states in conjugated polymers is close to 0.7 eV[38], intersystem crossing proceeds in only one direction, i.e. from S_1 to T_1.

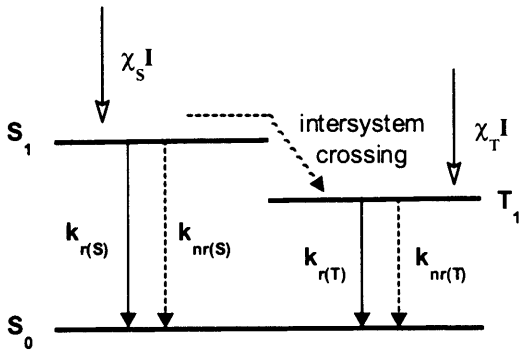

Figure 1.13: Schematic diagram showing the formation and decay of singlet and triplet excited states in conjugated polymers under electrical excitation. S_0 is the singlet ground state, S_1 is the lowest excited singlet state, and T_1 is the lowest triplet state. k_r and k_{nr} denote the radiative and non-radiative decay rates respectively. χ_S and χ_T represent the fractions of singlet and triplet excitons generated, respectively. (Adapted from reference[37])

1.5 The PLED Efficiency

Energy efficiency is an important issue in PLEDs, not only because of energy consumption issues, but also because the wasted energy may lead to PLED degradation. The efficiency is often expressed by equations 1.2 and 1.3, which respectively give the internal and external quantum efficiency[2].

$$\eta_{internal} = \gamma \cdot q \cdot r_{st} \tag{1.2}$$

$$\eta_{external} = \gamma \cdot q \cdot r_{st} \cdot \eta_{coupling} \tag{1.3}$$

γ is the ratio of the number of excitons formed over the number of electrons flowing in the external circuit. It is related to the balance between electron and hole currents, and is high when electron and hole currents are balanced, and small for excessive majority carrier currents. Photoluminescence efficiency q is related to the intrinsic efficiency of the polymer chain, which in the solid may be additionally influenced by interactions with neighbouring chains and impurities, and also by other effects, such as exciton coupling to plasmon modes on the metallic electrode. The factor r_{st} is the fraction of excitons formed as singlets, and accounts for the non-emissive nature

of triplet states. The output coupling coefficient ($\eta_{coupling}$) is related to the fraction of emitted photons that escape from the device into air. Due to the refractive index mismatch, a considerable portion of the emitted photons are trapped within the PLED, where they are either dissipated or scattered as edge emission.

In the first reported PLEDs the efficiency was close to 0.01 %[9], but since then it has improved considerably, and recently reported external efficiencies are as high as 22 %[39]. The factors γ and q are now often close to unity[2]. High γ values can be achieved by lowering charge injection barriers to achieve balanced carrier injection[40]. The factor q is increased by reducing the amount of impurities in the active layer, and also by increasing the intrinsic chain efficiency, or by positioning the recombination zone away from the metal contact to reduce plasmon-induced quenching[40]. Improving the other two factors, r_{st} and $\eta_{coupling}$, has proven to be more difficult, and these are still significantly below the optimum value. In recent years however, significant efforts have been put towards their improvement, as we next discuss.

From simple spin statistics it might be expected that r_{st} is fixed at 0.25, since the ratio of singlet to triplet states is 1:3. However, some reports suggest that the singlet generation fraction can exceed the 25 % statistical limit in some polymers, and can reportedly be as high as 50 %[37,41-43]. Several explanations for this have been proposed, as discussed in a recent review[36]. A recent proposal for instance suggests that the formation rates for singlets and triplets vary with chain length, favouring singlets in longer chains[42]. However, consensus has not been reached, and recently it was even argued that the 25 % singlet generation limit may not have been exceeded[44]. The emission efficiency can also be increased by doping the host polymer with a small concentration ($\sim$ 3 %) of a phosphorescent dye. This method was originally applied to small molecule light emitting diodes[45], and later to polymer-based devices[46-48]. As shown in Figure 1.14, in this method, the vast majority of host singlets and triplets are efficiently transferred to the guest molecules, excluding a minor fraction of singlets that manage to decay to the host ground state[40]. Since the phosphor emission efficiency is very high, the majority of

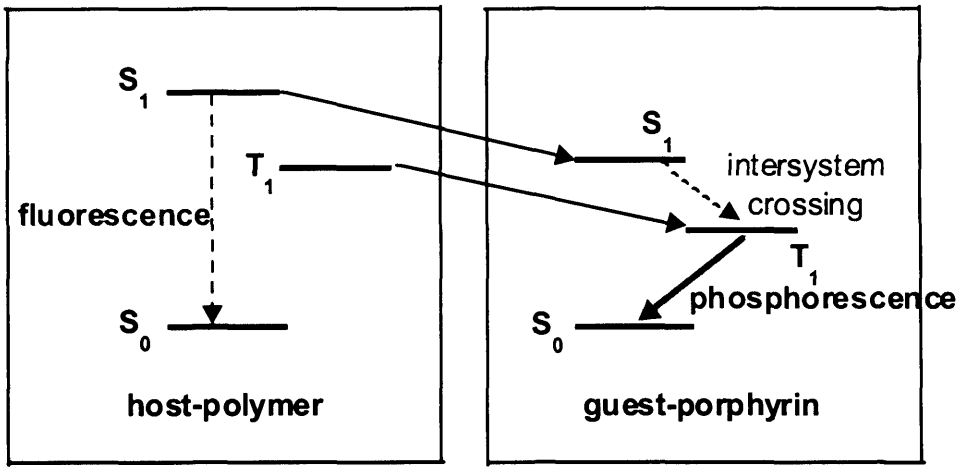

Figure 1.14: Schematic diagram showing exciton transfer in host-guest systems. Adapted from Patel *et al.*[40]

transferred excitons decay radiatively to the phosphor ground state. Thus, the host triplet energy that would otherwise be wasted is harvested and used to emit light. Remarkably, internal emission efficiencies close to 100 % (at low brightness) were reported with this method[49]. Note however that although this method is suitable for red- and green-emitting devices, it is not well suited for blue emission, due to the need for a high band-gap host semiconductor[7]. Another drawback is that the dopant sites become saturated at operational current densities due to long triplet lifetimes, which increases exciton quenching and lowers the efficiency[48].

The factor $\eta_{coupling}$ arises because the photons emitted by the active layer need to pass through at least two different materials before escaping into air, as shown in Figure 1.15(a). Due to Snell's law for refraction, light incident at an angle less than a critical angle will undergo total internal reflection at the anode-glass and the glass-air interface. As shown, this leads to two waveguided modes, one in the substrate/ITO/organic layers and the other in the organic/ITO layers[40]. Only a fraction of light, typically close to 20 - 30 %, escapes into air, which thus severely limits the external quantum efficiency. Several methods for improving the output coupling have been demonstrated however. In one example, Tsutsui *et al.*[50] increased the external emission by a factor of 1.8, by inserting a low refractive index silica aerogel layer between ITO and glass. The aerogel layer reduces waveguiding and edge emission caused by internal reflections, and increases the output cou-

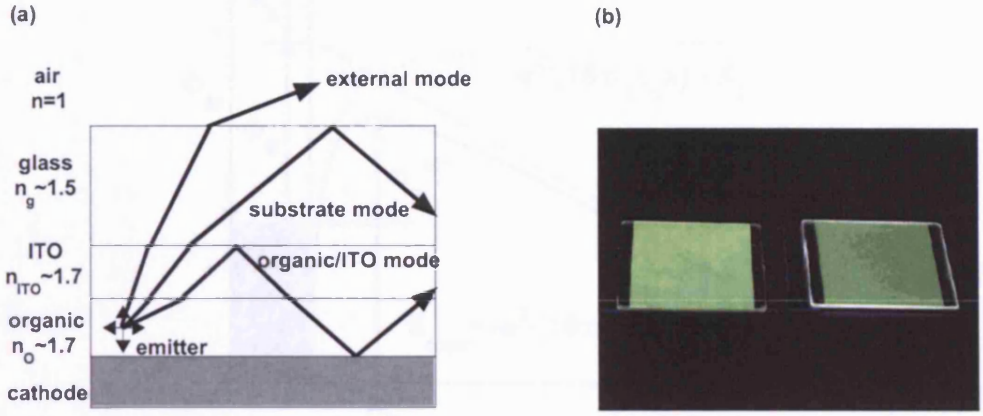

Figure 1.15: (a) Most of the light emitted in an organic layer is waveguided in the substrate, or organic/ITO layers, whilst only a smaller fraction is emitted externally. (Adapted from Patel *et al.*[40]) (b) An example demonstrating increased optical output when a thin aerogel layer is placed betweeen the emissive layer and the glass substrate. The photograph compares thin emissive organic layers on glass substrates with (left) and without (right) an aerogel spacer layer under UV radiation. Reproduced from Tsutsui *et al.*[50]

pling, as demonstrated in Figure 1.15(b). The efficiency can also be enhanced if the substrate waveguided mode is scattered by: increasing the substrate surface roughness[51], or attaching a monolayer of silica microspheres[52], or a diffusive layer[53], at the substrate-air interface.

1.6 Charge Carrier Injection and Transport

The conduction in the organic layer starts by charge injection from delocalised states of the metal contact, into a distribution of the polymer's localised states. Typically, there is an energy barrier (Φ_B) that the carriers need to surmount to enter the polymer layer. A schematic energy level diagram of a metal-semiconductor interface, in the presence of an electric field F, is shown in Figure 1.16. Owing to the combined effects of the field and the image force, the energy barrier Φ_B is reduced to Φ_B^{eff}[54].

To describe the injection into organic semiconductors, two textbook models borrowed from inorganic semiconductor physics have on occasions been employed[55,56].

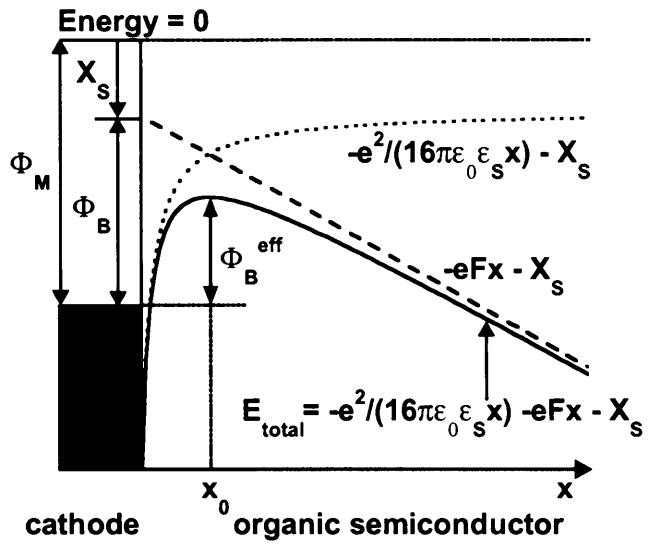

Figure 1.16: Schematic energy band diagram of the metal-semiconductor contact. Φ_M is the metal work function, Φ_B is the injection barrier height at zero electric field, and X_S is the electron affinity of the semiconductor. The cathode supplies electrons which are injected into a distribution of the organic polaron levels[32]. The solid line represents a minimum of this distribution, modified by the image force energy $-e^2/(16\pi\varepsilon_0\varepsilon_s x)$, and the field energy -eFx. As a result of the image and field forces, the effective barrier is reduced to Φ_B^{eff}.

These are Fowler-Nordheim (FN) quantum mechanical tunnelling and thermionic emission. The former invokes quantum mechanical tunnelling of electrons through an energy barrier. It ignores image charge effects, and for the simple case of a triangular barrier, shown by dashed line in Figure 1.16, it predicts[54]

$$J \propto F^2 \cdot \exp(-\frac{\kappa \cdot \phi_B^{3/2}}{F}), \tag{1.4}$$

where J is the current, and κ is a constant in terms of the effective carrier mass. Tunnelling becomes significant only at high fields (larger than 10^8V/m)[54,57].

Contrarily, thermionic emission is a classical process which, being thermally activated, depends on the temperature T. For charge injection from a metal into a *crystalline* semiconductor, it predicts the following current dependence[54,55,58]:

$$J = A^* \cdot T^2 \cdot \exp(\frac{-\phi_B^{eff}}{k_B T}), \tag{1.5}$$

where k_B is the Boltzmann constant, and A^* is known as the Richardson constant. The current also has a field dependence included in the factor ϕ_B^{eff}, due to barrier

lowering by field and image effects.

However, unlike in crystalline semiconductors, where charges propagate freely in extended states, conduction in polymer films proceeds by hopping between localised, energetically disordered polaronic states[32], and neither of the two models takes this into account. Consequently, their predicted current characteristics often lack in accuracy when applied to polymer diodes[58,59]. In one of the widely cited publications, Parker has used the FN model to explain the measured current-voltage characteristics of MEH-PPV-based single carrier devices[60]. He reported good qualitative agreement between the model and the functional dependence of the current on field and temperature. However, the measured current was three orders of magnitude smaller than expected from the FN model, and neither image force nor band bending effects could explain such behaviour[61]. However, Davids *et al.*[61] reported that if the low carrier mobility of the organic material is taken into account large current backflow from the polymer back into the injecting contact is predicted, which accounts for the small current.

Other investigations on the other hand have reported that any similarity between the measured current and the FN model must be accidental entirely[62-64]. Namely, a model that does not invoke any long-range tunnelling transitions can fully account for the experimental current-voltage characteristics of injection currents, such as those reported by Parker[62,63,65]. The main feature of this model is that the charges are first injected into acceptor states in the interfacial layer, below the manifold of hopping states, in a process described as thermally and field assisted charge transfer[62]. From there, they can either return back to the metal contact, or overcome the image potential by thermally activated hopping[57], and access the bulk states away from the interface. At low fields only few carriers escape the image potential, and most end up back in the metal contact, resulting in a large current backflow[55]. This could explain the relatively weak temperature dependence of injection currents observed in some PLEDs, despite the presence of large injection barriers[66].

Due to the applied electric field, the charges that escape the image potential can

move towards the other electrode. They can either travel along individual polymer chains (intra-chain transport) or, eventually, they need to transfer between different chains (inter-chain transport), by hopping from one chain to the next. Intra-chain mobility along the conjugated segments is high and comparable to inorganic semiconductors mobilities (1 to 10^3 $cm^2V^{-1}s^{-1}$)[57]. For instance, the reported intra-chain mobility in isolated PPV-based chains is close to 0.2 $cm^2V^{-1}s^{-1}$[67]. The mobility of bulk polymer films on the other hand is much smaller, close to 0.5×10^{-6} $cm^2V^{-1}s^{-1}$ for a similar polymer[68]. This occurs because inter-chain mobility is much lower, due to low electronic state coupling between neighbouring chains[69]. Also, due to the variation in conjugation lengths between different chains, and between different segments on the same chain, there is a spread in polaronic energy levels, further exacerbated by defects and various chemical and topological disorders. This generates potential barriers or traps, which impede charge transport and thus reduce the bulk mobility.

Charge carriers can overcome an energy barrier using the thermal energy of the solid, or, alternatively, by tunnelling. In both cases, the probability of overcoming the barrier is increased if an electric field is applied, due to the lowering of the effective energy barrier. Thus, the mobility $\mu(F)$ is field-dependent, and increases with increasing fields. For many polymer systems it is given by[20,40]

$$\mu(F) = \mu_0 \exp(\rho\sqrt{F}), \tag{1.6}$$

where μ_0 and ρ are material and temperature dependent parameters.

In single-carrier diodes (i.e. in diodes in which the current is dominated by either electrons or holes), two limiting regimes for the current are known to exist[40,55,70]. For large injection barriers or large mobilities the current is limited by the rate of carrier injection into the organic material. This is the *injection limited current (ILC)*, which depends sensitively on the height of the injection barrier. Davids *et al.* have shown that for typical single-carrier PLEDs the current is injection limited for barriers higher than about 0.3 - 0.4 eV[56,70]. At lower injection barriers the current is likely to be *space charge limited (SCL)*. In this regime, the charges are injected

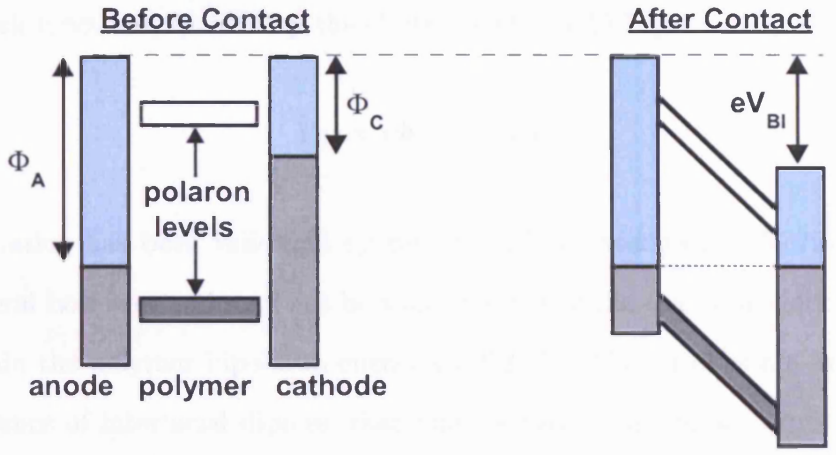

Figure 1.17: Schematic energy level diagram of a simple PLED before and after contact is made between the polymer and the electrodes. Φ_A and Φ_C are the anode and cathode work functions respectively.

faster than they can pass through the polymer layer, leading to charge accumulation. SCL current (J_{SCL}) in most single carrier organic devices is given by[40,54,57,71]

$$J_{SCL} = \frac{9}{8} A \varepsilon_0 \varepsilon_r \mu(F) F^2 / d, \tag{1.7}$$

where A is the cross sectional area, ε_0 is the permittivity of free space, ε_r is the relative dielectric constant, and d is the organic layer thickness.

1.7 The Built-In Voltage

Figure 1.17 shows a schematic energy level diagram of a single-layer PLED, before and after contact is made between the polymer and the two electrodes. Typically, asymmetric electrode work functions are employed in order to enhance electron and hole injection. The cathode has the lower and the anode has the higher work function. After contact, the chemical potential is equilibrated through the heterostructure, via electron transfer from the cathode to the anode. The resulting charge distribution generates a built-in voltage (V_{BI}) between the electrodes, supporting a built-in electric field in the polymer layer. In many PLEDs, V_{BI} is (to a good approximation) given by the difference between the anode (Φ_A) and the cathode

(Φ_C) work functions, divided by the electronic charge[55,72]:

$$V_{BI} = (\Phi_A - \Phi_C)/e. \tag{1.8}$$

This equation has been validated by several PLED investigations[55,72-76]. It is not general however, and may not be valid if either of the electrode work functions lies within the polymer bipolaron energy gap[72,77]. Also, it does not account for the presence of interfacial dipoles, that may be present in certain types of metal-semiconductor interfaces[55].

We remark that the rigid polaron band picture shown on the right-hand side in Figure 1.17 is only applicable in the absence of space charge in the active layer, which otherwise would cause a spatially non-uniform electric field. We note that typically, but not always, PLEDs are produced with low amounts of impurities and traps in the active layer, so that in reverse and weak forward bias the rigid band picture is appropriate[55,77,78].

We also note that the concentration of surface states in conjugated polymers is typically small compared to inorganic semiconductors (e.g. silicon). Surface states in the latter result from orbitals which cannot bond due to the lack of atoms at the semiconductor surface. The ordered covalent bonding system which prevails in the bulk and gives rise to the bandgap is disrupted at the surface, typically resulting in a significant concentration of dangling bonds, and associated gap states at the surface. In general, depending on their energy, these states can affect charge injection barriers, particularly if they are located deep within the energy gap. Consider as an example a cathode-semiconductor interface with a non-zero electron injection barrier. If the gap states here are located below the cathode Fermi level, an electron transfer from the metal to the semiconductor will occur, which will tend to 'pin' the metal Fermi level to the energy defined by the surface states. This means that the electron injection barrier would be governed by the energy difference between the semiconductor conduction band and the gap state energy, rather than the Fermi energy of the cathode. In contrast to inorganic semiconductors, conjugated polymers have a low concentration of unsaturated bonds since π electrons which give rise to

the bandgap are localised mostly within a single chain, and they are therefore not significantly affected by the presence of a film surface[55]. Thus, importantly, the phenomenon of Fermi level pinning by the surface states does not typically occur in conjugated polymers.

1.8 Outline of Work

In this thesis we present electroabsorption (EA) investigations of blue-emitting polyfluorene-based PLEDs. The main focus of the research is to use EA spectroscopy in order to gain new information about blue-emitting PLEDs, with the ultimate aim of helping to improve their lifetime characteristics. In Chapter 2, we introduce electroabsorption from the perspective of the Stark effect, and then give an overview of the literature concerning EA characterisations of PLEDs. Chapter 3 focuses on the specific EA techniques used during the course of the research, and includes a description of the EA experimental set-up. Also, a simple PLED is measured to test the experimental apparatus, and to serve as a point of reference from which other (more complicated devices) can be considered. Chapter 4 reports on EA measurements of the devices with the structure ITO/PEDOT:PSS/emitting-polymer/LiF/Ca/Al, most commonly used in the course of this research. In Chapter 5, we specifically focus on EA measurements of the built-in voltage, and use the results to gain an insight into the energy level alignment across these PLED heterostructures. In Chapter 6, we employ EA spectroscopy in the study of degradation effects in blue-emitting PLEDs. Finally, Chapter 7 concludes the thesis by summarising the main findings.

Chapter 2

Characterisation of Polymer Light-Emitting Diodes by Electroabsorption Spectroscopy

In the presence of an electric field (F) molecular energy levels are shifted due to the Stark effect, resulting in an altered photon absorption spectrum, which can be probed experimentally using modulation spectroscopy techniques, for example via electroabsorption (EA). EA is particularly suited for characterisation of polymer-based light-emitting diodes (PLEDs), as it allows non-destructive probing of the polymer layer 'buried' between the two electrodes. Typically, in EA investigations of PLEDs, a sum of ac and dc voltages is applied across the device so that the intensity of an optical probing beam passing through the active layer is modulated. Interestingly, due to the field dependence of the Stark effect, this allows the measurement of the PLED built-in voltage (i.e. the voltage generated upon equilibration of the Fermi levels through the PLED heterostructure). The predicted change in absorption ($\Delta\alpha$) induced by the applied field is proportional to the square of the electric field[72,79]. Here we present the relevant derivation, and also obtain the predicted EA dependence on applied ac and dc voltages. We then discuss examples from literature involving PLED characterisation by EA spectroscopy.

2.1 Introduction to EA Spectroscopy

Electroabsorption (EA) spectroscopy belongs to a group of modulation spectroscopy techniques that involve modulation of optical properties of a sample, typically through a periodic change of an external parameter such as the electric field (electromodulation), temperature (thermomodulation), or stress (piezomodulation)[80]. The early success of modulation spectroscopy (and electromodulation spectroscopy in particular) in studying the electronic structure of inorganic crystals[79,80], has encouraged its application to organic solids[81-84]. For example, Sebastien and Weiser reported electromodulation studies of polydiacetylene single crystals in 1979[81], and vapour deposited layers of tetracene and pentacene in 1981[82]. In 1989 Phillips *et al.* reported studies of nonoriented cis- and trans-polyacetylene films[83], and in 1992 Horvath *et al.* reported electroabsorption studies of a PPV-based polymer, and polydodecylthiophene (PDT)[85], using it to estimate the spatial extent of the exciton.

In a polymer light-emitting diode (PLED) structure, electric-field modulation of the polymer layer is achieved by the application of an external voltage across the device. An optical probe beam typically enters the active layer through the transparent electrode, where its intensity is modulated. In our experiments, the beam is then reflected off the opposite electrode, back into the active layer, exiting the device through the transparent electrode. Due to the thinness of the active layer ($\sim$ 100 nm), high electric fields necessary to produce measurable EA signals (on the order of 10^6 to 10^8 Vm^{-1}) are easily achieved with a relatively small applied voltage (typically within an order of magnitude of 1 V)[72,74,77,86,87]. When the voltage is applied, the electric field induces a change in the polymer absorption coefficient via the linear and quadratic Stark effects, which we discuss in the next section.

2.2 Linear and Quadratic Stark Effect in Conjugated Polymers

The effect of static electric fields on atoms and molecules is known as the Stark effect, after J. Stark, who in 1913 studied the effect of such fields on the spectrum of hydrogen and other atoms[88]. When placed in an electric field **F**, directed along the z axis, the Hamiltonian of an unperturbed molecular electronic state $\mid \Psi_i\rangle$ is modified by the addition of the following perturbation[88]:

$$H' = eFz, \tag{2.1}$$

where $-e$ is the electron charge. Owing to this perturbation, an energy level i is shifted by a value given by the expectation value of the operator:

$$\Delta E_i = eF\langle \Psi_i \mid z \mid \Psi_i\rangle. \tag{2.2}$$

In centrosymmetric conjugated polymers, electronic states cannot have a permanent electric dipole moment due to their symmetry. However, permanent dipoles can still occur as a result of disorder, such as geometrical distortions, aggregates and chain defects, which can break the symmetry. For instance, defects are known to disrupt the conjugation, and can act as energy barriers which limit the size of coherent states. In one report, an electronic state whose conjugation is limited by defects was simulated as a potential well with asymmetric barrier heights[89]. For a 4 nm conjugated segment and a barrier difference of 80 meV, there was an asymmetry in charge distribution, resulting in a net permanent dipole of 55 D. The linear Stark shift induced by such permanent dipoles can be expressed by equation 2.3, where **m** is the dipole moment[55,90].

$$\Delta E_i = -\mathbf{m} \cdot \mathbf{F} \tag{2.3}$$

To obtain the shift ΔE of an optical transition from state A to state B, we need to calculate the difference between Stark shifts of state B and state A, as in

equation 2.4

$$\Delta E = -(\mathbf{m}_B - \mathbf{m}_A) \cdot \mathbf{F} = -\Delta \mathbf{m}_{BA} \cdot \mathbf{F}, \tag{2.4}$$

where $\Delta \mathbf{m}_{BA}$ is the dipole difference between B and A states. Experimentally measured shifts found in literature range from $\sim$ 170 μeV[90] to $\sim$ 5000 μeV[89].

Figure 2.1(a) is a schematic illustration of the linear Stark shift in two orientational subpopulations, in which the dipole moment is oriented either with or against the field, resulting in a downward or an upward shift of the energy level respectively. For these subpopulations, provided that the excited state dipole is greater than that of the ground state, the optical transition is red-shifted, or blue-shifted, as indicated in Figure 2.1(b). The change in absorption (field on minus field off) follows the line shape of the second absorption derivative[91], which is shown in Figure 2.1(c).

In the absence of permanent dipoles, an electric field can still shift energy levels due to the quadratic Stark effect. The quadratic Stark effect is a second order perturbation and causes a much smaller shift than the linear Stark effect. For example, Harrison *et al.* reported linear and quadratic Stark shifts of 170 μeV and 33 μeV respectively, in the ladder-type PPP polymer, MeLPPP[90].

In the quadratic Stark effect, one considers a shift in the state $\mid i\rangle$ induced by virtual excitation to all states $\mid j\rangle$ coupled with non-zero dipole moment $\mu_{ij} = \langle i \mid e\mathbf{r} \mid j\rangle$[89-94]. The energy shift of the level i is given by[90,94]

$$\Delta E_i = \sum_{i \neq j} \frac{\mid \boldsymbol{\mu}_{ij} \cdot \mathbf{F} \mid^2}{(E_i - E_j)}, \tag{2.5}$$

where E_i - E_j is the energy difference between levels i and j.

To discuss the effect further, it is illustrative to consider a simple three-level system[92], as in Figure 2.2(a)[90,94], where $1A_g$ is the ground state, and mA_g is a one-photon forbidden state positioned above $1B_u$ (lowest allowed excited state) in a PPP-based polymer[90]. In this case, the shift of the $1B_u$ state is given by[90,92]

$$\Delta E(1B_u) = \frac{(\boldsymbol{\mu}_{BA} \cdot \mathbf{F})^2}{E(1B_u) - E(mA_g)}, \tag{2.6}$$

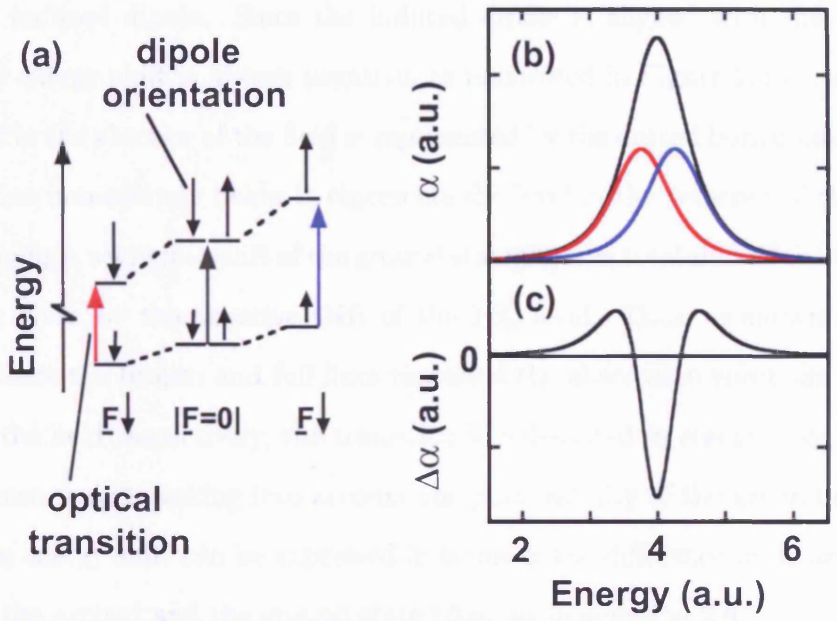

Figure 2.1: Schematic illustration of the linear Stark effect. (a) The effect of the applied electric field on energy levels of two orientational subpopulations in which the dipole moment is oriented either with or against the field, resulting in a downward or an upward energy shift respectively. Consequently, the optical transition from the ground state to the lowest excited singlet state is either red- or blue-shifted, as indicated by the coloured arrows. (b) Optical absorption spectrum with $\mathbf{F} = 0$, shown in black, and $\mathbf{F} \neq 0$, shown in red and blue (corresponding to the red- and blue-shifted transition respectively). (c) The difference between the spectrum with the field on and the field off follows the second derivative line shape, which is shown here. (Adapted from Bublitz and Boxer[91].)

where $\boldsymbol{\mu}_{BA}$ is the transition dipole moment between $1B_u$ and mA_g states. This can also be expressed in terms of the polarisability p of the $1B_u$ exciton (which in conjugated polymers is typically between $\sim$ 2000 to $\sim$ 8000 Å$^3 \times 4\pi\varepsilon_0$), as in equation 2.7[90-94].

$$\Delta E(1B_u) = -\frac{1}{2}pF^2 \tag{2.7}$$

In essence, the quadratic Stark shift arises due to interaction between the field and the field induced dipole. Since the induced dipole is aligned with the field, the produced energy shift is always negative, as illustrated in Figure 2.2(a), where the $1B_u$ level in the absence of the field is represented by the dotted horizontal line, and the full line immediately below it represents the level in the presence of the field.

Assuming a negligible shift of the ground state[90], the total shift of the transition energy is given by the negative shift of the $1B_u$ level. Thus, as shown in Figure 2.2(b), where the broken and full lines represent the absorption spectrum with and without the field respectively, the transition is red-shifted in energy. For the more general case though, taking into account the polarisability of the ground state, the transition energy shift can be expressed in terms of the difference in polarisabilities between the excited and the ground state (Δp), as in equation 2.8.

$$\Delta E = -\frac{1}{2}\Delta pF^2 \tag{2.8}$$

Interestingly, in the quadratic Stark effect, the change in absorption (field on minus field off) follows the line shape of the first derivative[91], which is shown in Figure 2.2(c).

Ultimately, ΔE is determined by both the linear and the quadratic Stark shift, so that

$$\Delta E = -\Delta\mathbf{m}_{BA} \cdot \mathbf{F} - \frac{1}{2}\Delta pF^2. \tag{2.9}$$

Now, the change in absorption, $\Delta\alpha = \alpha(F) - \alpha(0)$, can be expressed in powers of ΔE using a Taylor expansion of $\alpha(E + \Delta E)$ up to the second order of ΔE[55,89,90,94]:

$$\Delta\alpha = \left\langle \frac{\partial\alpha}{\partial E}\Delta E \right\rangle + \frac{1}{2}\left\langle \frac{\partial^2\alpha}{\partial E^2}\Delta E^2 \right\rangle + ... \tag{2.10}$$

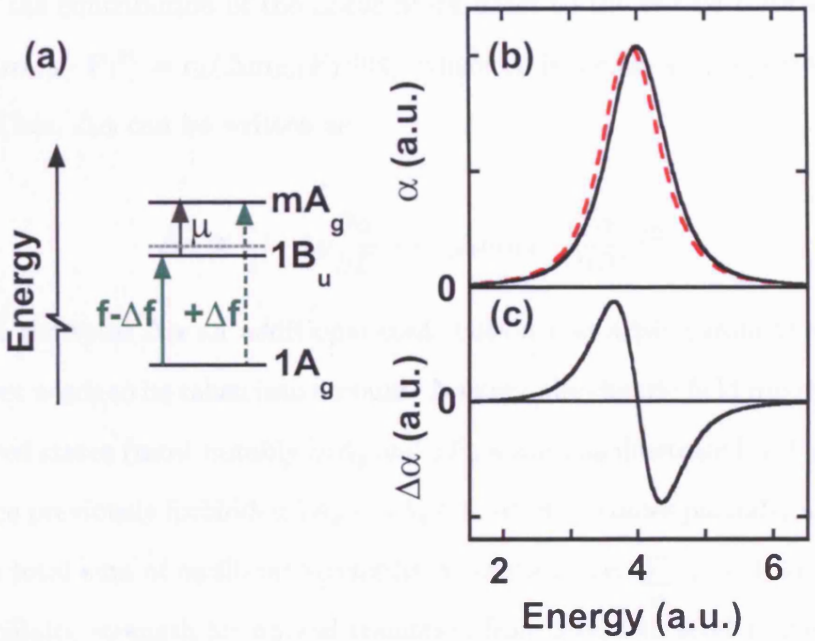

Figure 2.2: Schematic illustration of the quadratic Stark effect in conjugated polymers. (a) In the presence of the field, the $1B_u$ and mA_g states become mixed owing to a non-zero dipole moment (μ) between the two levels. Consequently, the $1B_u$ state becomes polarised[92], and, due to the field interaction with the induced dipole, the $1B_u$ state is lowered from the dotted horizontal line to the full horizontal line immediately below it[91]. Another consequence of state mixing is that the forbidden $1A_g$ - mA_g transition indicated by the broken vertical arrow becomes partially allowed, resulting in a decrease (Δf) of the oscillator strength (f) of the allowed transition. (b) Due to the lowering of the $1B_u$ level, the absorption spectrum with the field off (full black line) becomes red-shifted when the field is on (broken red line). (c) The change in the absorption (field on minus field off) follows the first derivative of the absorption[91], which is shown here.

For an isotropic distribution of polymer chains the expectation value $\langle \Delta \mathbf{m}_{BA} \cdot \mathbf{F} \rangle$ is zero, and therefore the first term in equation 2.10 only contains contributions from the quadratic Stark effect[55,90], i.e.

$$\langle \Delta E \rangle = -\frac{1}{2} \Delta p F^2. \tag{2.11}$$

However, the contribution of the linear Stark effect to the second term is non-zero since $\langle (\Delta \mathbf{m}_{BA} \cdot \mathbf{F})^2 \rangle = c_L (\Delta \mathrm{m}_{BA} F)^2$[94], where c_L is a constant, reported to equal 1/3[55]. Thus, $\Delta\alpha$ can be written as

$$\Delta\alpha \cong \frac{1}{2}[-\Delta p \frac{\partial \alpha}{\partial E} + c_L (\Delta m_{BA})^2 \frac{\partial^2 \alpha}{\partial E^2}] F^2. \tag{2.12}$$

To obtain the total $\Delta\alpha$ an additional contribution also arising from the quadratic Stark effect needs to be taken into account. Namely, the electric field mixes forbidden and allowed states (most notably mA_g and $1B_u$ states, as illustrated in Figure 2.2a), so that the previously forbidden $1A_g$ - mA_g transition becomes partially allowed[90]. Since the total sum of oscillator strengths is constant, i.e. $\sum_{j \neq i} f_{ij} = 1$[35], where f_{ij} is the oscillator strength for optical transition from level i to level j, there is a net transfer of oscillator strength from the $1B_u$ allowed to the one-photon forbidden transition of the mA_g exciton. Thus, the transfer of oscillator strength contributes negatively to $\Delta\alpha$ near the $1\mathrm{A}_g$ - $1\mathrm{B}_u$ transition energy, and positively near the $1A_g$ - mA_g transition energy. The fractional change of oscillator strength is given by[55,85,90,93]

$$\frac{\Delta f_{ij}}{f_{ij}} = \frac{| \boldsymbol{\mu}_{ij} \cdot \mathbf{F} |^2}{(E_i - E_j)^2}. \tag{2.13}$$

Combining equations 2.12 and 2.13, $\Delta\alpha$ can be rewritten as[55]

$$\Delta\alpha = [c_T \frac{| \mu_{ij} |}{(E_i - E_j)^2} \alpha - \frac{1}{2} \Delta p \frac{\partial \alpha}{\partial E} + c_L (\Delta m_{BA})^2 \frac{\partial^2 \alpha}{\partial E^2}] F^2 \ , \tag{2.14}$$

where c_T is a constant. This can be conveniently expressed as

$$\Delta\alpha = G(h\nu)F^2, \tag{2.15}$$

where $h\nu$ is the photonic energy, and

$$G(h\nu) = [c_T \frac{\mid \mu_{ij} \mid}{(E_i - E_j)^2}\alpha(h\nu) - \frac{1}{2}\Delta p\frac{\partial\alpha(h\nu)}{\partial E} + c_L(\Delta m_{BA})^2\frac{\partial^2\alpha(h\nu)}{\partial E^2}]. \tag{2.16}$$

We note that G($h\nu$) is proportional to the imaginary part of the third order dielectric susceptibility[72,79].

In typical conjugated polymers, the first term in equation 2.16 is usually small compared to the other two terms due to the relatively large energy separation between mA_g and $1B_u$ states[89]. For instance, in polydiacetylene[89] and MeLPPP[90], mA_g was reported to lie 0.5 and 0.7 eV respectively above the $1B_u$ state. Incidentally, we note that in systems with small energy separation, for example in charge-transfer excitons of crystalline anthracene-PMDA (pyromellitic dianhydride), the first term can dominate the line shape[89].

The relative importance of the two other two terms in equation 2.16 depends on the polymer structure, as well as on the film quality, due to the factors such as chain order, chemical purity and the presence of defects, which can influence the formation of both permanent and field induced dipoles. In an investigation by Harrison *et al.*[90], involving MeLPPP films with low concentration of permanent dipoles, the quadratic Stark effect dominated the EA response. In another report by Weiser and Horvath[94], several films of 4-BCMU (a polydiacetylene-based polymer) with varying amount of disorder were investigated. They found that for specially made ordered films, in which polymer chains were highly oriented and isolated within the single crystal of the monomer, $\Delta\alpha$ was dominated by the first derivative of absorption, i.e. by the quadratic Stark effect. Conversely, for the highly disordered films formed by spin-casting, the second derivative term, i.e. the linear Stark effect dominated $\Delta\alpha$, whilst the contributions of the first derivative and the transfer of oscillator strength were much smaller. This demonstrated clearly that the linear

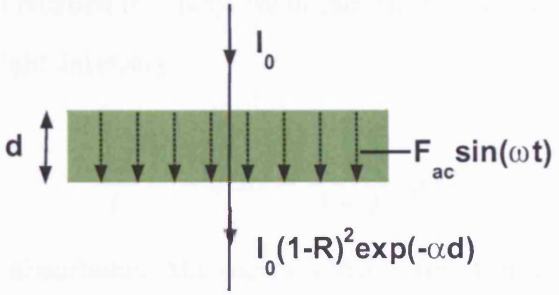

Figure 2.3: An optical beam with an initial intensity I_0 passing through a semiconducting material with thickness d, absorption coefficient α, and the reflection coefficient R (assumed to be the same at both interfaces). The broken vertical arrows indicate the orientation of the electric field applied across the film.

Stark effect is highly sensitive to disorder. Interestingly though, the quadratic Stark effect was very similar in both the ordered and the disordered film, implying that the quadratic Stark effect is much less sensitive to disorder. (According to the authors, this arose because even in the disordered films the homogeneous chain segments, reported to be between 2.5 and 5 nm, were larger than the exciton size, which was found to be 2.5 nm[94].)

2.3 Electromodulation of an Optical Beam

In an EA experiment, the intensity of an optical beam passing through the active layer is modulated via the Stark effect. The dependence of intensity I on the absorption coefficient α is given by[55,83]

$$I = I_0(1-R)^2 e^{-\alpha d}, \tag{2.17}$$

where I_0 is the intensity of the beam just before it enters the material, R is the reflection coefficient (assumed to be the same at the front and back surfaces) and d is the thickness. The change in intensity I due to an applied field F is given by the partial derivative of equation 2.17, yielding[55,83]

$$\frac{\partial I}{\partial F} = -I_0 e^{-\alpha \cdot d}[d(1-R)^2 \frac{\partial \alpha}{\partial F} + 2(1-R)\frac{\partial R}{\partial F}]. \tag{2.18}$$

Dividing by the unperturbed intensity, we obtain the fractional field-induced change in the transmitted light intensity

$$\frac{\Delta I}{I} = -[d\Delta\alpha + \frac{2}{(1-R)}\Delta R]. \tag{2.19}$$

For sufficiently high absorbance, the second term in equation 2.19 can be neglected, which yields[55,83,95]

$$\frac{\Delta I}{I} = -d\Delta\alpha. \tag{2.20}$$

If we combine equations 2.15 and 2.20 we obtain the dependence of ΔI/I on the electric field;

$$\frac{\Delta I}{I} = -dG(h\nu)F^2. \tag{2.21}$$

For an electric field of the form $F = F_0 + F_{ac}sin(\omega t)$, where F_0 and F_{ac} are respectively dc and ac fields, we have

$$\frac{\Delta I}{I} = -dG(h\nu)[(F_0^2 + \frac{F_{ac}^2}{2}) + 2F_0F_{ac}\sin(\omega t) - \frac{F_{ac}^2}{2}\cos(2\omega t)]. \tag{2.22}$$

Thus, due to the presence of dc and ac fields, $\Delta I/I$ is modulated at frequency 1ω (the first harmonic) and 2ω (the second harmonic). (In the absence of the dc field only the second harmonic component is generated.) We can write the two components individually as

$$\frac{\Delta T}{T}(1\omega) = -2dG(h\nu)F_0F_{ac}\sin(\omega t), \tag{2.23}$$

$$\frac{\Delta T}{T}(2\omega) = dG(h\nu)\frac{F_{ac}^2}{2}\cos(2\omega t), \tag{2.24}$$

with $\Delta I/I$ replaced by $\Delta T/T$ since the latter is commonly used in the literature[72].

In a PLED, assuming a charge-free active layer, the ac field equals the applied ac voltage (V_{ac}) divided by the film thickness d, i.e. $F_{ac} = V_{ac}/d$. Also, the dc field, determined by both the applied dc voltage (V_{dc}) and the built-in voltage (V_{BI}), is

given by $F_0 = (V_{dc} - V_{BI})/d$[55,72]. The first- and second-harmonic signals are therefore respectively given by

$$\frac{\Delta T}{T}(1\omega) = -2\frac{G(h\nu)}{d}(V_{dc} - V_{BI})V_{ac}\sin(\omega t), \tag{2.25}$$

$$\frac{\Delta T}{T}(2\omega) = \frac{G(h\nu)}{d}\frac{V_{ac}^2}{2}\cos(2\omega t). \tag{2.26}$$

Note that, according to equation 2.25, the first harmonic EA signal is nulled when the applied dc bias equals the built-in voltage. Therefore, EA can be utilised to probe the built-in voltage and, importantly, gain information about energy level alignment across the PLED heterostructure.

2.4 Previous Examples of PLED Characterisation by EA

The first extensive measurements of internal fields in organic light-emitting diodes (OLEDs) using EA were reported by Campbell *et al.* in 1995[86]. The authors measured the electric field in a multi-layer OLED, and showed that in the forward bias the field was non-uniformly distributed between the different layers due to the charge accumulation at the interfaces. One year later, in 1996, Campbell *et al.* reported V_{BI} measurements in a series of single-layer PLEDs, consisting of poly[2-methoxy, 5-(2'-ethyl-hexyloxy)-1,4-phenylene vinylene] (MEH-PPV) sandwiched between two metal contacts[72]. By employing several different metal contacts, the dependence of V_{BI} on the electrode work function (W_F) was tested. For electrodes with work functions positioned within the MEH-PPV bipolaron energy gap, V_{BI} was found to correspond closely to the difference between the metal work functions;

$$V_{BI} \approx \frac{W_F(anode) - W_F(cathode)}{e}, \tag{2.27}$$

where W_F(anode) and W_F(cathode) are work functions of hole and electron injecting contacts respectively. Interestingly, for an electrode work function positioned outside

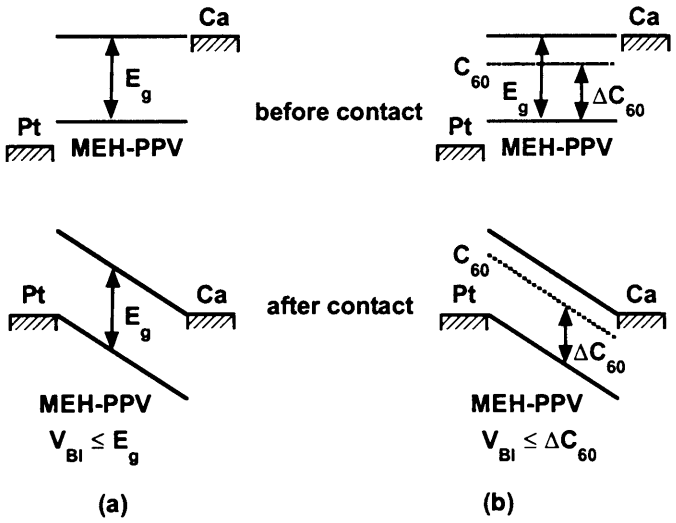

Figure 2.4: Schematic illustration of the built-in potentials in (a) undoped and (b) C_{60} doped MEH-PPV. The upper panels show the relative alignment of MEH-PPV polaron levels, the electron acceptor level of C_{60}, and the Fermi levels of Pt and Ca metals before the metals and the polymer are in contact. The lower panels show the built-in potentials for the structures after contact. (Adapted from reference[74])

the bipolaron gap, charge transfer occurs between the bipolaron level and the metal, resulting in 'pinning' of the metal Fermi level to the polymer bipolaron level[77]. In this case, the effective work function of the 'pinned' electrode is determined by the polymer bipolaron level.

Another notable application of the EA method was to investigate the maximum V_{BI} in diodes with MEH-PPV doped with C_{60} molecules (such blends have enhanced photoconductivity and are of interest for photovoltaic and photoconductive applications)[74]. Due to pinning effects, the maximum V_{BI} is determined by the polymer bipolaron energy gap[77]. Interestingly, in MEH-PPV-only devices the maximum V_{BI} was $\sim$ 2.1 V, whereas in the doped devices it was $\sim$ 1.5 V. As illustrated in Figure 2.4[74], this was ascribed to pinning of the cathode Fermi level to the C_{60} electron acceptor level. In MEH-PPV-only devices the Ca Fermi level is close to the MEH-PPV electron acceptor level, whereas in devices with C_{60} the Ca Fermi level is pinned to the C_{60} acceptor level which is lower in energy. Consequently, the maximum V_{BI} in devices with C_{60} is lower since it is determined by the difference between C_{60} electron acceptor level and the lower MEH-PPV level (ΔC_{60} in Figure 2.4).

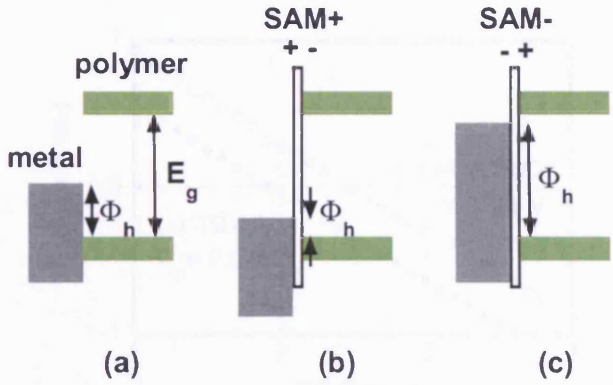

Figure 2.5: Schematic energy level diagram of metal-polymer interfaces: (a) untreated interface; interface with a dipole layer which (b) decreases, or (c) increases the energy barrier for hole injection (Φ_h). (Adapted from Campbell *et al.*[96])

EA was also instrumental in measuring V_{BI} in PLEDs with self-assembled monolayers (SAMs) which were used to alter the anode work function[73,96]. In these reports by Campbell *et al.*, thiol-based SAMs with an intrinsic electric dipole moment were inserted on top of Ag[96] and Cu[73] surfaces, as illustrated in Figure 2.5. Depending on the SAM type, the hole injection energy barrier (Φ_h) could be either decreased (Figure 2.5b), or increased (Figure 2.5c). Due to the change in the effective anode work function the first harmonic EA nulling voltage was observed to increase (or decrease) by as much as 0.5 V, corresponding to Φ_h altering by 0.5 eV.

Another valuable application of the EA method was to measure the reduction in Φ_h when the anode material was changed from ITO to ITO/PEDOT:PSS[75]. Figure 2.6 shows the measured first harmonic EA response as a function of dc bias, in devices with and without PEDOT:PSS. The voltage at which EA is nulled is larger by $\sim$ 0.5 V in the former than in the latter. Since this voltage corresponds to the built-in voltage, this indicates that the insertion of PEDOT:PSS reduces Φ_h by $\sim$ 0.5 eV.

EA was also employed in investigations of electron injection barriers (Φ_e), in PLEDs with ultrathin layers of lithium fluoride (LiF)[97], inserted between a blue-emitting polyarylene and the cathode, which was either Al[98] or Ca/Al[99,100]. ITO/PEDOT:PSS was used as the anode. In the first instance, the authors varied

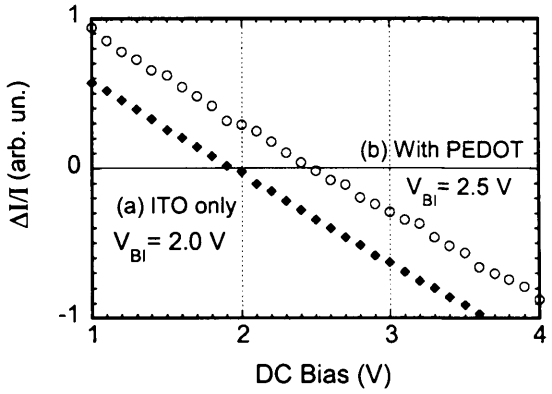

Figure 2.6: Electroabsorption response at 2.95 eV (V_{ac} = 1 V) as a function of applied dc voltage for (a) ITO/PDPV/Ca/Al and (b) ITO/PEDOT:PSS/PDPV/Ca/Al structures. The bias at which the response is null corresponds to the built-in potential V_{BI}. (from [75])

the LiF thickness and found that V_{BI} increases progressively, from 1.2 V at 0 nm to 2.3 V at 7 nm, and remains constant for higher thicknesses, up to 11 nm[98]. This corresponded to a decrease in Φ_e of 1.1 eV, which was evidenced in increased PLED brightness and efficiency. Subsequently, several additional cathode types were investigated, including LiF/Ca/Al and Ca/Al[99,100]. The results are shown in Figure 2.7, where the PLED V_{BI} is shown together with the operating voltage V_{OP} (applied dc voltage at which luminance equals 100 cdm^{-2}). As can be seen, V_{OP} decreases with increasing V_{BI}, due to the lowering of the electron injection barrier. Importantly, LiF/Ca/Al cathodes resulted in the highest V_{BI} (2.7 V), and the lowest V_{OP}.

Another notable employment of EA was reported by Poplavskyy *et al.*, who investigated an ITO/PEDOT:PSS/poly(9,9-dioctylfluorene)(PFO)/Al device kept in a vacuum chamber[101]. When the device was pre-conditioned by applying a dc voltage above the electroluminescence onset voltage, the device current (in the subsequent application of the dc bias) increased substantially. EA measurements revealed that V_{BI} increased from 1.9 to 2.1 V due to pre-conditioning, reportedly as a result of electron trapping near the PEDOT:PSS/PFO interface, which generates an interfacial dipole thereby lowering the hole injection barrier (and increasing V_{BI})[101].

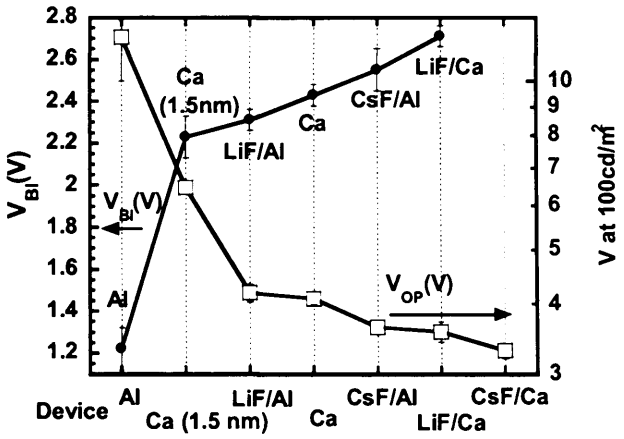

Figure 2.7: V_{BI} and V_{OP} (operating voltage at which luminance equals 100 cdm^{-2}) of PLEDs with several different cathode types. Note that V_{BI} of CsF/Ca devices could not be assessed accurately due to the presence of space charge in the active layer, formed by disassociation of CsF[55]. (from Brown *et al.*[100])

Interestingly, according to Lane *et al.*[102], and similarly Brewer *et al.*[103], the existence of such traps (which were also reported by van Woudenbergh *et al.*[104]) may lead to screening of the electric field in the active layer. Using EA, Lane *et al.* studied the internal electric field in *operating* PLEDs. Figure 2.8 shows the measured variation of the first and second harmonic EA signal with the applied dc bias. Up to 2.2 V, the first harmonic signal decreases linearly with the dc bias, as expected from equation 2.25. At higher voltages, at which charge injection occurs, the first harmonic EA signal remains close to zero, indicating that the injected charge completely screens the electric field. According to Brewer *et al.*[103], this can be explained by a mathematical model which assumes the presence of electron traps near the anode-polymer interface (their existence was also conjectured by van Woudenbergh *et al.*[104] and Poplavskyy *et al.*[101]). Figure 2.9, redrawn from [103], shows the energy level diagram at high forward bias in a conventional PLED (with non-zero electric field) and in a trap-rich PLED (with zero field in the bulk of the active layer). In the trap-rich PLED, the electrons trapped near the anode-polymer interface generate a dipole which lowers the hole injection barrier and enhances hole injection. Note that since the field in the polymer bulk is zero, the charges here

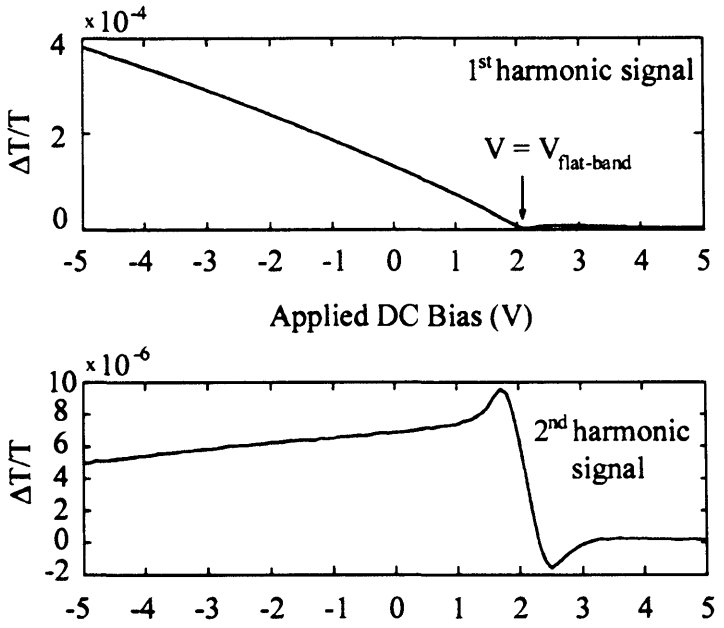

Figure 2.8: The dc bias dependence of the first and second harmonic EA signal of an ITO/PEDOT:PSS/Emitting-Polymer/Ca/Al LED, measured at 490 nm. Up to $\sim$ 2.2 V the first harmonic signal varies linearly with dc bias, as expected from equation 2.25. Above 2.2 V the first harmonic signal is approximately zero, indicating full screening of the internal field. The second harmonic signal also falls to zero at 2.2 V indicating full screening of the ac field. (Note that field screening has so far only been observed in PLEDS containing PEDOT:PSS, suggesting that traps may be a result of interactions between polyfluorene and PEDOT:PSS.) (From Brewer *et al.*[103])

move by diffusion rather than being field driven.

In another interesting example, EA has been used to investigate the operating method of light-emitting electrochemical cells (LECs)[105,106], which is still a subject of debate. LECs have a similar structure as PLEDs, but differ in the composition of the active layer, which apart from a luminescent polymer also contains a salt, e.g. lithium triflate-$LiCF_3SO_3$, and an ionically conducting polymer, e.g. PEO-poly(ethylene oxide). Two different operating models of these devices have been proposed; by Pei *et al.*[105,106], and deMello *et al.*[107,108]. Each of the models predicts a particular distribution of the internal electric field, and field measurements using EA have been employed by both Gao *et al.*[109], and deMello *et al.*[108], to validate their particular model.

As LECs are intriguing devices, particularly since they offer the prospect

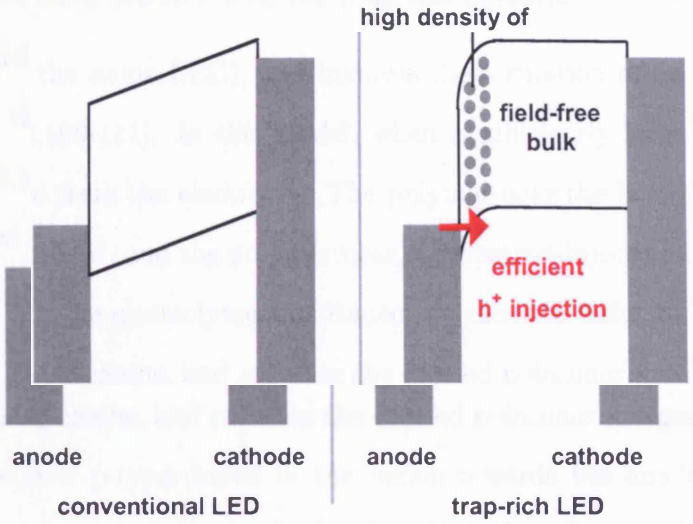

Figure 2.9: Schematic diagram comparing a conventional (trap-free) PLED with a trap-rich PLED containing a high density of trapped electrons close to the anode. At high forward bias, in the trap-rich PLED, the electrical field in the polymer bulk is close to zero, unlike in conventional PLED, where high electric fields are present. Redrawn from Brewer *et al.*[103].

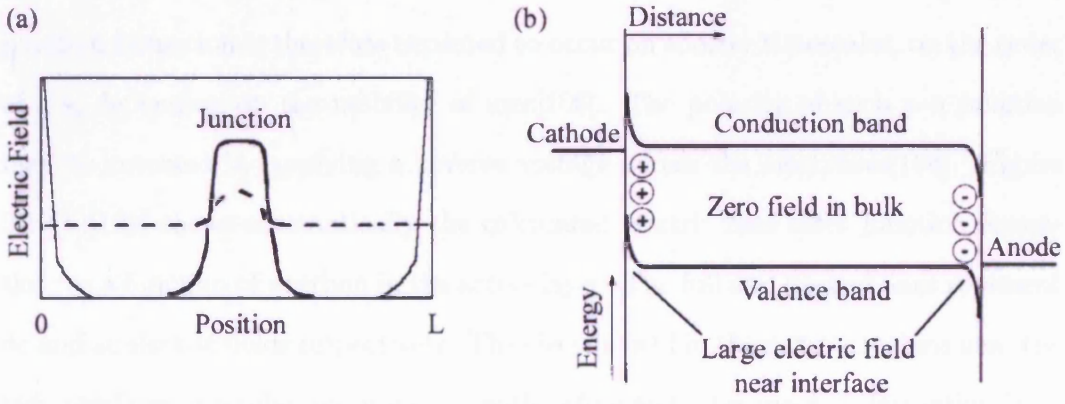

Figure 2.10: (a) Schematic illustration of the calculated dc (solid line) and ac (dashed line) electric field in the active layer, as a function of position, after electrochemical junction formation, in the model by Pei *et al.*[106] (from reference [109]). (b) Schematic energy level diagram for an LEC operating in forward bias in the model proposed by deMello *et al.*[107], which does not involve polymer doping, but is based on high interface dipoles formed by ionic space-charge. (from reference [107])

of nearly ohmic electrode-polymer contacts independent of the electrode work functions[108,109], we shall describe here the proposed operating mechanisms in more detail. The model of Pei *et al.* is based on electrochemical doping of the emitting-polymer (hence the name LEC), and involves the formation of an electrochemical junction[105,106,109-111]. In this model, when a sufficiently large bias is applied, charge is injected from the electrodes. The polymer near the hole-injecting contact thus becomes oxidised, and the polymer near the electron-injecting contact reduced. Counterions from the electrolytes simultaneously move in order to compensate the charges on polymer chains, and stabilise the formed polaronic charges. As a result, the polymer becomes p-type doped in the region towards the anode, and n-type doped in the region towards the cathode. Provided that the doped polymer is a good conductor, such as PPV, both regions are electrically conductive, and the field inside the doped regions is close to zero. As the applied bias is maintained, both p- and n-doped regions expand towards each other, and eventually meet forming an electrochemical junction (where electronic carriers are depleted by recombination). In one report, where a 1.5 mm thick active layer was used, junction formation reportedly occurred after 18 minutes of an applied bias of 140 V[111]. However, the active layer thickness is typically much smaller than this, on the order of 300 nm[109], and junction formation is therefore expected to occur on shorter timescales, on the order of 1 s, depending on the mobility of ions[106]. The polarity of such p-n junction may be reversed by applying a reverse voltage across the electrodes[106]. Figure 2.10(a)[109] shows schematically the calculated electric field after junction formation, as a function of position in the active layer. The full and dashed lines represent dc and ac electric fields respectively. The electric field in the narrow regions near the two interfaces is similar and non-zero both before and after junction formation[109]. However, as shown in the graph, the electric field in the p-n junction is large after junction formation (whereas before it was zero). Thus, it may be expected that the electroabsorption response will increase significantly following junction formation. Indeed, Gao *et al.* reported a large and an abrupt increase of both the first and the second harmonic EA signal for dc biases above $\sim$ 1.7 V, in a 260 nm device[109].

In contrast to this model, deMello *et al.*[107,108] do not envisage electronic doping of the conducting polymer, nor the formation of a p-n junction. Instead, in their model, the dissolved salt ions accumulate close to the electrodes due to the applied electric field and, for an ionic density greater than 10^{20} cm^{-3}, the charges screen the field from the bulk of the polymer layer, giving rise to a flat band across the bulk of the polymer layer. However, near the contact interfaces the field is large, and injection barriers are lowered, resulting in ohmic contacts. Consequently, at high forward bias, carrier density is high near the interfaces and, as a result, electrons and holes move towards each other by diffusion (leading to subsequent exciton formation and emission of light). As illustrated in Figure 2.10(b), which shows a schematic energy level diagram proposed by deMello *et al.*, the field in the bulk of the polymer is zero (in contrast to the junction formation model). The applied field is dropped in the narrow regions near the interfaces, whose thickness is of the order of 10 Å for ionic density greater than 10^{20} cm^{-3}[107]. To test their model, the authors applied forward bias and then cooled LECs to below the glass transition temperature of the polymer electrolyte (200 K)[108]. Then, using EA, they could probe the electric field generated by the frozen ion distribution. As explained in reference[108], this confirmed that the field was zero before the devices were cooled.

Another valuable study of PLEDs using EA was reported by Giebeler *et al.*, who investigated degradation effects in non-encapsulated PLEDs based on MEH-PPV[112], and poly(2,5-dialkoxy-p-phenylene vinylene) (PDAOPV)[113]. The authors found that the dc bias dependence of the first EA harmonic became non-linear after electrical stressing in air. This was explained by the formation of space charge in the active layer, introduced during electrical driving by the diffusion of impurities (for example, by oxygen and moisture from air) which trap electronic charges. Upon application of an electric field, the trapped charges generated a counter field, which could be observed since it affected the magnitude as well as the sign of the EA response[112,113]. The authors also reported a V_{BI} increase resulting from electrical stressing, reportedly due to formation of gaseous bubbles at the Al electrode[113].

Other examples of PLED characterisation by EA include measurements of band

bending in MEH-PPV-based devices containing an insulating layer[114], and a demonstration of a polarisation sensitive electromodulation technique that discriminates between interface and bulk effects[115]. Also, Liess *et al.* reported a method for monitoring the onset of both hole and electron injection, via changes in the EA signal induced by field screening of the injected charge[116].

Chapter 3

Electroabsorption Experimental Set-Up

This chapter describes the electroabsorption (EA) experimental set-up used in the course of this work. We first describe the main components, including the light source, monochromator and photodetector, and then discuss the measurement procedure. To assess the precision of the spectrometer, we measure the EA response of a simple polymer light-emitting diode, and compare the results with the theory outlined in Chapter 2. Once the validity of the spectrometer is established, we investigate the EA signal-to-noise ratio, and demonstrate a method for reducing the noise that appears during high frequency measurements. We also investigate the variation of the EA nulling voltage (i.e. the applied dc voltage required to null the first harmonic EA response) between different pixels and different devices, and assess the accuracy with which the built-in voltage can be measured.

3.1 Overview

In an electroabsorption (EA) experiment, a modulating electric field with frequency ω is applied across the sample, producing Stark modulation of the absorption coefficient. As a result, the intensity of an optical beam passing through the sample is modulated with frequency ω. Typically, in characterisation of polymer light-emitting diodes (PLEDs) by EA, the fractional change in the light intensity is small, often

between 10^{-5} and 10^{-4}, so that high fields (on the order of 10^7 Vm^{-1}) need to be applied.

A schematic representation of the EA spectrometer utilised in this research, set up by Brown[55], is shown in Figure 3.1. The light is generated by a Xenon lamp which produces a broad spectrum of white light, which enters a monochromator thus narrowing the energy band to a few tens of meV. An automatically controlled shutter is placed at the monochromator exit, to reduce the unnecessary exposure to light which can potentially photodegrade the sample. With the shutter open, the beam exiting the monochromator is focused by a lens onto the PLED where, after transmission through the glass substrate and the transparent electrode, it enters the polymer film at an angle of incidence close to 45^0. After passing through the polymer film the beam is reflected off the metallic electrode back into the polymer layer, so that it exits the device after again passing through the transparent electrode and the glass substrate. Using a second lens, the beam is then focused onto a photodiode. Where necessary, an optical filter (or a compact monochromator) is inserted in front of the photodetector, to screen from unwanted photoluminescence (PL), or in some cases electroluminescence (EL). The signal generated in the photodetector is measured by two dedicated lock-in amplifiers (Stanford Research SR-830) and a dc meter (Keithley 199), with each of the lock-in amplifiers measuring either the first or the second harmonic ΔT component. For both ΔT components the EA signal (ΔT/T) is calculated by dividing the lock-in signal with the dc meter signal (T).

Both the ac voltage, $V_{ac}\sin(\omega t)$, and the dc voltage, V_{dc}, are provided by one of the lock-in amplifiers, and added by a custom-made summing amplifier[55], before being applied to the PLED. Several components, including the monochromator, shutter, lock-in amplifiers and dc meter, are interfaced to a computer to allow automated operation of the experiment. The software was designed with LabVIEW graphical development package by Brown[55], and by the author.

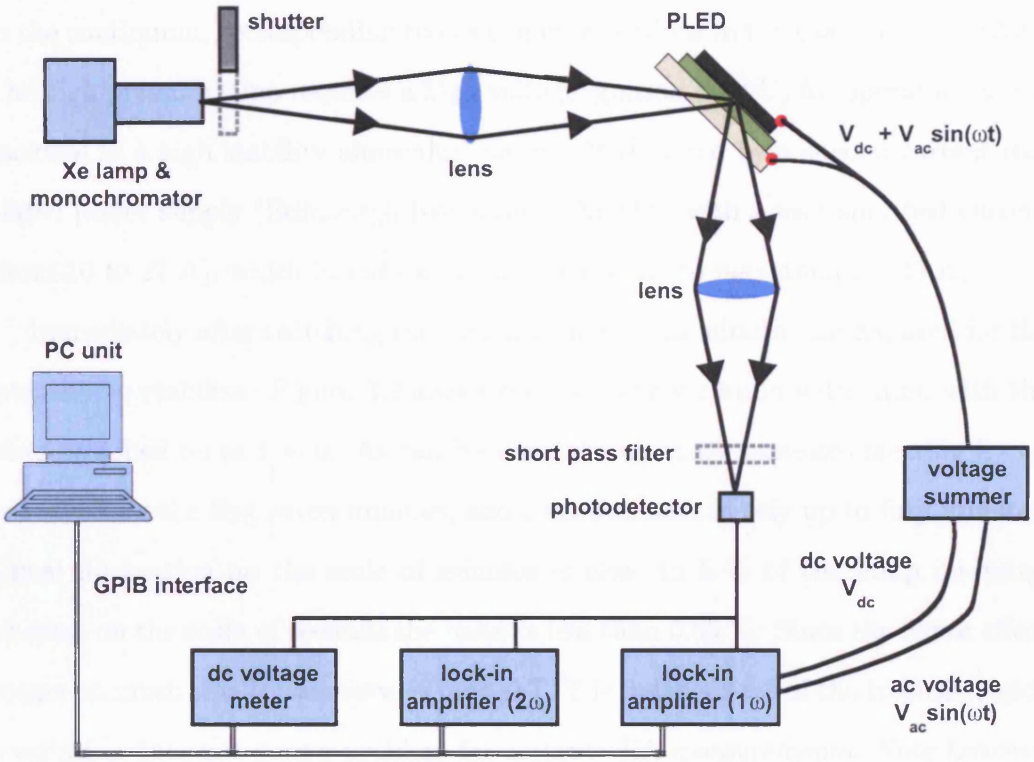

Figure 3.1: Schematic illustration of the electroabsorption system used in this thesis. Please see text for discussion.

3.2 Description of the Spectrometer's Critical Components

3.2.1 Xe Lamp[55,117]

A high intensity 450 W xenon arc lamp (OSRAM XBO 450W OFR) was employed as the light source. It has a continuous emission spectrum in the ultra-violet, visible and near infrared range (from 190 nm to 2600 nm). It operates by the passage of current through the xenon gas, and produces a number of discrete lines, in addition to the continuum, corresponding to electronic transitions in the gas (see Figure 3.3). The high pressure lamp requires a high voltage ignition (33 kV) for operation and is enclosed in a high stability aluminium casing. It is driven by a special current regulated power supply (Edinburgh Instruments Xe900), with a user specified current (from 10 to 27 A), which in our experiment was close to maximum ($\sim$ 25 A).

Immediately after switching the Xe lamp on, several minutes are required for the intensity to stabilise. Figure 3.2 shows the intensity variation with time, with the lamp switched on at t = 0. As can be seen, the intensity increases steadily by up to $\sim$ 20 % in the first seven minutes, and then decreases slowly up to fifty minutes. Signal fluctuation on the scale of minutes is close to 5 % of the lamp intensity, whereas on the scale of seconds the noise is less than 0.05 %. Since the Stark effect occurs on much smaller time-scales, and $\Delta T/T$ is independent of the intensity, such a variation does not pose a problem for accurate EA measurements. Note however that the software running the experiment is written so that the dc reading and the lock-in reading are taken in the space of $\sim$ 1 s, and the user needs to be aware that the calculated $\Delta T/T$ signal may be potentially affected if the time constant for ΔT measurements is higher than a few seconds.

3.2.2 Main Monochromator[55,118]

A schematic drawing of the main monochromator (Bentham M300EB) is shown in Figure 3.3(b). Its calibration was certified by the manufacturer, and was further checked by the author using a calibrated Ocean Optics S2000 UV-VIS Spectrometer.

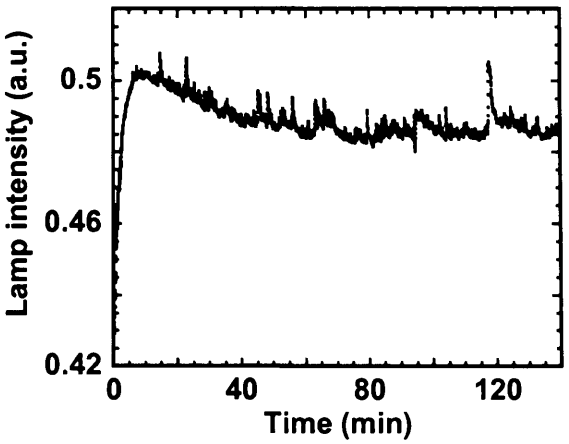

Figure 3.2: Variation of Xe lamp intensity with time immediately after switching on at t = 0. The intensity was measured after passing the light, centred at 500 nm (2.49 eV), through the monochromator.

The monochromator has a variable-width entrance and exit slits which are 20 mm high, and is fitted with a single 1800 lines/mm diffraction grating which can provide an output in the energy range from zero order to 900 nm. The width of both the exit and entrance slits was set between 1 and 2 mm as it was found that this gives sufficiently high light intensity, whilst the bandwidth of the exit beam is kept below 4 nm. A rotating wheel carrying several optical filters, whose purpose is to select the appropriate filter for blocking higher order wavelengths at specific regions of the spectrum, is located inside the monochromator. Both the output wavelength and the filter are controlled via a separate control unit located outside of the main monochromator housing. The unit can be operated either manually or automatically via a computer, for which custom-made software was developed by Brown[55] and the author. The optical spectrum of the beam exiting the monochromator (detected by a silicon diode) is shown in Figure 3.3(a).

3.2.3 Photodetector

Due to the required sensitivity, the photodetector is a particularly important part of the experimental set-up, and must be able to minimise noise effects. The system we used was developed by Brown[55], and consists of a Hamamatsu Photonics

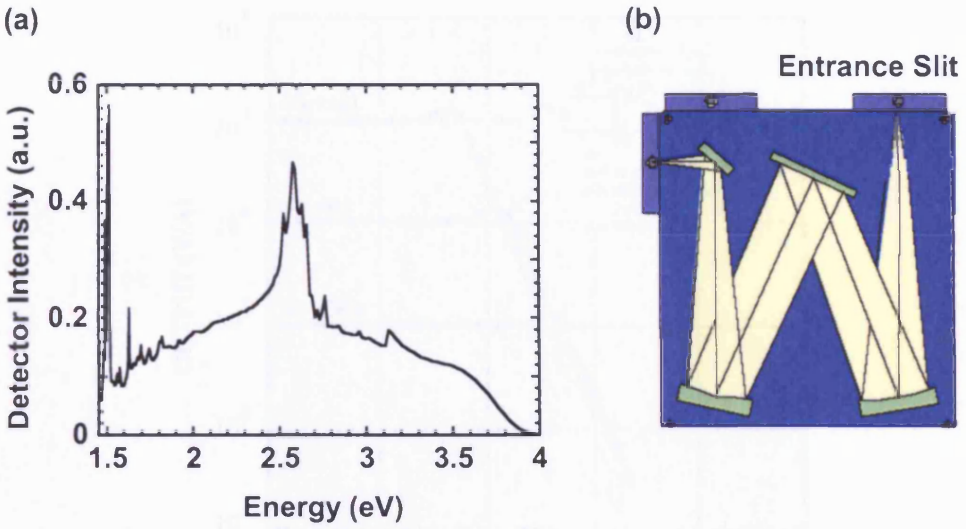

Figure 3.3: (a) Intensity vs energy spectrum of the Xe-900 lamp with main monochromator, detected by a silicon photodiode. (b) Schematic of the main monochromator (Bentham M300EB) used in EA experiments (from [118]).

S1406 UV-enhanced silicon photodiode, whose characteristics are well matched for the measurements presented in this thesis. Its spectral response is in the range 190 - 950 nm, and the active area (5.7 mm^2) is comparable to the cross sectional area of the probe beam at the focus[119]. It incorporates a high-speed operational amplifier, located close to the photodiode for an effective minimisation of noise. The package was placed inside a metallic enclosure in order to screen from external electromagnetic fields. Figure 3.4 shows the frequency response of the photodiode/operational amplifier combination at different values of the feedback resistance R_f[119]. The inset shows a schematic diagram of the corresponding electronic circuit. In our photodetector, the feedback resistance was $\sim 0.6\ M\Omega$, whereas the feedback capacitance C_f (used to reduce high frequency noise, and oscillations if $R_f < 100\ k\Omega$[119]) was zero[55]. In Figure 3.4 the frequency response at $R_f = 1M\Omega$ is flat up to $\sim$ 40 kHz, but at higher frequencies the response is non-constant and varies with frequency. Thus, from the data in Figure 3.4, and from the author's experience, it is expected that accurate EA measurements can be taken up to 40 kHz, whereas at higher frequencies the photodetector response needs to be taken into account. In our experiments, the frequency was typically close to 1 kHz, which is well within the capabilities of the photodetector. We also tested the photodetector at higher

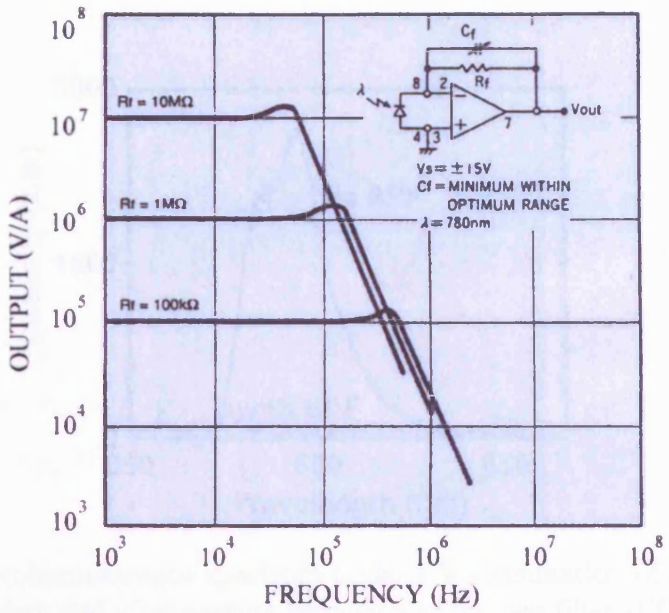

Figure 3.4: The frequency response of the photodiode with a built-in operational amplifier (Hamamatsu S1406), for different values of the feedback resistance R_f. The inset shows a schematic of the corresponding electronic circuit. (From [119])

frequencies, up to 100 kHz, and the results are presented in section 3.3.1.

3.2.4 Photoluminescence Screening

In EA experiments involving blue-emitting polyfluorenes (F8, TFB, PFB), a noticeable but small PL signal was generated at incident photon wavelengths below 420 nm. Typically, near 420 nm, the PL signal in PFB was $\sim$ 1 % of the EA signal, whereas in F8 and TFB PL was much smaller ($<$ 0.1 %). Where necessary, a short pass optical filter (SPF) (or in some cases a compact monochromator) was placed in front of the photodetector to reduce the PL signal. Figure 3.5 shows the PL spectrum of a blue-emitting polyfluorene before and after passing through the short pass filter (COMAR 435 IK), whose pass band is 390 - 415 nm, with $\sim$ 70 % transmission at 420 nm, and $\sim$ 50 % transmission at 435 nm[120]. As can be seen, the filter blocks off most of the PL ($>$ 90 %) signal. Thus, with the filter, which could be applied for incident wavelengths shorter than 435 nm, we found that the PL signal was small and did not significantly affect EA measurements. Although a compact monochromator (Digikrom CM110) was also available for PL screening, it

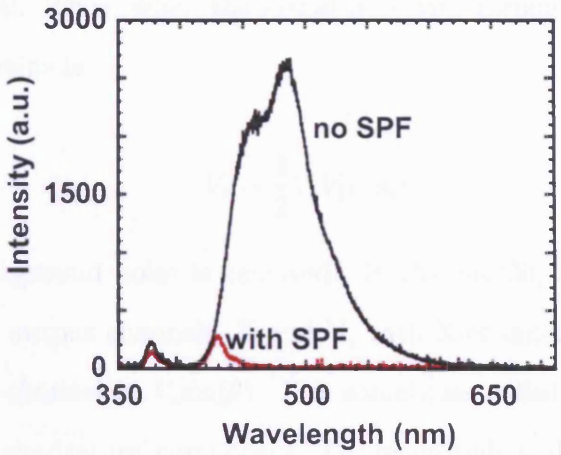

Figure 3.5: Photoluminescence spectrum under UV illumination of a blue-emitting polyfluorene, before and after passing through a short pass filter (COMAR 435 IK). The spectrum was recorded using Ocean Optics S2000 UV-VIS spectrometer.

was not as convenient to use as it significantly reduced the intensity of the probing beam.

3.2.5 ΔT Detection Using a Lock-In Amplifier

As already mentioned, since the sinusoidal signal generated in the photodetector due to the Stark effect (ΔT) is small, a lock-in amplifier (Stanford Research SR830 DSP) was employed to detect the signal. Here we consider its principle of operation.

Suppose that the signal we are trying to measure is[121]

$$V_{sig}=V_s \sin(\omega_s t + \theta), \tag{3.1}$$

where V_s is the signal amplitude and θ is the phase relative to the lock-in reference phase. The lock-in can separate the signal from noise many orders of magnitude larger, provided that noise does not oscillate with frequency ω. The lock-in first multiplies the signal with its reference voltage, $V_l \sin(\omega_l t)$, and the product $V_p = V_s V_l \sin(\omega_l t)\sin(\omega_s t + \theta)$ can be rewritten as

$$V_p = \frac{1}{2} V_s V_l [\cos((\omega_s - \omega_l)t + \theta) - \cos((\omega_s + \omega_l)t + \theta)]. \tag{3.2}$$

If the lock-in reference frequency ω_l equals ω_s, the first term in equation 3.3.1 becomes a dc signal. Thus, when the signal is passed through a low pass filter the signal which remains is

$$V_p = \frac{1}{2} V_s V_l \cos(\theta), \tag{3.3}$$

whereas the background noise is removed. In the SR830, the measured signal is displayed in two output channels, X and Y, with X-channel being proportional to $V_s \cos(\theta)$, and Y-channel to $V_s \sin(\theta)$. X is sometimes called the 'in-phase' component, and Y the 'quadrature' component. The magnitude and phase of the measured signal are then equal to $\sqrt{X^2 + Y^2}$, and $\tan^{-1}(\mathrm{Y/X})$ respectively.

3.3 Electroabsorption Measurements of an ITO/ Polymer/Al Device

To test the precision of the EA spectrometer, we measured the EA response of an ITO/EP/Al PLED, where EP (emitting-polymer) is a polyfluorene-based blue emitter. We then assessed whether or not the measured response is in agreement with the EA equations 3.4 and 3.5[72], obtained previously in Chapter 2.

$$\frac{\Delta T}{T}(1\omega) = -2\frac{G(h\nu)}{d}(V_{dc} - V_{BI})V_{ac} \sin(\omega t) \tag{3.4}$$

$$\frac{\Delta T}{T}(2\omega) = \frac{G(h\nu)}{d}\frac{V_{ac}^2}{2} \cos(2\omega t) \tag{3.5}$$

Note that these equations characterise the EA response of well behaved PLEDs, in which the polymer layer is free of significant concentration of space charge. In the presence of the latter, deviation from equations 3.4 and 3.5 can be expected. (For example see publications by Giebeler *et al.*[112,113].)

The devices we used were fabricated by Cambridge Display Technology (CDT), and provided to the author by Dr. Matthew Roberts. Fabrication followed the standard procedure (see Chapter 4, and also Brown *et al.*[75]), and included the

treatment of the ITO substrate with oxygen plasma. Finished devices were encapsulated with metal cans and epoxy resin to provide effective isolation from potentially damaging atmospheric gases such as oxygen and moisture. The PLEDs were made using state of the art clean room facilities, with high purity materials, and are therefore expected to have a low concentration of impurities and space charge in the active layer. Note that Brown, who investigated similar devices, reported that the concentration of charge in the active layer (below the onset of hole or electron injection) was small and did not significantly affect the uniformity of the electric field[55]. Also, our current-voltage measurements (not shown here), and visual inspection of photoluminescence under UV light, indicated that the devices were in good condition.

3.3.1 Results

EA vs Photon Energy, Voltage and Frequency

The measured EA spectrum of the ITO/EP/Al structure is shown in Figure 3.6, together with the absorption spectrum of the polymer. The main features of the EA spectrum, including the magnitude and the position of the two main peaks centred at 2.95 and 3.25 eV, are in qualitative agreement with the previously published EA spectra of blue-emitting polyfluorenes[100,122]. The EA onset coincides with the onset of absorption, but is much sharper, and reaches the maximum at 2.95 eV, where the absorption is still relatively low.

According to Campbell *et al.*[72], and also Brown *et al.*[55,100], EA vs V_{dc} and EA vs V_{ac} measurements are best taken in the vicinity of the EA maximum, since photoluminescence and charge generation are minimised here. Thus, we performed EA vs V_{dc} and EA vs V_{ac} measurements at the photon energy ($h\nu$) of 2.92 eV, indicated by the dotted vertical line in Figure 3.6. The results are shown in Figures 3.7 and 3.8.

As can be seen in Figure 3.7, the first harmonic EA response, $\Delta T/T(1\omega)$, is linearly dependent on V_{dc}, in accordance with equation 3.4, and crosses the V_{dc} axis at the nulling voltage (V_{null}) equal to 1.01 V. (Note that in equation 3.4 V_{null}

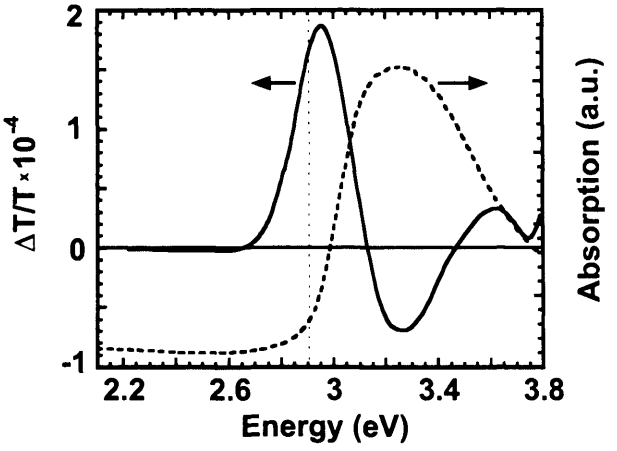

Figure 3.6: EA spectrum of the ITO/EP/Al structure (shown on the left-hand ordinate axis), measured at V_{dc} = 0 V, V_{ac} = 0.5 V, and frequency = 1 kHz. The absorption spectrum of the polymer (provided by Dr. Matthew Roberts of CDT) is shown on the right-hand ordinate axis.

corresponds to the PLED built-in voltage.) Also, the second harmonic EA response, $\Delta T/T(2\omega)$, remains constant over the V_{dc} range shown, as expected from equation 3.5. Furthermore, at $V_{dc} = 0V$ the experimental ratio EA(1ω)/EA(2ω) equals 7.9, which is consistent (within the experimental error) with equations 3.4 and 3.5 (whose ratio equals $8 \times V_{BI}$). Therefore, these results demonstrate that the measured EA vs V_{dc} dependence of both the first and the second EA harmonic is fully consistent with equations 3.4 and 3.5.

The EA vs V_{ac} dependence, shown in Figure 3.8, was measured at frequencies 1, 45 and 90 kHz. (Note that since the lock-in amplifier can only operate at frequencies up to 100 kHz the second harmonic response was not measured at 90 kHz.) The curves were fitted with a generic power law (V_{ac}^N) in order not to constrain the fit to the expected linear dependence for the first harmonic, or quadratic dependence for the second harmonic signal. At 1 kHz, the power coefficient N for the first and the second harmonic EA signal was found to be 1.0041 and 1.9685 respectively, indicating a very close fit. At 45 kHz, the first harmonic response was virtually identical, but at 90 kHz it deviated by approximately 4 %.

We also measured the dependence of the EA amplitude on frequency, with the

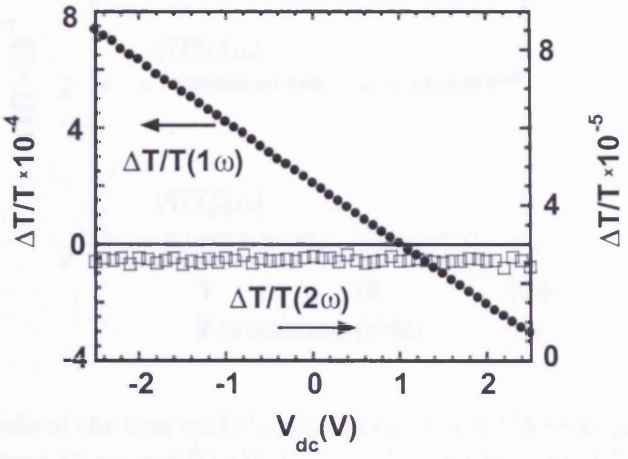

Figure 3.7: The first harmonic EA signal, $\Delta T/T(1\omega)$, and the second harmonic EA signal, $\Delta T/T(2\omega)$, versus the applied dc bias, measured at $h\nu = 2.92$ eV, $V_{ac} = 0.5$ V, and frequency = 1 kHz.

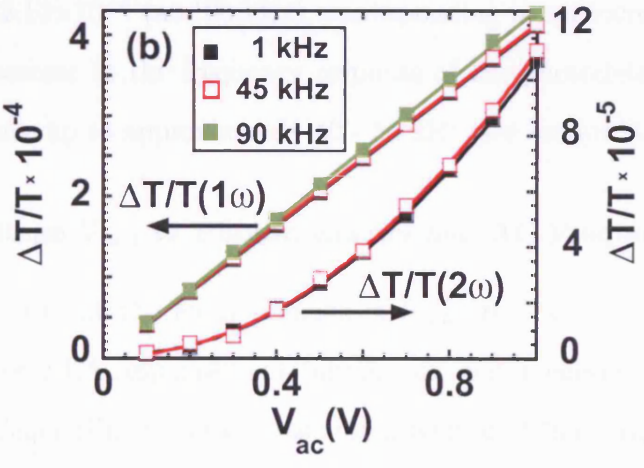

Figure 3.8: ΔT/T(1ω) and ΔT/T(2ω) versus V_{ac}, measured at $h\nu = 2.92$ eV, $V_{dc} =$ 0 V, and frequency = 1, 45 and 90 kHz.

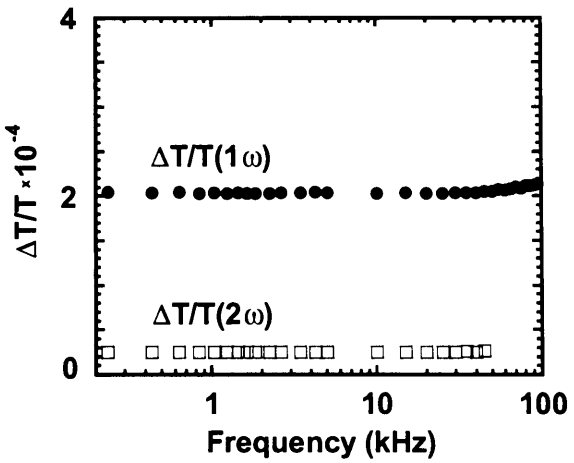

Figure 3.9: Amplitude of the first and the second harmonic EA response as a function of frequency, measured at $h\nu = 2.92$ eV, $V_{dc} = 0$ V, and $V_{ac} = 0.5$ V. (Note that in these, as in all other high frequency measurements, the photodetector ground was connected to the nearest earth.)

results shown in Figure 3.9. The first harmonic signal was measured up to 100 kHz, and the second harmonic signal was measured up to 50 kHz. For frequencies lower than approximately 40 kHz, both the first and the second harmonic response was constant, in accordance with equations 3.4 and 3.5 respectively. Above 40 kHz the amplitude of the first harmonic signal increased steadily from 2.05×10^{-4} (at 40 kHz) to a maximum of 2.14×10^{-4} (at 100 kHz), corresponding to an increase of $\sim$ 4 %. We ascribe this increase to the frequency response of the photodetector, which is expected to be linear up to approximately 40 - 50 kHz (see section 3.2.3).

The Nulling Voltage V_{null} vs Photon Energy and AC Frequency

In Figure 3.10 we present the measurements of V_{null} (the dc voltage required to null the first harmonic EA response) as a function of photon energy and frequency. The energy dependence (Figure 3.10a) was measured from 2.79 eV (near EA onset) to 2.99 eV (near EA peak), and V_{null} was found to be constant at 1.028 V, with a maximum interval of variation of $\pm$ 5 mV. The frequency dependence (Figure 3.10b) was measured from 1 to 96 kHz, and, similarly, V_{null} was found to be constant at 1.022 V, with a maximum interval of variation of $\pm$ 4 mV. Thus, these results are in

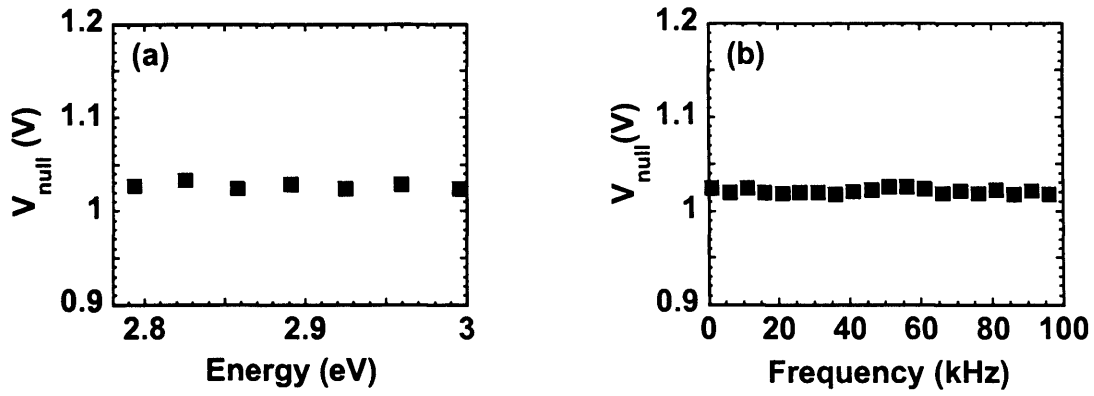

Figure 3.10: (a) V_{null} as a function of $h\nu$, measured at frequency = 1 kHz. (b) V_{null} as a function of frequency, measured at $h\nu$ = 2.92 eV.

agreement with EA equation 3.4, since V_{null} is expected to equal the built-in voltage, which is independent of both $h\nu$ and frequency.

3.3.2 Discussion

The measured dependence of the first and the second harmonic EA response on V_{ac} and V_{dc}, and on frequency (up to at least 40 kHz), is in excellent agreement with the theoretical model (equations 3.4 and 3.5). In addition, V_{null} was found to be independent of photon energy and frequency within the measured range, also in full accordance with the theoretical model. Thus, these the results demonstrate that the EA spectrometer can accurately measure the EA response of polymer light-emitting diodes. We remark that Brown, who constructed the experimental rig[55], and used it extensively in characterisation of PLEDs[75,98-100], only reported measurements for frequencies up to 5 kHz. The results presented here demonstrate that the spectrometer is capable of accurate measurements at significantly higher frequencies, up to at least 40 kHz. Above 40 kHz, due to the frequency response of the photodetector, the EA signal amplitude deviates progressively with increasing frequency, by $\sim$ 1 % at 60 kHz, and $\sim$ 4 % at 95 kHz.

Interestingly however, as already mentioned, V_{null} was constant over the whole measured range from 1 to 96 kHz, and had a variation of only $\pm$ 0.4 %, independent of frequency. Thus, the observed deviation of the EA signal above 40 kHz does

not seem to have a noticeable effect on V_{null}. We can explain this effect as follows. Assuming that the intensity of the light incident on the photodiode is of the form $V_{pd}\sin(\omega_s t + \theta)$ (with V_{pd} being zero when the PLED EA response is zero), the photodiode output signal (after amplification by the op amp) is $AV_{pd}\sin(\omega_s t+\theta+\varphi)$, where A is the amplification and φ is an additional phase shift introduced by the op amp[123]. The measured deviation of EA above 40 kHz is then presumably due to deviation of A above 40 kHz. We note from Figure 3.8 that at both 45 and 90 kHz the measured $\Delta T/T(1\omega)$ vs V_{ac} response is nearly perfectly linear, indicating that A is independent of V_{pd} magnitude (which increases linearly with V_{ac}). Similarly, $\Delta T/T(1\omega)$ vs V_{dc} response is also expected to be linear at any given frequency, up to at least 100 kHz. Thus, although A may deviate with frequency, V_{pd}, which is proportional to the first harmonic EA response generated by the polymer, is always nulled at the same dc bias independently of frequency. Thus, the measured V_{null} is independent of frequency.

3.4 EA Signal-to-Noise Ratio

To assess the signal-to-noise ratio in $\Delta T/T$ measurements, we measured the variation in time of both ΔT (the lock-in amplifier signal) and T (the dc meter signal). Measurements were performed at three sets of conditions: (1) with no light and with no applied voltage, (2) with light but no applied voltage, and (3) with light and with an applied ac voltage (V_{ac} = 0.5 V). Apart from the mentioned conditions the experiment was set-up as usual (e.g. see section 3.1). The structure of the tested device was ITO/PEDOT:PSS/EP/LiF/Ca/Al. The results are shown in Figure 3.11, where the lock-in signal is represented on the left-hand ordinate axis, and the dc meter signal on the right-hand ordinate axis.

For dark signal with no applied voltage (Figure 3.11a) the lock-in mean value is zero, as expected, with a maximum variation interval of $\pm$ 0.1 μV. The dc signal has a mean value of - 0.426 mV, and a maximum interval of variation of $\pm$ 0.005 mV. When the light is switched on, with no applied bias (Figure 3.11b), the lock-in mean value is zero, but the noise is slightly increased, and has a maximum interval

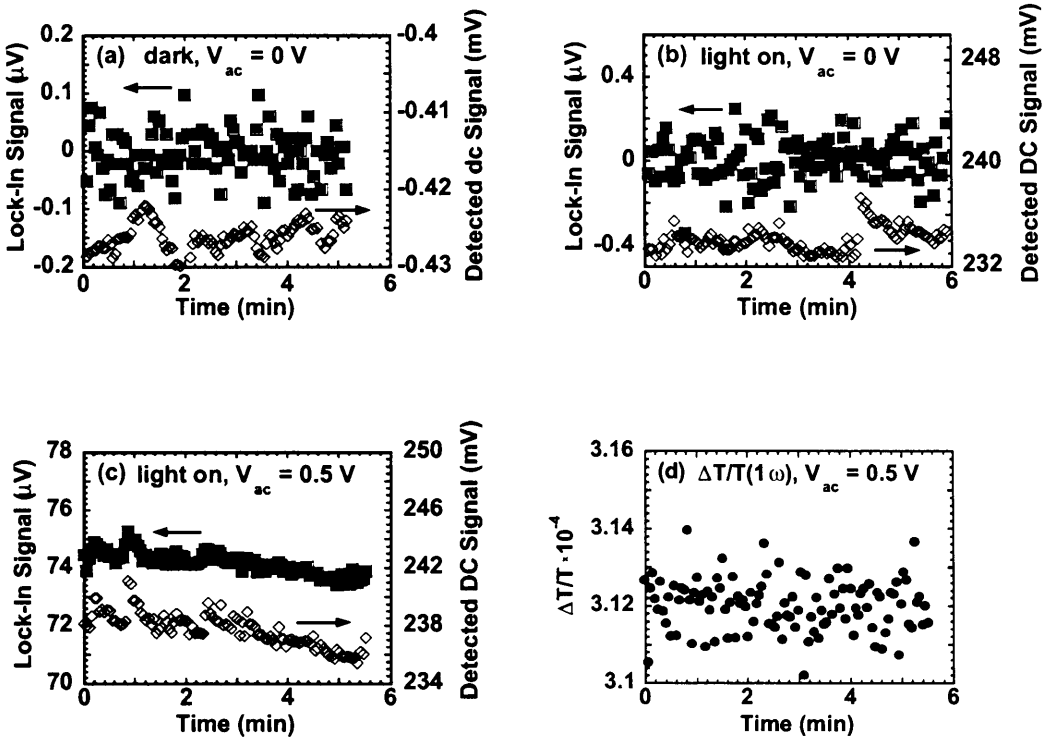

Figure 3.11: The measured variation of the lock-in signal (left-hand ordinate axis) and the dc meter signal (right-hand ordinate axis) in time, with (a) no light and no applied voltage, (b) with light and no applied voltage, and (c) with light and with an applied ac voltage V_{ac} = 0.5 V. (d) The lock-in signal divided by the dc meter signal, $\Delta T/T(1\omega)$.

of variation of $\pm$ 0.3 μV. The dc meter mean value is 234 mV, and the variation interval is $\pm$ 2 mV, the increase resulting from the variation of Xe lamp intensity with time. When ac voltage is applied (Figure 3.11c), the first harmonic lock-in signal equals $\sim$ 74 μV, and changes with time following the variation of Xe lamp intensity. When the lock-in signal is divided by the dc signal to produce ΔT/T(1ω) (Figure 3.11d), ΔT/T(1ω) is essentially constant, equalling $3.12\times10^{-4} \pm 2\times10^{-6}$. Note that the noise originates within the lock-in amplifier rather than in the dc meter.

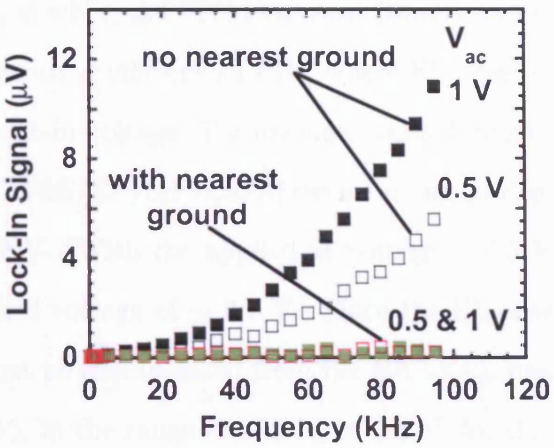

Figure 3.12: The first harmonic lock-in signal as a function of frequency, at no incident light, with V_{ac} = 0.5 or 1 V. No dc bias was applied.

3.5 Noise at High Frequency Measurements

In addition to the lock-in noise shown in Figure 3.11, another type of noise was present at higher frequencies, even in the absence of light. The measured lock-in signal in the dark as a function of frequency, at $V_{ac} = 0.5$ and 1 V, is shown in Figure 3.12. If the photodetector is not connected to the nearest ground, at $V_{ac} = 1$ V, the noise at 50 kHz is close to 3 μV, and at 100 kHz it is close to 10 μV. This is high enough to affect the accuracy of EA measurements at higher frequencies. However, if the photodetector is connected to the nearest earth, for frequencies below 50 kHz the noise is virtually eliminated to less than 0.1 μV, whereas at higher frequencies the noise is reduced to 0.2 - 0.3 μV. Thus, with the photodetector grounded to the nearest earth, this noise did not significantly affect EA measurements, even above 50 kHz. Incidentally, we note that the noise may be caused by minute synchronous ground currents.

3.6 Accuracy of V_{null} Measurements

In this section we describe the method for measuring V_{null}, and then investigate the accuracy with which V_{null} can be measured.

V_{null} is ideally measured by varying V_{dc} over a wide range, for instance from -3 to 4 V, and finding V_{dc} at which $\Delta T/T(1\omega)$ is zero. However, this is often not practical, especially when measuring efficient PLEDs, where EL onset occurs at applied voltages close to the built-in voltage. For example, considering the measured response of the ITO/PEDOT:PSS/EP/LiF/Ca/Al device shown in Figure 3.13, the EL onset occurs at $V_{dc} \sim 2.2$ V. (With the applied ac voltage of 0.5 V, this corresponds to the maximum applied voltage of ~ 2.7 V.) Since the EL onset occurs at V_{dc} lower than V_{null}, V_{null} must be extrapolated from the EA vs V_{dc} line. The inset in Figure 3.13 shows EA vs V_{dc} in the range -2.0 $\leqslant V_{dc} \leqslant$ 1.5 V, for six different 'scans', with virtually identical EA responses. V_{null} was extrapolated by Labview software, and the measured values (2.716, 2.726, 2.712, 2.716, 2.723, 2.718) are essentially the same in all six scans, with the mean value of 2.718 V, and the maximum variation interval of $\pm$ 8 mV.

Incidentally, these measurements were performed with the dc bias altered in steps of 0.1 V. When many V_{null} measurements are performed, it is convenient to increase the V_{dc} step in order to decrease the measurement time. In practice, we found that with the step of 0.5 V the measurement time is considerably reduced, whilst the accuracy is not significantly compromised. For instance, performing the same measurements as above, but with the dc step increased to 0.5 V, the mean V_{null} equals 2.718 V $\pm$ 11 mV.

To investigate the influence of noise on V_{null} accuracy, V_{null} was measured for a wide range of lock-in signal magnitudes: from $\sim 50\ \mu V$ (where EA signal is much larger than noise) to $\sim 0.2\ \mu V$ (where EA signal and lock-in noise are comparable). The lock-in signal was decreased either by reducing V_{ac}, or by decreasing the probe beam intensity via monochromator slit width. As can be seen in Figure 3.14, V_{null} is unchanged from 50 to 10 μV, equalling 2.72 V ($\pm$ 7 mV). When the signal is reduced to 5 μV, V_{null} equals 2.74 V ($\pm$ 29 mV), whereas at 1 μV V_{null} equals 2.77 V ($\pm$ 120 mV). At 0.2 μV V_{null} equals 2.89 V ($\pm$ 600 mV). Thus, for signals above 10 μV there is essentially no change in V_{null} accuracy. When the signal is lowered to 5 μV V_{null} varies by 0.7 %, whereas at 1 μV it varies by 2 %, and at 0.2 μV it varies

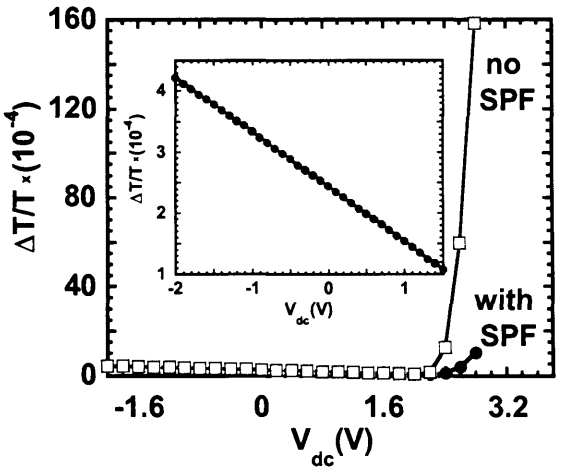

Figure 3.13: The measured $\Delta T/T$ vs V_{dc} response of an ITO/PEDOT:PSS/EP/LiF/Ca/Al device, measured at $h\nu$ = 2.96 eV, V_{ac} = 0.5 V, and f = 1 kHz, with and without a short pass filter (SPF). The inset shows the magnified plot in the range -2.0 $\leqslant V_{dc} \leqslant$ 1.5 V.

by 6 %. Thus, although V_{null} can be measured with reasonable accuracy at signals as low as 1 μV, the optimum accuracy (< 0.3 %) is achieved for signals higher than 10 μV.

3.7 V_{null} Variation Between Different Pixels and Devices

Ideally, V_{null} ought to be the same in devices of the same type (i.e. in devices made with the same materials), and in different pixels on the same device. However, due to variation in the material quality and the presence of impurities, this is not always the case. Thus, in general, if the devices are not from the same batch (but are of the same type), an increased V_{null} variation between them can be expected. Also, if impurities (or other irregularities) are accidentally introduced into the PLED, an increased V_{null} variability between the pixels and the devices is likely.

In Table 3.1 we present the measured V_{null} values of several PLEDs, all of which were encapsulated (and expected to have low concentration of impurities). Data of four types of devices is shown, with differing anodes and/or cathodes, but with

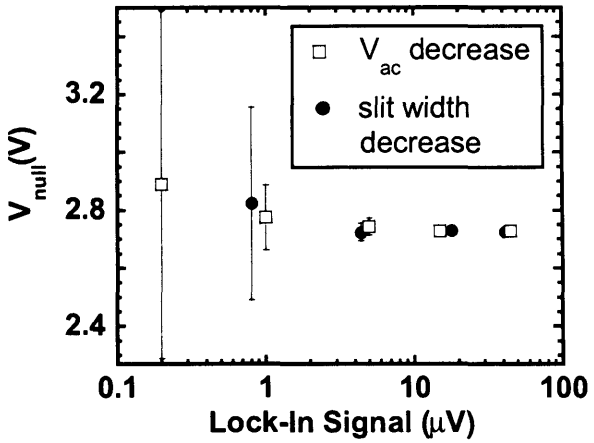

Figure 3.14: The average nulling voltage and the maximum interval of variation as a function of lock-in signal magnitude at V_{dc} = 0 V. The ITO/PEDOT:PSS/EP/LiF/Ca/A device was measured at $h\nu$ = 2.96 eV, V_{ac} = 0.5 V, and f = 1 kHz.

the same or similar active layer (a blue-emitting polyfluorene). In each device four different pixels have been measured, marked p1 to p4 in Table 3.1. As can be seen, V_{null} variation between different pixels (within the same device) ranges from a minimum of 8 mV (in device A2), to a maximum of 64 mV (in device B1). The variation of mean V_{null} between devices of the same type is larger, and can be as high as 101 mV (between devices D2 and D3), or as low as 21 mV (between devices A1 and A2). In our experience, these values are typical of other PLEDs, provided they are highly regular, i.e. made with high purity materials and under carefully controlled fabrication conditions.

3.8 Conclusion

In this chapter, we demonstrated that the measured EA response of an ITO/EP/Al device is in excellent agreement with EA equations 3.4 and 3.5. Although EA accuracy may decline at frequencies above 40 kHz, accurate V_{null} measurements are possible up to at least 100 kHz. At high frequencies an additional type of noise may be of concern, however it is easily eliminated by connecting the photodetector ground to the nearest earth. Importantly, as expected from equation 3.4, V_{null} was found to

Anode	**Cathode**	**No.**	V_{null}	V_{null}	V_{null}	V_{null}	V_{null}
			p1 (V)	p2 (V)	p3 (V)	p4 (V)	mean (V)
ITO	Al	A1	1.018	0.992	1.024	1.006	1.010
ITO	Al	A2	0.989	0.993	0.985	0.991	0.989
ITO/PDT	NiCr/Al	B1	1.326	1.380	1.378	1.390	1.368
ITO/PDT	NiCr/Al	B2	1.429	1.399	1.442	1.460	1.432
ITO/PDT	Ba/Ag	C1	2.511	2.508	2.502	2.510	2.508
ITO/PDT	Ba/Ag	C2	2.567	2.580	2.541	2.562	2.562
ITO/PDT	LiF/Ca/Al	D1	2.773	2.741	2.750	2.758	2.755
ITO/PDT	LiF/Ca/Al	D2	2.684	2.658	2.692	na	2.678
ITO/PDT	LiF/Ca/Al	D3	2.757	2.810	2.780	2.769	2.779

Table 3.1: Comparison of nulling voltage variation between different pixels (marked p1 to p4) and different devices of the same type. PDT stands for PEDOT:PSS. The experimental parameters were the same in each measurement, and the photon energy was fixed at 2.96 eV, ac voltage at 0.5 V, and frequency at 1 kHz.

be independent of both photon energy (in the measured range 2.79 to 2.99 eV), and of frequency (up to at least 100 kHz). Thus, the results are in full agreement with the theory, and demonstrate that our spectrometer can accurately measure the EA response and the built-in voltage of PLEDs. Any deviation from equations 3.4 and 3.5, if observed in future devices (under similar experimental conditions) can thus be ascribed to genuine physical effects arising within the PLED device.

We also discussed the accuracy of V_{null} measurements and found that V_{null} varies by $\pm$ 10 mV (at fixed $h\nu$, V_{ac}, ω, and for the same PLED and pixel). V_{null} variation between different PLEDs of the same type was found to be between 20 and 100 mV.

Chapter 4

Electroabsorption Measurements of ITO/PEDOT:PSS/ Polyfluorene/LiF/Ca/Al Devices

We report on electroabsorption (EA) measurements of polymer light-emitting diodes with the general structure ITO/PEDOT:PSS/emitting-polymer/LiF/Ca/Al, where ITO is indium tin oxide, PEDOT:PSS is poly(3,4-ethylene dioxythiophene) doped with poly(styrene sulfonate), and the emitting polymer is either poly(9,9-dioctylfluorene) (F8), poly(9,9-dioctyl-fluorene-co-bis-N,N'-(4-butyl-phenyl)-bis-N,N'-phenyl-1,4-phenylenediamine) (PFB), poly(9,9-dioctylfluorene-co-N-(4-butylphenyl)-diphenylamine) (TFB), or a blend of these components. Interestingly, we find that the EA nulling voltage, i.e. the dc bias at which the EA signal vanishes, depends significantly on the frequency of the ac voltage and on the incident photon wavelength. Such a dependence poses a problem for accurate measurement of the so-called built-in voltage (V_{BI}), i.e. the voltage generated between the electrodes upon equilibration of the Fermi levels through the heterostructure. We find that the EA signal is mixed with a smaller intensity signal which can be ascribed to excited state absorption, and we propose a method for separating the excited state absorption signal. Importantly, for photon energies close to the peak of the Stark response, and at higher ac frequencies (e.g. at 50 kHz), the variation of the nulling voltage with energy is significantly lower, which allows an estimate of the built-in voltage. We discuss the origin of the

excited state absorption signal and present evidence suggesting that it is likely to be due to trapped electrons near PEDOT:PSS/polyfluorene interface.

4.1 Introduction

Since the initial work on polymer light-emitting diodes (PLEDs) by Burroughes and co-workers[9] there has been substantial progress in understanding the physics of such devices, and in the technology necessary to control their performance. However, limited polymer stability and susceptibility to degradation during operation have been until recently major obstacles to obtaining commercially viable polymer-based emissive displays. Whereas the lifetime of the best red- and green-emitting diodes is now sufficient for commercial applications (>10,000 hours) the lifetime of the blue-emitting diodes is significantly shorter[17]. Thus, increasing the lifetime of the blue diodes is at present among the most prominent targets for the development of full colour displays.

Polyfluorene (PF)-based materials have emerged as the most promising candidates as blue-emitting materials, owing to their excellent stability and efficient electroluminescence (EL). Lifetimes exceeding 4000 hours have also been reported[17]. Due to their typically low electron affinity blue-emitting polymers often require the use of interlayers such as LiF at the polymer-cathode interface[97]. These are known to reduce the electron injection barrier[98,99] and improve the device luminescence efficiency and lifetime. At the anode, the hole transport interlayer, poly(3,4-ethylene dioxythiophene) doped with poly(styrene sulfonate) (PEDOT:PSS), is often used to aid the injection of holes into the polymer[75,124,125]. Although the presence of LiF and PEDOT:PSS may reduce the interaction of the polymer with the cathode[126] (often a reactive metal such as Ca), and the indium tin oxide (ITO) anode[127], known to cause EL degradation, it is not as yet clear whether LiF and PEDOT:PSS themselves may be involved in device degradation[128]. The evidence published in the literature so far suggests that PEDOT:PSS is likely to be damaged upon electrical driving[129,130] which may cause some parts of the layer to react with the emitting polymer and degrade it[131,132].

Electroabsorption (EA) has been shown to be an effective tool for studying such systems[72]. It has been used to gain information ranging from interface dipoles[73,101], barriers for charge injection[75] and energy level alignment[100] to degradation of the polymer layer[112,113]. Here, electroabsorption is used in the study of diodes with the general structure ITO/PEDOT:PSS/PF-based polymer/LiF/Ca/Al. The polymers investigated include poly(9,9-dioctylfluorene) (F8), poly(9,9-dioctyl-fluorene-co-bis-N,N'-(4-butyl-phenyl)-bis-N,N'-phenyl-1,4-phenylenediamine) (PFB), poly(9,9-dioctylfluorene-co-N-(4-butylphenyl)-diphenylamine) (TFB), and a 60-20-20 % (ratio by weight, respectively) tri-blend of these polymers.

When the device is first formed, the equilibration of the Fermi energy through the whole structure occurs via electron transfer from the electrode with the lower work function (LiF/Ca/Al) to the electrode with the higher work function (ITO/PEDOT:PSS). Such a charge distribution generates a potential difference between anode and cathode (the so-called built-in voltage, or V_{BI}) that supports an electric field in the active polymer layer. Interestingly, such electric field changes the polymer optical properties via the Stark effect. The internal fields can then be probed, non-invasively, by means of optical experiments, such as the measurements of the Stark response. Typically, significant insight into the magnitude of the built-in fields can be gathered by measurements of the fractional change in absorption or transmission ($\Delta T/T$), the electroabsorption response, as a function of additional, externally applied fields/voltages. In the Stark effect, $\Delta T/T$ is proportional to the square of the electric field[72], so that for an applied bias of the form $V = V_{dc} + V_{ac}\sin(\omega t)$, and in a polymer layer free of space charge, the modulation of the differential transmission at both the first- and second-harmonic frequencies is in accordance with equations

$$\Delta T/T(1\omega) \propto 2Im\{\chi^3(h\nu)\}V_{ac}(V_{dc} - V_{BI})\sin(\omega t + \theta), \tag{4.1}$$

$$\Delta T/T(2\omega) \propto \frac{1}{2}Im\{\chi^3(h\nu)\}V_{ac}^2\cos(2\omega t + 2\theta), \tag{4.2}$$

where $Im\{\chi^3(h\nu)\}$ is a function of the imaginary part of the third order dielectric

susceptibility, h is Planck's constant, ν is the photon frequency, and θ is the phase of the signal with respect to the applied ac voltage. Thus, $\Delta T/T(1\omega)$, the first harmonic of $\Delta T/T$, varies linearly with V_{dc} and, for an electromodulated (EM) signal arising only from Stark effect, passes through zero at $V_{dc} = V_{BI}$, whereas $\Delta T/T(2\omega)$, i.e. the second harmonic of $\Delta T/T$, is independent of V_{dc}. The built-in voltage is usually best measured at photon energies ($h\nu$) in the vicinity of the lowest energy Stark peak, where the Stark signal is high and linear absorption is relatively low[55]. This minimises any effects that might arise from photogenerated charges, and keeps the signal/noise ratio close to its maximum.

Interestingly, we find that the electromodulated signal contains additional contributions whose dependence on frequency and dc bias is not in agreement with equation 4.1. Observations of such additional contributions have also been published by Lane *et al.*[102], who ascribed them to excited state absorption (ESA). The signal is likely to be a result of the modulation of trapped charge density near one of the electrodes, induced by an applied sinusoidal electric field[133]. In our case, we observe in particular a significant dependence of the $\Delta T/T(1\omega)$ nulling voltage, V_{null} (i.e. the dc bias at which $\Delta T/T(1\omega)$ is nulled), on the incident photon energy $h\nu$ and on the ac bias frequency $\omega/2\pi$, which makes the measurement of the built-in voltage not straightforward. We attribute such behaviour to the intermixing of Stark and ESA signals in agreement with Lane *et al.*[102], but also notice that an additional factor might be the non-uniformity of the electric field inside the active layer, having ruled out noise and photoluminescence (filtered out, where necessary) as possible explanations.

4.2 Experimental

The PLEDs used in the experiments for this chapter were provided by CDT. They were fabricated on oxygen-plasma treated ITO substrates covered by a 70 nm thick PEDOT:PSS layer[134]. The PEDOT:PSS was spin-coated and baked at 200 ^{o}C for 60 minutes. The substrates were then transferred to a nitrogen glovebox for all subsequent processing steps. The emitting polymer was spin coated onto the

substrate from a 2 % (weight) xylene solution. The cathodes were evaporated at pressures 10^{-6}-10^{-7} mbar and the thickness was measured with a calibrated quartz crystal monitor, so as to give the following thicknesses: LiF (4 nm), Ca (10 nm), Al (400 nm). The active area of the pixels was 10 mm^2. The emitting polymer layer and the cathodes were processed in a nitrogen glove box and the finished devices were encapsulated with metal cans and epoxy resin. Contact pins were attached to allow characterisation outside the glovebox. Following fabrication, the devices were electrically driven for a couple of minutes (for efficiency, luminance and current tests) before their EA response was measured.

4.3 TFB, PFB, F8 and Tri-Blend Results

In our measurements, we found that the main experimental results, such as the mixing of Stark and ESA signals, and V_{null} dependence on photon energy, are very similar in TFB, PFB, F8 and tri-blend devices. Thus, in this section, we present the results for the TFB-based device, which are typical of F8-, PFB-, and tri-blend -based devices as well.

4.3.1 Electromodulation (EM) Spectra

Figure 4.1 shows the first and second harmonic electromodulation (EM) spectra of the TFB-based device at V_{ac} = 1.0 V, frequency f = 2 kHz, and V_{dc} = 0 or - 4 V (reverse bias). The spectra are dominated by two large peaks centred at 2.98 and 3.55 eV, and there is a much smaller, broader peak shown magnified in the inset, centred in the vicinity of 2.3 eV. When the dc bias is changed from 0 to - 4 V, the first harmonic signal $\Delta T/T(1\omega)$ increases by more than a factor of 2 in the range 2.9 to 3.8 eV (region A), whereas it decreases for energies between 2.0 and 2.7 eV (region B). The second harmonic response, $\Delta T/T(2\omega)$, at 0 and -4 V, multiplied by a factor of 12.7, is nearly identical to the first harmonic signal at 0 V in region A, and does not change when the bias is changed from 0 to -4 V, as expected according to equation 4.2. In region B, the second harmonic response is too small to generate a signal distinct from the background noise.

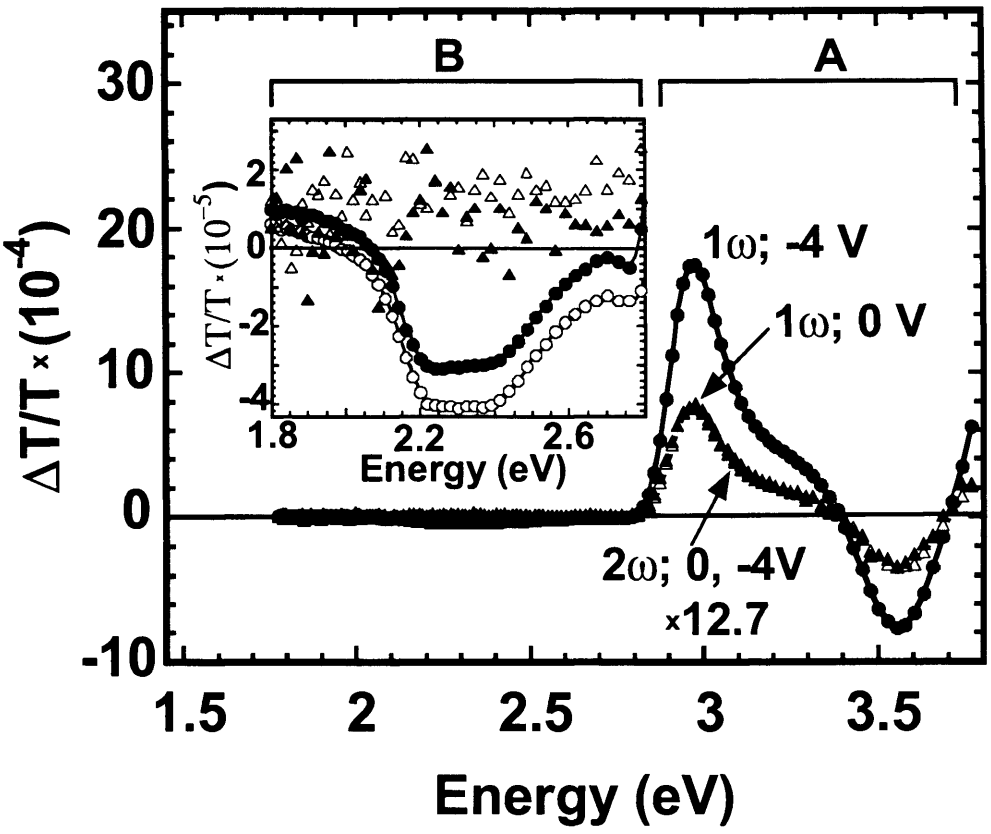

Figure 4.1: First harmonic, 1ω (circles), and second harmonic, 2ω (triangles), EM spectra (note the 12.7 factor for the second harmonic spectra), of an ITO/PEDOT:PSS/TFB/LiF/Ca/Al LED. The applied dc bias was 0 V (empty symbols) and - 4 V reverse bias (filled symbols). The ac voltage amplitude is 1.0 V and frequency equals 2 kHz. The second harmonic response is independent of dc bias and is nearly identical to the first harmonic response at $V_{dc} = 0$ V, as expected from equations 4.1 and 4.2. The inset shows magnified spectra in the energy range 1.8 to 2.8 eV.

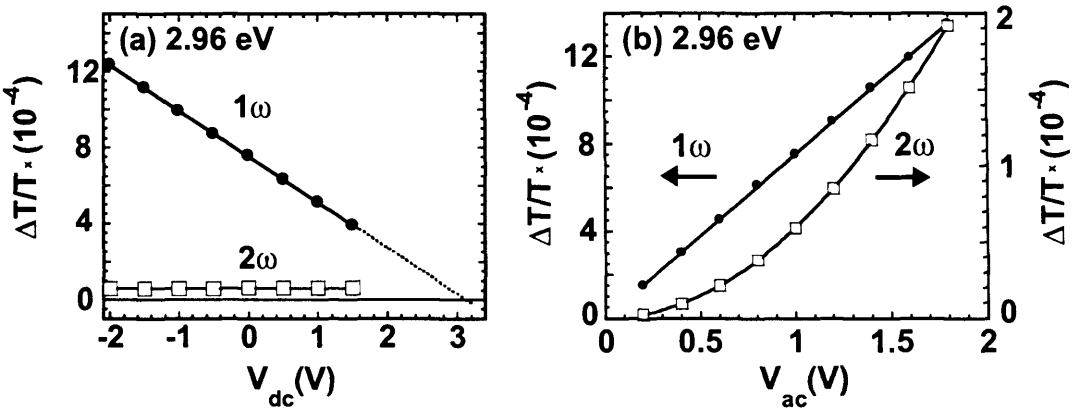

Figure 4.2: (a) dc bias, and (b) ac bias dependence of the PLED's electromodulation response. The dc bias dependence was measured for V_{ac} = 1 V and the ac bias dependence was measured for V_{dc} = 0 V. All signals were measured at 2.96 eV incident photon energy and at 2 kHz frequency. Consistently with equations 4.1 and 4.2 we observe a linear dependence on V_{dc} of the first harmonic (1ω) signal, and no dependence on V_{dc} of the second harmonic (2ω) signal. Similarly, the 1ω and 2ω vs ac bias curves can be fitted with a generic power law (V_{ac}^n) with n = 1.0008 and n = 1.9952.

4.3.2 Electromodulation Signal versus V_{dc} and V_{ac}

The applied voltage dependence of the EM signals in regions A and B of the spectrum is shown in Figures 4.2 and 4.3 respectively. More precisely, Figure 4.2(a) shows the first and second harmonic EM response as a function of the applied dc bias, measured at 2.96 eV incident photon energy (region A), V_{ac} = 1.0 V, and f = 2 kHz. The first harmonic signal, shown in the range -2.0 < V_{dc} < 1.5 V, is linearly dependent on V_{dc} in accordance with equation 4.1. Since the signal becomes non-linear with V_{dc} (for V_{dc} > 1.8 V) as a result of charge injection into the emitting-polymer layer, the signal for higher dc biases is not shown here. The dotted line corresponds to the extrapolated 1ω response for V_{dc} > 1.5 V, and crosses the V_{dc} axis at V_{null} = 3.14 V. The 2ω signal remains constant over the V_{dc} range shown, as expected from equation 4.2. The dependence of the first and second harmonic signals on V_{ac}, measured at $h\nu$ = 2.96 eV, V_{dc} = 0 V and f = 2 kHz, in the range 0.2 < V_{ac} < 1.8 V, is shown in Figure 4.2(b). The curves were fitted with a generic power law (V_{ac}^n) yielding n = 1.0008 and n = 1.9952 for the first and second harmonic signals respectively, consistent with equations 4.1 and 4.2.

Figures 4.3 (a) and (b) show the first harmonic $\Delta T/T$ as a function of V_{dc} and V_{ac}

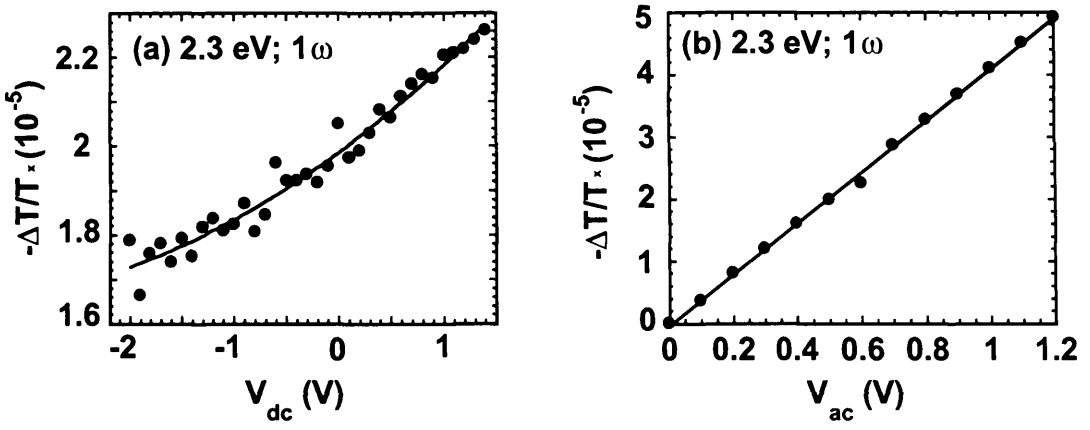

Figure 4.3: First harmonic EM response (ΔT/T(1ω)) as a function of V_{dc} for V_{ac} = 0.5 V (a), and as a function of V_{ac} for V_{dc} = 0 V (b), at 2.30 eV incident photon energy and a frequency of 2 kHz. The V_{dc} dependence is fitted with a second order polynomial, whilst the V_{ac} dependence is fitted with a straight line fit.

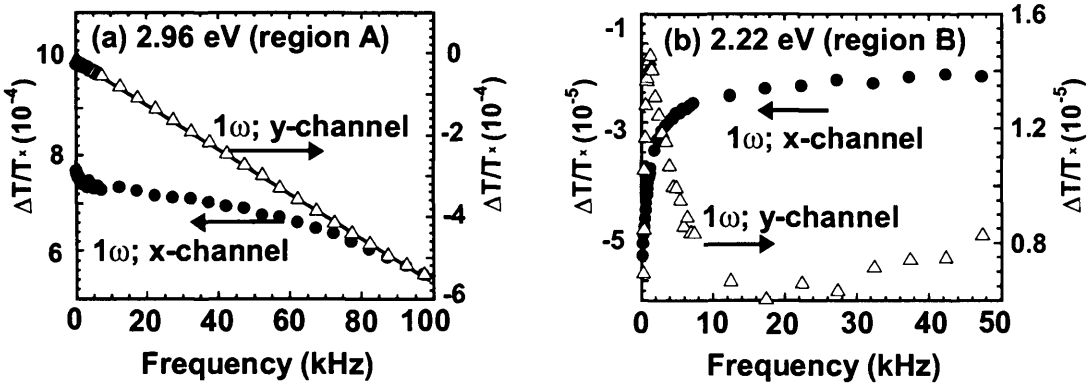

Figure 4.4: $\Delta T/T$ vs frequency graphs at 2.96 eV and 2.22 eV incident photon energy, V_{ac} = 1 V, V_{dc} = 0 V.

respectively, at 2.30 eV incident photon energy (region B). In the measured range, the signal fits a linear dependence on V_{ac} very well, but the V_{dc} dependence is clearly non-linear, and fits a polynomial of the second order. In addition, the absolute magnitude of the signal decreases as the diode is more negatively biased, i.e. as the field in the bulk of the emitting-polymer layer is increased. Such dependence is at variance with equation 4.1, from which we would expect a signal increase for higher electric fields.

4.3.3 Electromodulation Signal versus Frequency

The dependence of the EM signal on the ac bias frequency is shown in Figure 4.4 for photon energies 2.96 eV (region A) and 2.22 eV (region B), at 1 V ac bias amplitude, with no externally applied dc bias. The left-hand ordinates axis shows the lock-in amplifier x-channel (in-phase) signal, whilst the y-channel (out-of-phase) signal is shown on the right-hand ordinates axis.

At **2.96 eV**, the x-channel component is approximately linear with f^2 above 5 kHz, and for frequencies in the range 20 to 100 kHz obeyed the following fit (fitted using the Kaleidagraph least squares curve fit)

$$\Delta T/T(1\omega, x) = 7.15 \times 10^{-4} - 1.88 \times 10^{-14} \times f^2, \tag{4.3}$$

and the correlation coefficient R[135], an indicator of the quality of the fit (1 indicating the perfect fit), equal to 0.9987. Interestingly, below $\sim$ 5 kHz the signal deviates distinctly from this dependence. The y-channel component is linear in the range above 5 kHz and can be fitted to a straight line, according to the following fit equation

$$\Delta T/T(1\omega, y) = -1.47 \times 10^{-6} - 5.47 \times 10^{-9} \times f, \tag{4.4}$$

with R = 0.99985, again indicating a very close fit. Below $\sim$ 5 kHz the dependence is clearly non-linear.

At **2.22 eV**, on the contrary, plots of the x-channel signal versus f^2, and of y-channel signal versus f, in the range 20 to 100 kHz, do not have a clear linear dependence. The x-channel signal is negative and its absolute magnitude progressively decreases as the frequency is increased. Also, the y-channel signal is positive and initially increases as f is increased from 0.2 kHz, reaches a maximum at 1.2 kHz, then starts to decrease reaching a minimum at 17 kHz, and then increases with frequency up to 100 kHz.

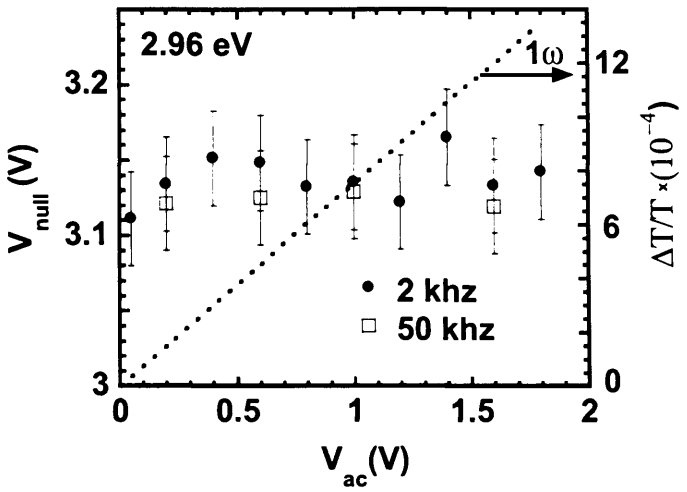

Figure 4.5: V_{null} as a function of ac bias (left hand y-axis) at 2 and 50 Khz. The maximum interval of variation is indicated by the error bars. The $\Delta T/T(1\omega)$ signal at $V_{dc} = 0$ V, f = 2 kHz, is indicated on the right hand y-axis. The graph shows that within the measured range 0.05 V $< V_{ac} <$ 1.8 V V_{null} is independent of ac bias.

4.3.4 V_{null} as a Function of V_{ac}, $h\nu$ and Frequency

Figure 4.5 shows the dependence of V_{null} on the ac bias measured at $h\nu = 2.96$ eV, $f = 2$ kHz and $f = 50$ kHz. The right-hand y axis shows the $\Delta T/T(1\omega)$ signal measured at $V_{dc} = 0$ V and $f = 2$ kHz, which varies linearly from 3.6×10^{-5} at $V_{ac} =$ 0.05 V to 1.3×10^{-4} at $V_{ac} = 1.8$ V. The graph shows that V_{null} does not depend on ac bias amplitude within the experimental error, at either lower (2 kHz), or higher (50 kHz) frequencies.

In Figure 4.6(a) we present the results of V_{null} measurements as a function of energy of the probing beam in the range $2.76 < h\nu < 3.1$ eV, at 2 and at 50 kHz. The right-hand y-axis shows the $\Delta T/T(1\omega)$ signal measured at $V_{dc} = 0$ V and $f =$ 2 kHz. V_{null} measurements were performed as described in Chapter 3, and the ac bias amplitude was fixed at 1.0 V. As can be seen, the variation of V_{null} with energy is large at energies around 2.8 eV, where $\Delta T/T$ is small, and smaller at energies in the vicinity of the $\Delta T/T$ peak (~3 eV). Interestingly, the energy dependence of V_{null} is much smaller at 50 kHz than at 2 kHz, with V_{null} seemingly approaching a similar value at the two frequencies (~3.1 and ~3.2 V respectively) as $\Delta T/T(1\omega)$ reaches values larger than $\sim6\times10^{-4}$. At 2 kHz, V_{null} varies from 3.03 V at 2.89 eV, to 3.21 V at 2.96 eV, whereas at 50 kHz, in the same $h\nu$ span, V_{null} increases from

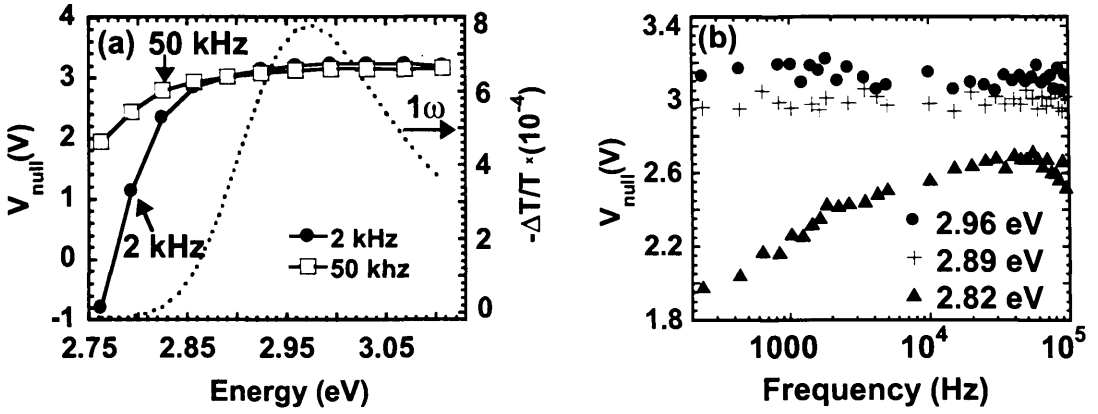

Figure 4.6: (a) V_{null} as a function of incident photon energy at 2 and 50 khz, together with the first harmonic response (dotted line); (b) V_{null} as a function of frequency at $h\nu$ = (2.82, 2.89, 2.96 eV).

3.02 to 3.13 V.

The frequency dependence of V_{null} is shown in Figure 4.6(b), in the range 0.23 - 50 kHz, and for three different values of $h\nu$ (2.82, 2.89 and 2.96 eV). The plot is consistent with the results of Figure 4.6(a), with an observed large variation of V_{null} with frequency at 2.82 eV, and smaller variation at 2.89 and 2.96 eV. At 2.89 eV, V_{null} lies within the range $2.88 < V_{null} < 3.06$ V, with a mean value of 2.99 V and standard deviation equal to 0.04 V. By comparison, at 2.96 eV, where $\Delta T/T$ is 1.6 times larger, V_{null} lies within the range $3.05 < V_{null} < 3.22$ V, and has a mean value of 3.12 V and standard deviation equal to 0.05 V.

4.4 Discussion

4.4.1 Electromodulation Response versus $h\nu$, V_{dc}, V_{ac}

Region A ($2.9 < h\nu < 3.8$ eV)

The EM response in region A is in accordance with the EA equations 4.1 and 4.2, with the first harmonic signal proportional to V_{dc} and V_{ac}, the signal being higher at larger dc fields, and the second harmonic signal constant as a function of V_{dc}, and proportional to V_{ac}^2. Once suitably scaled, the second harmonic spectrum is essentially identical to the first harmonic, as expected from equations 4.1 and 4.2,

and the common dependence on $\chi(\nu)$. Region A spectra are also in agreement with previously published electroabsorption spectra of blue-emitting polyfluorene-based polymers[100,122]. We therefore consider that the electromodulated signal in region A is dominated by the Stark response of the active polymer layer.

Region B ($2.0 < h\nu < 2.7$ eV)

The EM response in region B decreases when the bias is changed from 0 to -4 V. This behaviour is opposite to that observed in region A (2.9 to 3.8 eV). Although the signal is linearly dependent on V_{ac} (Figure 4.3), it also exhibits a non-linear dependence on the dc bias, which is not consistent with Stark response of the polymer layer. Furthermore, the broad peak ($\sim$ 2.3 eV) occurs below the TFB absorption onset, and the EM response does not match any corresponding electroabsorption data in the literature. The EM response is however similar to the EM response observed by Lane and co-workers in ITO/PEDOT:PSS/PFO:F8BT/Ca/Al light-emitting diodes, where PFO is poly(9,9'-dialkyl-fluorene-2,7-diyl), and F8BT is poly(9,9-dioctylfluorene-alt-benzothiadiazole)[102]. The EM response that they observed was ascribed to excited state absorption (ESA) by trapped charge, which according to the authors follows a dynamics similar to those of photoexcited charges, with lifetimes of micro- to milli-seconds.

4.4.2 Electromodulation as a Function of Frequency

Region A

To discuss the frequency dependence of the first harmonic signal in region A, we start by considering x- and y-component behaviour expected from equation 4.1. First, we express θ (the phase difference between the applied ac voltage and the Stark-effect EM signal) as a function of ω. For a PLED device modelled as a resistor R_1 and a capacitor C_1 connected in parallel, representing the active layer, together with a resistor R_2 connected in series (Figure 4.7), we have

$$\tan\theta = -\omega(CR_1R_2)/(R_1 + R_2) = -\tau_c\omega, \tag{4.5}$$

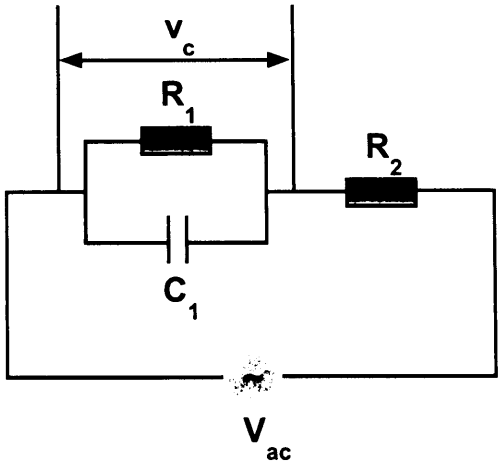

Figure 4.7: A model circuit of a polymer light-emitting diode. V_C is the voltage across the active layer.

where $\tau_c = (CR_1R_2)/(R_1+R_2)$. θ is also the phase between the applied voltage and the voltage across the active layer. Now, in the limit for small θ, we have $\theta \approx -\tau_c\omega$, and, by expanding $\sin(\omega t+\theta)$, we can write equation 4.1 as

$$\Delta T/T(1\omega) = k_1[\sin(\omega t)(1-\frac{1}{2}(\tau_c\omega)^2) - \cos(\omega t)\tau_c\omega], \tag{4.6}$$

where $k_1(h\nu, V_{dc}, V_{ac}) \propto \chi(h\nu)V_{ac}(V_{dc}-V_{BI})$. The lock-in x- and y-channel components, for small θ, can therefore be written as

$$\Delta T/T(1\omega)_x = k_1(1-\frac{1}{2}(\tau_c\omega)^2) \tag{4.7}$$

$$\Delta T/T(1\omega)_y = -k_1\tau_c\omega. \tag{4.8}$$

We can now compare equations 4.7 and 4.8 with the observed experimental dependence of the $\Delta T/T$ x and y signals on frequency (equations 4.3 and 4.4 respectively). Equation 4.3 is of the same form as equation 4.7, and equating the terms with the same power of ω yields $k_1 = 7.15\times10^{-4}$, and $\tau_c = 1.2\times10^{-6}$ s. (These coefficients are valid at $h\nu = 2.96$ eV, $V_{dc} = 0$ V, and $V_{ac} = 1$ V.) Equation 4.4 is of the same form as equation 4.8, apart from a constant term of the order of 10^{-6}, which may be due to noise. We can now check the validity of our approximation based on these

values, and we note that although at the upper frequency band (100 kHz) $\theta = 0.754$, giving an error of approximately 20 %, up to $f = 50$ kHz the error $(\tan\theta - \theta)/\tan\theta$ is less than 5 %. The approximation used appears thus reasonable, especially for $f < 50$ kHz. In the range of frequency below 5 kHz (at 2.96 eV probing energy), the dependence of the EM signal on frequency is not in agreement with equations 4.7 and 4.8.

We consider that the signal at 2.96 eV consists of the Stark signal mixed with an ESA signal of a much smaller magnitude. To obtain the approximate ESA signal as a function of frequency, we subtract from the total signal (Figure 4.4a) the Stark-effect signal described by equations 4.3 and 4.4. In Figure 4.8, we compare the ESA signal at 2.96 eV obtained with this subtraction (data multiplied by -1 and shown in empty symbols, squares show the x-channel and triangles show the y-channel), with the frequency dependence of the ESA signal measured at 2.22 eV (shown earlier in Figure 4.4b) (full symbols), in the range 0.2 to 7 kHz. Remarkably, the frequency dependence of the two signals is very similar, indicating that the ESA signal, dominant at 2.22 eV (region B), is also present at 2.96 eV. At 2.96 eV, the magnitude of the in-phase Stark-effect signal is approximately 15 (low f) to 50 (high f) times larger than the magnitude of the in-phase ESA signal. The Stark response (of the bulk of the active polymer layer) is thus dominant at 2.96 eV.

Region B

It is interesting to compare the frequency dependence of the signal in region B, with the relation given for an ESA signal by Lane *et al.*[102], and Brewer *et al.*[103],

$$\Delta T/T(\omega)_x = c_1/(1+\omega^2\tau^2), \tag{4.9}$$

$$\Delta T/T(\omega)_y = -c_1(\omega\tau)/(1+\omega^2\tau^2), \tag{4.10}$$

where ω is the modulation frequency, τ is the excitation lifetime, and c_1 is a constant of proportionality[136]. (Again, the subscript x refers to the lock-in x-channel,

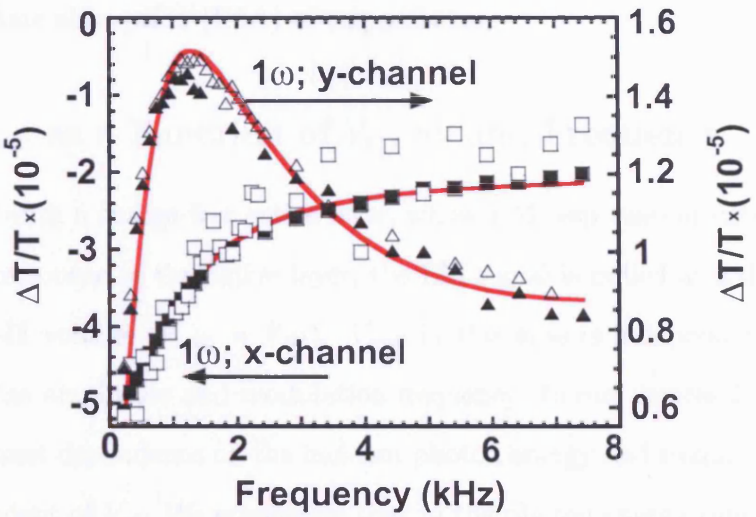

Figure 4.8: A comparison of the $\Delta T/T(1\omega)$ vs frequency plots of the ESA signal at 2.96 eV (obtained by subtracting the Stark response from the total $\Delta T/T(1\omega)$ signal) multiplied by -1, shown in empty symbols, and the $\Delta T/T(1\omega)$ signal measured at 2.22 eV, shown in full symbols. Squares are for x-channel whereas triangles are for y-channel signals. The full line is a fit to the 2.22 eV plot. Closeness of the fit suggests that $\Delta T/T(1\omega)$ at 2.22 eV is dominated by ESA.

and y to the lock-in y-channel.) The dependence of the EM response at 2.22 eV on frequency, shown in Figure 4.8 (full symbols), has some similarities with the dependence expected from ESA equations 4.9 and 4.10. The $\Delta T/T_x$ signal is inversely proportional to the frequency, whereas $\Delta T/T_y$ increases initially as the frequency is increased from 0.2 kHz, reaches a maximum at $\sim$ 1.2 kHz, and then decreases with increasing f. For a quantitative assessment, we found that we could fit $\Delta T/T_x$ and $\Delta T/T_y$ signals individually to equations 4.9 and 4.10 respectively. However, c_1 and τ in the two fits were significantly different. We therefore considered that the EM signal at 2.22 eV may be a sum of the ESA signal and another signal of the form c_1'$\sin(\omega t + \theta)$ (such a signal may arise for example due to the Stark response of the sub-gap absorption). Interestingly, this gave a good fit to the experimental data. The full red line in Figure 4.8 shows the fit (given by equations A2.7 and A2.8 in appendix A2) to the $\Delta T/T$ vs frequency data at 2.22 eV. The fit is very close to the experimentally observed dependence, with the fitted excitation lifetime τ equal to 130 μs. This is of the same order of magnitude as the value measured by Lane *et al.*[102], thus supporting the hypothesis that the EM signal in region B is dominated

by excited state absorption (ESA) of trapped charge.

4.4.3 V_{null} as a Function of V_{ac}, $h\nu$ and Frequency

For a PLED with a charge-free active layer, whose EM response consists only of the Stark-effect response of the active layer, the EM signal is nulled at a dc bias equal to the built-in voltage ($V_{null} = V_{BI}$). V_{null} in this case is independent of photon energy, ac bias amplitude and modulation frequency. In our devices however, V_{null} has a significant dependence on the incident photon energy and frequency, although it is independent of V_{ac}. We emphasize that in the photon energy range of concern here (2.8 - 3 eV), the photoluminescence signal was kept sufficiently small (using a short pass filter, where necessary), and did not affect V_{null} measurements.

From analysis of V_{null} vs $\Delta T/T$ (Figure 4.5), we find that the measured V_{null} values are accurate to within $\pm$ 0.1 V at signal strengths of 1×10^{-5}, and to within less than $\pm$ 0.05 V at signal strengths of 1×10^{-4}. Figure 4.5, for example, shows no significant variation in V_{null} for $\Delta T/T$ values in the range 3×10^{-5} to 1×10^{-3}. We can thus exclude the possibility that the increase of V_{null} shown in Figure 4.6(a), from -0.8 V at 2.76 eV (2 kHz) to 3.2 V at 2.96 eV (2 kHz), is due to an increase of the signal-to-noise ratio. Instead, based on the results above, we consider that the variation of V_{null} with $h\nu$ and ω is caused, in part at least, by the presence of the ESA signal, which is mixed with the Stark signal. From the latter, we expect a greater V_{null} variation at energies where the Stark response is smaller, and at frequencies where the ESA is larger. Since the Stark-effect response is smaller for smaller probing energies (below $\sim$3 eV) , and the in-phase ESA response is inversely proportional to frequency, this is in qualitative agreement with Figure 4.6, where the largest variation of V_{null} occurs at energies lower than $\sim$2.85 eV, and frequencies lower than $\sim$5 kHz.

To discuss how the ESA signal may cause the variation of V_{null} with $h\nu$ and ω, we consider the relative contributions of the Stark response (of the bulk of the active layer) and ESA signals to the total EM signal, as shown in Figure 4.9. By rewriting equation 4.1, the Stark-response can be represented by the linear rela-

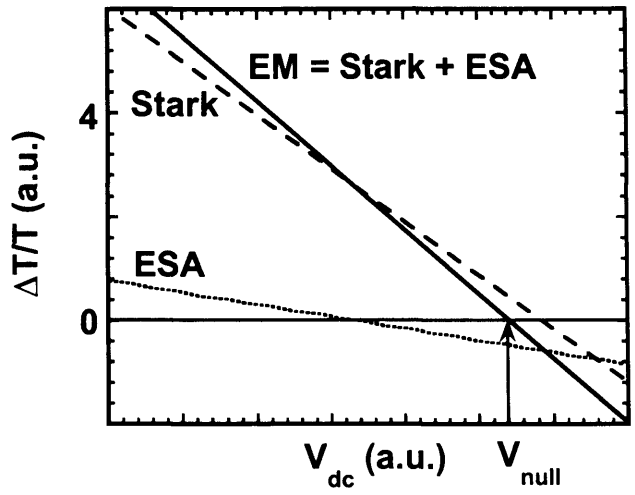

Figure 4.9: A schematic $\Delta T/T$ vs V_{dc} plot of an EM signal which is a sum of Stark and ESA signals.

tion $(a_s(h\nu)V_{dc} + b_s(h\nu))$, where the coefficients $a_s(h\nu)$ and $b_s(h\nu)$ are respectively the gradient and the value of the signal at zero bias, and are both proportional to $Im\{\chi^3(h\nu)\}$. Note that, in the absence of significant concentration of space charge in the active layer, the ratio $-b_s(h\nu)/a_s(h\nu)$ is equal to the built-in voltage. Now, although the dependence of the ESA signal on V_{dc} deviates from linearity, for a qualitative assessment (to a first approximation) we represent it by a linear relation as well, not least because the nulling voltage can always be determined by measurements at only two V_{dc} values. Correspondingly to the Stark relation, the ESA signal, which depends on ω as well as $h\nu$, is thus represented as $(a_{esa}(h\nu,\omega)V_{dc} + b_{esa}(h\nu,\omega))$. The EM signal then, being a sum of EA and ESA, is represented as $(a_s(h\nu)+a_{esa}(h\nu,\omega))V_{dc}+(b_s(h\nu)+b_{esa}(h\nu,\omega))$, and V_{null} is therefore given by:

$$V_{null}(h\nu,\omega) = -(b_s(h\nu) + b_{esa}(h\nu,\omega))/(a_s(h\nu) + a_{esa}(h\nu,\omega)). \tag{4.11}$$

It is clear from this that V_{null} may be dependent on both $h\nu$ and ω, and that, in general, the dependence is less pronounced if the Stark response is much higher than ESA. In addition, if the trapped charge (that causes the ESA signal) is indeed present in the active layer (whose spatial distribution is unknown, although it has been suggested that it may be situated within few Å of the PEDOT:PSS/polyfluorene

interface[102]), the Stark response of the active layer may then be non-uniform, since the trapped charge may cause a spatially non-uniform electric field, and a spatially non-uniform electroabsorption spectrum, since it is well known that charged chains have different absorption spectrum[103,122,136]. In this case, using similar reasoning as above, V_{null} variation with $h\nu$ may be additionally affected by the non-uniformity of the Stark response within the active layer.

4.4.4 Estimating the Built-In Voltage

One of the strengths of EA measurements is the ability to measure the built-in voltage of finished PLEDs, and use the results to probe the energy level alignment across the PLED heterostructure. Although in some cases the nulling voltage varies significantly with photon energy, more than 1 V in Figure 4.6(a), the variation decreases significantly above 2.85 eV (up to 3.1 eV), where there is a significant Stark signal generated by the polymer layer, as can be seen in Figure 4.10 (which shows V_{null} as a function of energy in the range from 2.85 to 3.11 eV). From 2.85 to 2.98 eV, the Stark signal increases sevenfold, from 1.14×10^{-4} to 7.77×10^{-4}, and V_{null} increases by 0.2 V, from 2.93 to 3.13 V. Above 2.98 eV and up to 3.1 eV V_{null} is essentially constant at 3.14 $\pm$ 0.01 V, whereas the Stark signal decreases by half.

The decreased V_{null} variation with energy is to be expected as $\Delta T/T(1\omega)$ becomes dominated by the Stark response of the bulk of the polymer film. It is interesting to compare the experimentally measured coefficients of Stark and ESA signals in this region. For example, at $h\nu$ = 2.96 eV and f = 50 kHz, we measured $\Delta T/T(1\omega)$ to be 7.01×10^{-4} (at V_{dc} = 0 V) and 11.50×10^{-4} (at V_{dc} = -2 V), so that, assuming that the signal is dominated by the Stark effect, we have $b_s \approx 7.01 \times 10^{-4}$ and $a_s \approx -2.25\times10^{-4}$. In this region, after ESA was separated from the total $\Delta T/T(1\omega)$ signal (using the method discussed in section 4.4.2), we also estimate that $b_{esa} \approx 1.2 \times 10^{-5}$ and $a_{esa} \approx -4.5 \times 10^{-6}$. Therefore, in equation 4.11, near $h\nu$ = 2.96 eV and f = 50 kHz, the ESA signal contributes less than 2 % to the total value of the numerator, and approximately 2 % to the total value of the denominator. The two contributions actually nearly cancel each other out, since the ESA signal increases

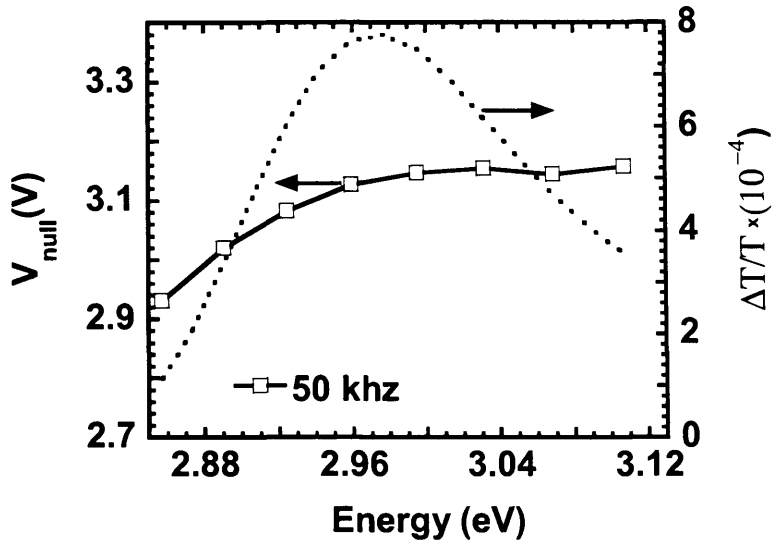

Figure 4.10: V_{null} as a function of incident photon energy of the ITO/PEDOT:PSS/TFB/LiF/Ca/Al structure, in the range from 2.85 to 3.11 eV, measured at 50 khz, together with the first harmonic $\Delta T/T$ response.

the absolute magnitude of both the numerator and the denominator. This means that, near $h\nu = 2.96$ eV and $f = 50$ kHz, V_{null} is expected to be approximately equal to V_{BI}. We estimate that V_{BI} equals 3.1 V, with the upper uncertainty limit of 0.05 V, and the lower uncertainty limit of 0.1 V.

4.5 PLEDs Based on Single Component Blends (SCBs)

We also present the results of EA measurements of PLEDs based on single component blends (SCBs) (also provided to us by CDT), in which all three components (F8, TFB and PFB) are incorporated into a single chain, and in some SCBs other monomers (not disclosed) may also be attached to the chain. LEDs based on these polymers have significantly better lifetimes (more than three orders of magnitude longer) than those based on tri-blends. Apart from the active layer, the PLEDs for which we present the results here are made from the same materials as those discussed in the preceding section (i.e. ITO/PEDOT:PSS is the anode, and LiF/Ca/Al is the cathode). The $\Delta T/T$ response of these devices, as far we can tell, is very similar to that presented in the previous section, except that the low-energy

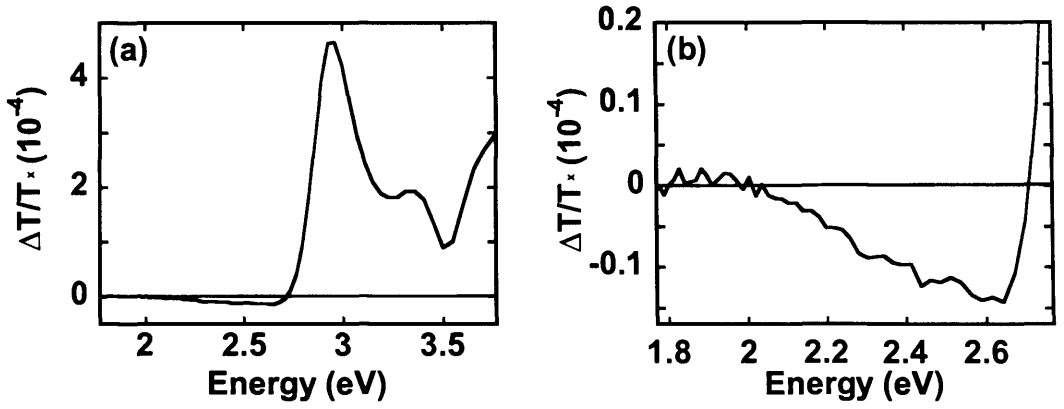

Figure 4.11: (a) First harmonic $\Delta T/T$ spectrum of an ITO/PEDOT:PSS/SCB/LiF/Ca/Al LED, measured at $V_{dc} = 0$ V, $V_{ac} = 1$ V, and f = 0.5 kHz. (Since here we are not greatly concerned with the accuracy of the spectrum above $\sim$ 2.7 eV, no effort was made to screen the PL signal.) (b) Magnified spectrum in the energy range 1.77 to 2.77 eV (no PL signal is generated in this region).

(sub-bandgap) spectrum is visibly different in magnitude and peak position.

Figure 4.11 shows the measured $\Delta T/T(1\omega)$ vs energy dependence, with the panel on the right-hand side showing the magnified spectrum in the range from 1.77 to 2.77 eV. As can be seen, there is again a notable $\Delta T/T(1\omega)$ signal in this range, which rises from zero at 2 eV, to 1.3×10^{-5} close to 2.6 eV. We note that the profile of the low energy signal differs somewhat from that shown in Figure 4.1, where the signal has a broad peak centred at 2.3 eV. In Figure 4.11, $\Delta T/T(1\omega)$ signal peaks close to 2.65 eV, where there is a sharp onset of the Stark response of the polymer layer, and the signal raises sharply as the energy is increased further.

To test if the low energy signal obeys the frequency dependence expected for an ESA signal, we measured the $\Delta T/T(1\omega)$ in-phase signal as a function of frequency at 2.49 eV, and obtained a fit to the data (as in section 4.4.2, using equation A2.7 in appendix A2). The results are presented in Figure 4.12(a), where the experimental data is shown in filled circles, and the fit is shown in diamonds connected by a full line. As can be seen, the fit is very close to the experimental data. The fitted excitation lifetime τ equals 185 μs. Thus, as in the devices discussed in the previous section, this suggests that the low energy signal is due to excited state absorption

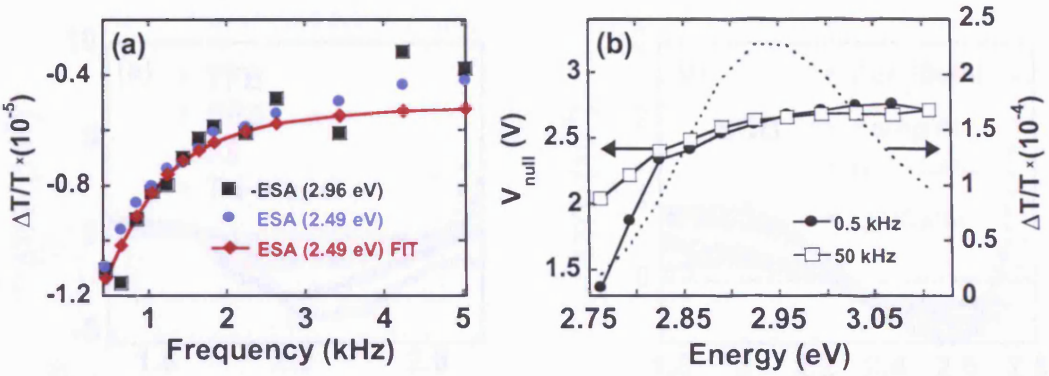

Figure 4.12: (a) $\Delta T/T(1\omega)$ (in-phase) frequency dependence measured at 2.49 eV (blue circles), together with a fit to the 2.49 eV signal (full line). The 'ESA' signal at 2.96 eV (black squares), 'extracted' from the total $\Delta T/T(1\omega)$ signal, as discussed in section 4.4.2, is also shown. (b) The nulling voltage as a function of photon energy, shown on the left-hand ordinate axis, measured at 0.5 and 50 kHz. The right-hand ordinate axis shows the $\Delta T/T(1\omega)$ response. (For both (a) and (b) the results were obtained using a short pass filter to screen the PL signal.)

by trapped charge, and hence, we assign this signal to ESA.

As in section 4.4.2, we investigated the possible presence of ESA at 2.96 eV, by measuring $\Delta T/T(1\omega)$ as a function of frequency, and separating the Stark and ESA frequency response. Indeed, as in section 4.4.2, we detected the presence of a signal whose frequency dependence is very similar to the frequency dependence of the ESA signal at 2.49 eV, as can be seen in Figure 4.12(a), where the ESA-like signal at 2.96 eV is shown in black squares (with the data multiplied by -1).

Importantly, as shown in Figure 4.12(b), V_{null} again has a significant dependence on photon energy. At 0.5 kHz, V_{null} increases from 1.35 V at 2.76 eV, to a maximum of 2.76 V at 3.07 eV, whereas at 50 kHz V_{null} increases from a minimum of 2.04 V to a maximum of 2.71 V.

4.6 Origin of the ESA Signal

To investigate the origin of the ESA signal, we first compare the low energy ESA spectra of TFB, PFB, F8 and tri-blend polymers in Figure 4.13(a). As can be seen, although the spectra have comparable magnitudes, the position and shape of the peaks are noticeably different. In contrast, shape profiles between different

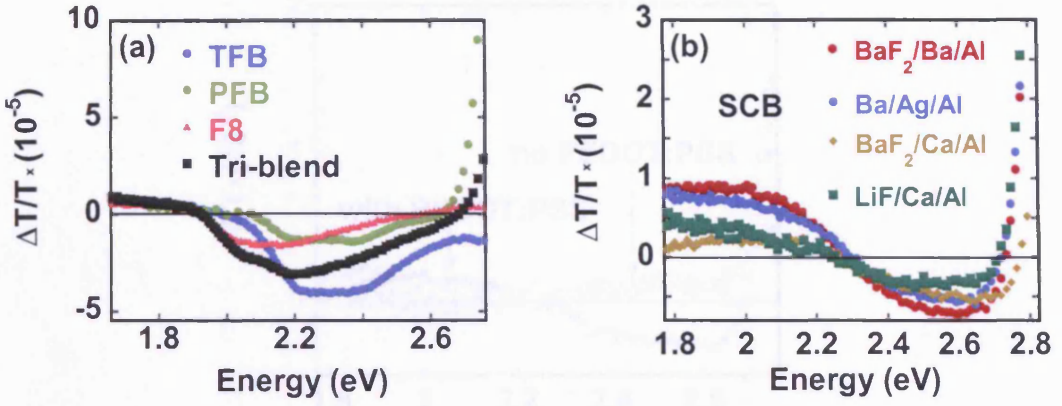

Figure 4.13: (a) ESA spectrum of TFB, PFB, F8, and tri-blend devices from 1.66 to 2.76 eV. The anode was ITO/PEDOT:PSS and the cathode was LiF/Ca/Al. The variability of ESA profiles suggests that the ESA signal is polymer dependent. (b) ESA spectrum of devices with four different cathodes (as indicated), in the range 1.77 to 2.82 eV. ITO/PEDOT:PSS was the anode and SCB was the emitting-layer. The similarity between different profiles suggests that the ESA signal is not cathode dependent.

devices containing the same polymer (data not shown here) are very similar or virtually identical in some cases. This suggests that the ESA signal is generated either within the polymer layer, or near the polymer-electrode interface. Figure 4.13(b) shows low energy ESA profiles of ITO/PEDOT:PSS/SCB/Cathode LEDs, with four different cathodes. Interestingly, the profiles are very similar, and all start with a positive $\Delta T/T(1\omega)$ signal near 1.8 eV, and then dip to a negative peak near 2.6 eV, presumably due to the appearance of excited state absorption. This similarity suggests that the ESA signal is not (directly) cathode dependent.

Figure 4.14 shows the ESA profile of SCB-based devices with and without the PEDOT:PSS layer. Interestingly, as can be seen, the ESA signal does not exist in the device without the PEDOT:PSS layer. We note that a similar observation was also reported by Brewer *et al.*[103]. Thus, the lack of ESA dependence on the cathode material, and its apparent dependence on the emitting-polymer, and on the presence of PEDOT:PSS, suggests that the ESA signal may be generated at the polyfluorene-PEDOT:PSS interface.

Furthermore, the ESA signal is significantly enhanced if the device is electrically driven above the EL onset for a period of several minutes. Figure 4.15 shows the

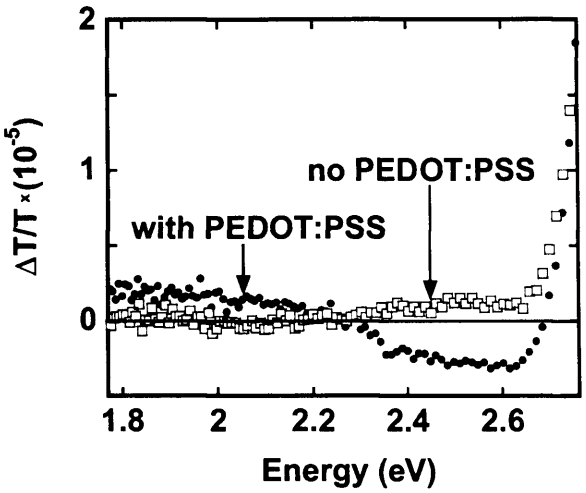

Figure 4.14: Low-energy ESA spectrum of a device with and without PEDOT:PSS, in the range from 1.77 to 2.76 eV. In this device, SCB was the active layer and LiF/Ca/Al was the cathode. The absence of an ESA peak in the device without PEDOT:PSS suggests that the ESA peak may result from interactions between PEDOT:PSS and the emitting-polymer layer.

ESA signal as a function of driving time in F8- and SCB-based devices. For F8, ESA increases from 0.8×10^{-5} to 3.2×10^{-5} after 1 minute of electrical driving (at 4.5 V bias), whilst for SCB ESA increases from 0.4×10^{-5} to 1.0×10^{-5} after 3 minutes (also at 4.5 V bias). Interestingly, we note that Poplavskyy *et al.*[101] and van Woudenbergh *et al.*[137] have reported a decrease in the hole injection barrier in polyfluorene-based LEDs with ITO/PEDOT:PSS anodes, when the devices were biased above the EL onset, due to electron trapping at the PEDOT:PSS/polyfluorene interface. Van Woudenbergh *et al.* reported that such effects only occur in devices that incorporate PEDOT:PSS[137], suggesting that trapping occurs at the PEDOT:PSS/polyfluorene interface. Furthermore, Lane *et al.*[102] and Brewer *et al.*[103] reported that such trapped charges may lead to full screening of the electric field inside the active layer (at high forward bias), which is reportedly also observed only in the devices that incorporate PEDOT:PSS[103].

On the basis of these considerations, our results can thus be explained in terms of electron trapping at the PEDOT:PSS/polyfluorene interface. In Figure 4.15, the increase in the ESA signal in the first few minutes of driving can then be explained by the increased density of trapped electrons at the interface.

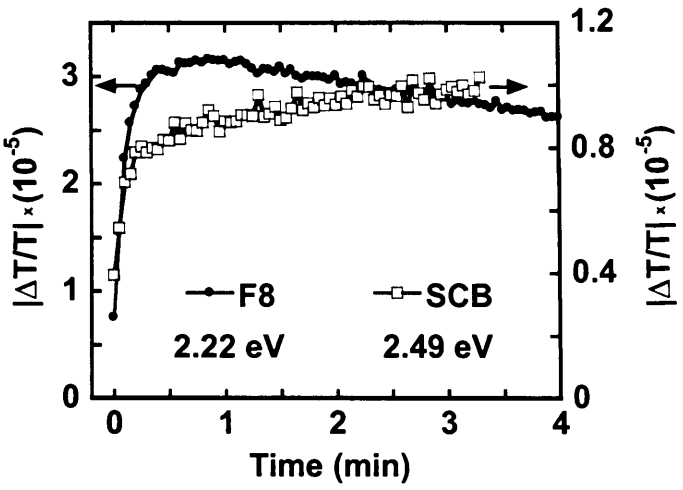

Figure 4.15: ESA signal as a function of electrical driving time, in ITO/PEDOT:PSS/EP/LiF/Ca/Al devices, subjected to 4.5 V bias. The active layer was either F8 or SCB. (Driving was repeatedly stopped/resumed so that the ESA signal could be measured.) ESA was measured either at 2.22 eV (F8), or 2.49 eV (SCB), and at $V_{dc} = 0$ V, $V_{ac} = 1$ V, f = 1 kHz.

4.7 Conclusion

In conclusion, the electromodulated signal created by trapped charges interferes with the electroabsorption and built-in voltage measurements of blue-emitting PLEDs with polyfluorene-based active layer, and ITO/PEDOT:PSS anode. This produces a significant dependence of the null-voltage, especially in the spectral region close to the linear absorption edge, on the measured frequency and energy. We have demonstrated a method for separating the trapped charge signal from the Stark-response signal. In addition, and more importantly, $\Delta T/T$ measurements at high frequencies (~50 kHz), and probe beam energies close to the Stark response peak, can 'profit' from especially high Stark-to-ESA signal ratio, allowing an estimate of the built-in voltage. We have also investigated the origin of the trapped charge signal, and our results indicate that it is likely to be due to electron trapping at the PEDOT:PSS/polyfluorene interface.

Chapter 5

Energy Level Alignment in ITO/PEDOT:PSS/Polyfluorene/ LiF/Ca/Al LEDs

We present built-in voltage measurements of polymer light-emitting diodes with the general structure ITO/PEDOT:PSS/emitting-polymer/LiF/Ca/Al, where ITO is indium tin oxide, PEDOT:PSS is poly(3,4-ethylene dioxythiophene) doped with poly (styrene sulfonate), and the emitting polymer is either poly(9,9-dioctylfluorene) (F8), poly(9,9-dioctyl-fluorene-co-bis-N,N'-(4-butyl-phenyl)-bis-N,N'-phenyl-1,4-phenylene-diamine) (PFB), poly(9,9-dioctylfluorene-co-N-(4-butylphenyl)-diphenylamine) (TFB), or a 60/20/20 % blend of these three polymers. We find that the built-in voltage is polymer dependent, suggesting pinning of electrode Fermi level to the polymer bipolaron levels. For example, in comparison to the F8-only device, the built-in voltage of the blend-based device is lower by $\sim$ 0.3 V, suggesting in particular the pinning of the PEDOT:PSS Fermi level to the PFB HOMO level. Cyclic voltammetry measurements support these conclusions. Assuming an effective LiF/Ca/Al work function of $\sim$ 2.0 eV, the measured built-in voltages are in excellent agreement with the basic theory of alignment of the chemical potential across the PLED heterostructure.

5.1 Introduction

Following the success of poly(9,9-dioctylfluorene) (F8) as a highly efficient blue emitter[138], polyfluorene-based homo- and co-polymers have emerged as the leading candidates for blue-emitting diodes[17]. However, in many of these polymers the injection and/or transport of one type of charge carrier is favoured over the other leading to low electroluminescence (EL) efficiencies and brightnesses. An effective approach to improving the charge imbalance is to blend the emissive material with hole-transporting and/or electron-transporting polymers[15]. By the appropriate choice of blend composition, the properties of the individual polymer components are preserved in the blend thus creating a new material with improved charge balance[139]. For this reason, blends are often significantly brighter and more efficient than the single component diodes. In addition to F8, PFB [poly(9,9-dioctyl-fluorene-co-bis-N,N'-(4-butyl-phenyl)-bis-N,N'-phenyl-1,4-phenylenediamine)] and TFB [poly(9,9-dioctylfluorene–co–N-(4-butyl- phenyl)-diphenylamine)] are among the more widely used polyfluorene-based polymers, and their chemical structure, together with their HOMO and LUMO levels, is shown in Figure 5.1. We note that some of the HOMO and LUMO values are slightly different from the literature data[15], but this is not unusual, since the energy levels in conjugated polymers are known to vary between different batches.

In a polymer light-emitting diode (PLED) with asymmetric electrode work functions, electrons are transferred from the electrode with the smaller work function to the electrode with the larger work function, resulting in the formation of the so-called built-in voltage (V_{BI}). Notably, eV_{BI} (where e is the electron charge) is strongly correlated to the difference between the anode and the cathode work functions (ΔW_F). If the electrode Fermi energy levels lie within the emitting polymer bipolaron gap, and in the absence of electric dipoles at polymer/electrode interface(s), eV_{BI} is equal to ΔW_F. More generally, the built-in voltage can be expressed as[100]:

$$eV_{BI} = E_G - \Phi_B(cathode) - \Phi_B(anode), \tag{5.1}$$

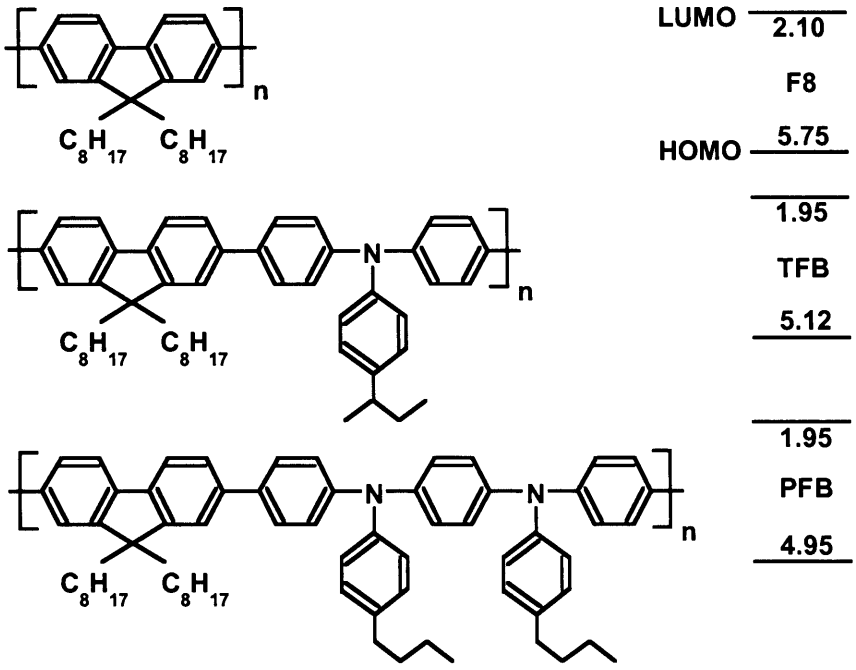

Figure 5.1: Chemical structures of poly(9,9-dioctylfluorene) and its co-polymers (full names given in the text). The associated HOMO and LUMO levels, based on cyclic voltammetry measurements by Ilaria Grizzi of CDT, are also indicated. The uncertainty in HOMO and LUMO values is ± 0.05 V.

where E_G is the polymer energy gap, and Φ_B is the barrier height at the polymer electrode interface. The advantage of this relation is that it is applicable even in the presence of interface dipoles and electrode Fermi level pinning at the polymer interface. Note that it states that the maximum V_{BI} is achieved when the energy barrier at both of the electrode interfaces is zero.

The built-in voltage can be measured by applying externally a voltage of the form $V = V_{dc} + V_{ac}\sin(\omega t)$ across the diode. The resulting modulation of the electric field across the diode modulates the intensity of the probe beam through the Stark effect[82], and generates an eletroabsorption (EA) signal which can then be measured using a lock-in amplifier, as already discussed in Chapter 3. For the conditions pertinent to equation 5.1, the EA signal obeys the following relation[72]

$$\Delta T/T(1\omega) \propto 2Im\{\chi^3(h\nu)\}V_{ac}(V_{dc} - V_{BI})\sin(\omega t + \theta), \tag{5.2}$$

where $Im\{\chi^3(h\nu)\}$ is a function of the imaginary part of the third order dielectric susceptibility, h is Planck's constant, ν is the photon frequency, and θ is the phase

of the signal with respect to the applied ac voltage. According to equation 5.2, $\Delta T/T(1\omega)$ varies linearly with V_{dc}, and passes through zero at $V_{dc} = V_{BI}$. The built-in voltage can thus be measured by finding the dc voltage at which the EA signal vanishes.

Here, we have employed EA spectroscopy, together with cyclic voltammetry measurements, to probe the built-in voltage and energy level alignment in light-emitting diodes whose active layer consisted of either F8, TFB, PFB, or a blend of these three polymers. The anode consisted of the hole transport interlayer, poly(3,4-ethylene dioxythiophene) doped with poly(styrene sulfonate) (PEDOT:PSS), deposited on top of indium tin oxide (ITO), and the cathode was LiF/Ca/Al. The EA measurements of these devices were presented in Chapter 4, and they indicate that the Stark signal is mixed with a smaller intensity signal, generated by trapped electronic charge at the PEDOT:PSS/polyfluorene interface. Such trapped charge has also been observed by several authors[101-103,137], all of whom argued that the charge is confined in the narrow region near the PEDOT:PSS/polyfluorene interface. Lane *et al.* estimated the thickness to be on the order of 0.2 Å[102], whilst van Woudenbergh *et al.* suggested a thickness on the order of 10 Å[137]. The effect of such trapped charge on the PLED internal field is shown schematically in Figure 5.2. A non-uniform field is expected at the anode/polyfluorene interface, but, importantly, the field in the bulk of the active layer (whose thickness is close to 70 nm), is expected to be uniform. For such constitution of the active layer, the Stark response of the polymer bulk is likely to dominate $\Delta T/T(1\omega)$, in agreement with our experimental observations[140]. Thus, although in Chapter 4 we found that V_{null} varies significantly with photon energy in the spectral region where the Stark response is small, the variation decreased substantially near the peak of the Stark response, and decreased even further when the measurements were performed at high frequencies (50 kHz), where the trapped charge signal is substantially lower. We were thus able to estimate the built-in voltage of the TFB-based device, and found it to be close to 3.1 V, with the upper uncertainty limit of 0.05 V, and the lower uncertainty limit of 0.1 V. Here, we estimate the built-in voltage of F8, PFB and tri-blend devices, and

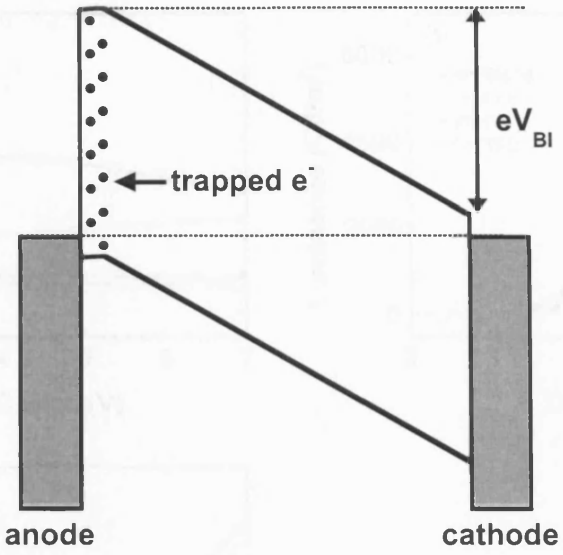

Figure 5.2: Schematic energy level diagram of a PLED with a high density of trapped electrons in the narrow region close to the anode/emitting-layer interface, at no applied voltage. Due to the trapped charge, the electric field is non-uniform close to the interface, but uniform in the bulk of the active layer.

then investigate, using the available data, if the results agree with the basic theory of alignment of the chemical potential across the PLED structure. We employ cyclic voltammetry to investigate if the tri-blend HOMO level is determined by the minority component with the least negative HOMO level (PFB), or the majority component with the more negative HOMO level (F8). Assuming that the cathode work function is $\sim 2.0 \pm 0.1$ eV, and using the previously established anode work function[75], and polymer HOMO and LUMO levels (Figure 5.1), the predicted V_{BI} values are in excellent agreement with the experimental results. Our results indicate that in the blend device the anode Fermi level is pinned to the PFB HOMO level, whilst the LiF/Ca/Al Fermi energy is pinned to the F8 LUMO level. This implies that the energy barrier at both of the electrode/polymer interfaces is close to zero, in agreement with the observed high efficiency of blend devices.

5.2 Experimental

The details of electroabsorption measurements, as well as the PLED fabrication processes, are described in Chapter 4. Following fabrication, the devices were tested

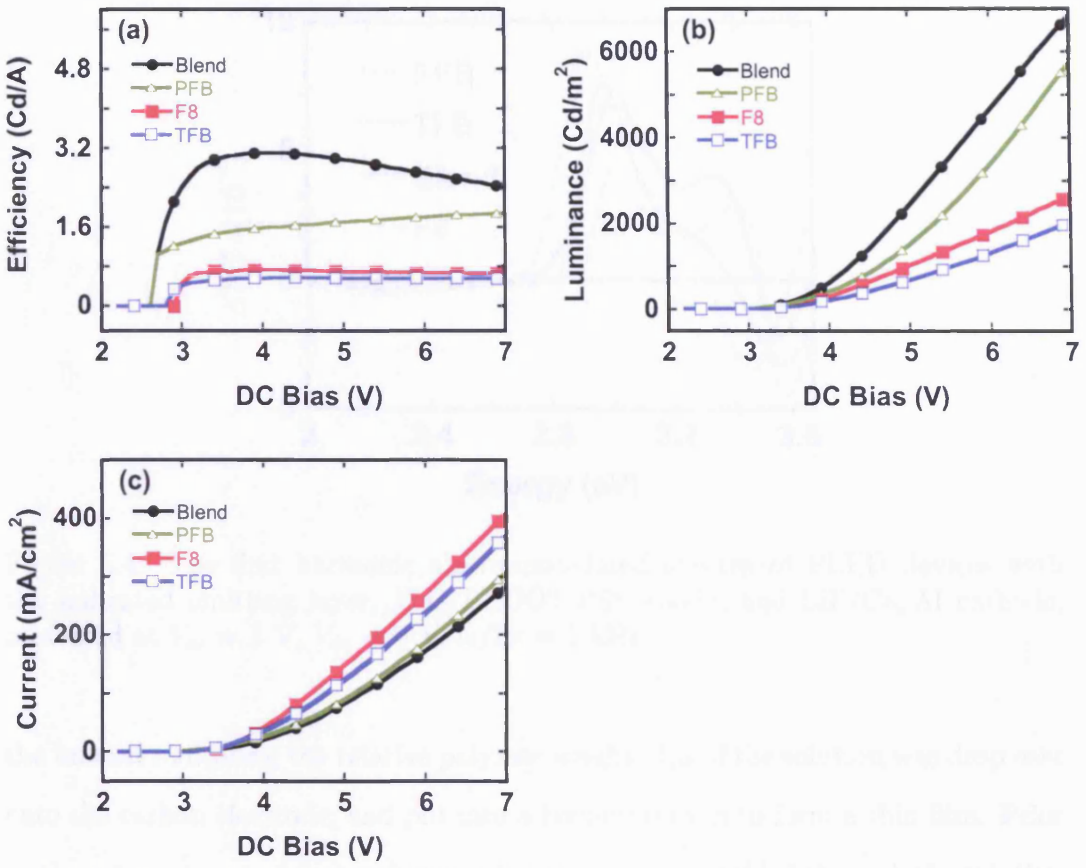

Figure 5.3: (a) Efficiency vs V_{dc}, (b) Luminance vs V_{dc}, and (c) Current vs V_{dc} graphs of ITO/PEDOT:PSS/emitting-polymer/LiF/Ca/Al devices investigated in this chapter. The active layer was either F8, TFB, PFB, or a blend of these three polymers. (Data provided by Dr. Matthew Roberts of CDT.)

at Cambridge Display Technology for efficiency, luminance and current characteristics, and the results are shown in Figure 5.3. As can be seen, the tri-blend has the highest efficiency and luminance, followed by PFB, whereas the efficiency and luminance of F8 and TFB is significantly lower.

Cyclic voltammetry (CV) measurements were performed as described by Janietz *et al.*[144], in an electrolyte solution of 0.1 M tetrabutylammonium tetrafluoroborate (TBABF4) dissolved in anhydrous acetonitrile. The working electrode was (glassy) carbon, the counter electrode was a platinum wire, whereas the reference electrode was Ag/AgCl. The polymers (purchased from American Dye Source) were dissolved in a 2 % xylene solution (p-xylene 99% HPLC grade from Aldrich), and the tri-blend was made from F8 (60%), TFB (20%) and PFB (20%), with the number in

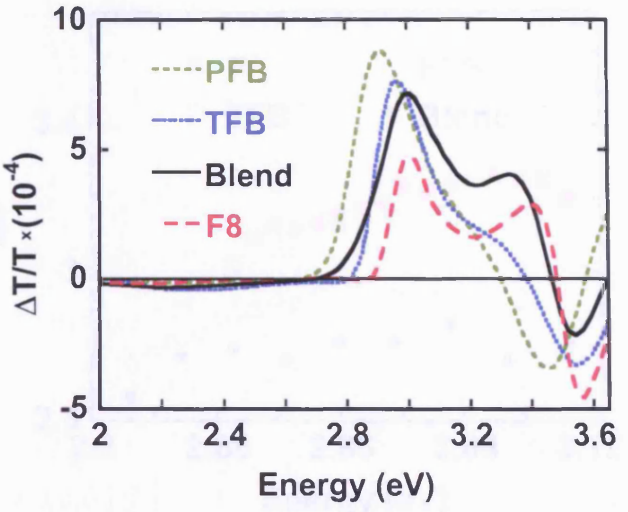

Figure 5.4: The first harmonic electromodulated spectra of PLED devices with the indicated emitting layer, ITO/PEDOT:PSS anode, and LiF/Ca/Al cathode, measured at $V_{ac} = 1$ V, $V_{dc} = 0$ V, $\omega/2\pi = 2$ kHz.

the bracket indicating the relative polymer weight. 1μl of the solution was drop cast onto the carbon electrode, and put into a (vacuum) oven to form a thin film. Prior to the measurement of each polymer, nitrogen gas was bubbled through the solution for at least ten minutes, to remove the dissolved atmospheric gases.

5.3 Results

Figure 5.4 shows the electromodulated (EM) spectra of devices with PFB (green broken line), TFB (blue dotted line), F8 (dashed red line) and tri-blend (full black line) emitting-polymer layers. Apart from a small peak in the vicinity of 2.3 eV, ascribed to excited state absorption by trapped charge (and discussed in more detail in Chapter 4), the spectra are characterised by larger peaks in the energy range 2.7 $\leq h\nu \leq$ 3.7 eV. The PFB Stark onset occurs near 2.70 eV, and the signal reaches the maximum value of 8.79×10^{-4} at 2.92 eV. In comparison, the TFB spectrum is blue-shifted, with the onset occurring near 2.80 eV, and the maximum (7.65×10^{-4}) occurring at 2.97 eV. The F8 spectrum is blue-shifted even further, and the onset is at 2.87 eV, whereas the maximum (4.76×10^{-4}) is at 3.01 eV. As expected, the blend onset coincides with that of the material with the smallest energy gap, that is PFB,

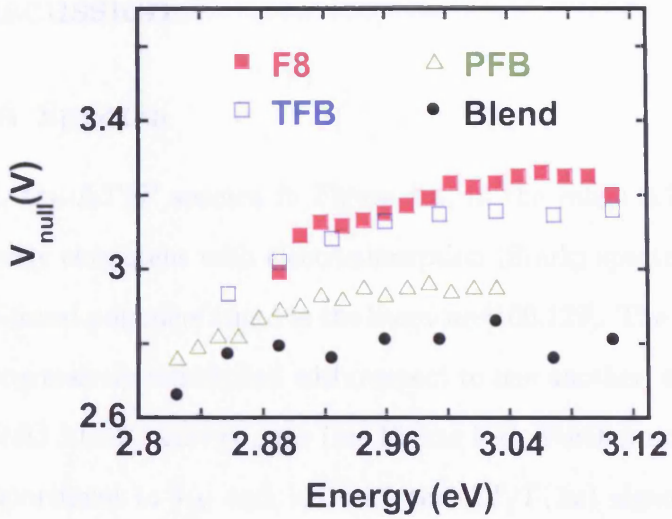

Figure 5.5: V_{null}, measured at 50 kHz, as a function of incident photon energy in PLEDs with the indicated active layer.

although the signal magnitude is smaller, probably due to the small concentration of PFB.

Figure 5.5 shows V_{null} as a function of photon energy in the blend, PFB, TFB and F8 devices. Interestingly, in the blend, from 2.85 to 3.11 eV, V_{null} is constant at 2.81 V, with a maximum interval of variation of $\pm$ 0.05 V. We note that, in the same energy range, and using the data shown in Figure 5.4, $\Delta T/T(1\omega)$ varies from 2.02×10^{-4} to 7.18×10^{-4}. At 2.82 eV, where $\Delta T/T(1\omega)$ is six times lower than at the peak, V_{null} is smaller, and equals 2.66 V. For other polymers there is a more visible variation of V_{null} with energy. For PFB, in the energy range 2.82 to 2.90 eV (where $\Delta T/T(1\omega)$ varies from 4.77×10^{-4} to 8.77×10^{-4}), V_{null} increases progressively from 2.76 to 2.90 V, and for energies in the range 2.92 to 3.03 eV (where $\Delta T/T(1\omega)$ varies from 8.79×10^{-4} to 5.40×10^{-4}), V_{null} has a constant value of 2.94 $\pm$ 0.02 V. In the TFB device, from 2.85 to 2.98 eV (where $\Delta T/T(1\omega)$ varies from 1.14×10^{-4} to 7.65×10^{-4}), V_{null} increases from 2.93 to 3.13 V. From 2.98 to 3.1 eV (where $\Delta T/T(1\omega)$ decreases by a half), V_{null} is constant at 3.14 $\pm$ 0.01 V. In the F8 device, within the range 2.90 to 3.11 eV (where $\Delta T/T(1\omega)$ varies from 0.49×10^{-4} to 4.76×10^{-4}), V_{null} lies between 3.09 and 3.26 V, with the values tending to increase with increasing energy. At 2.89 eV, near the Stark onset (where $\Delta T/T(1\omega) = 0.12 \times 10^{-4}$), V_{null} is lower and equals 2.99 V.

5.4 Discussion

5.4.1 EA Spectra

As expected, the $\Delta T/T$ spectra in Figure 5.4, in the range $2.7 \leq h\nu \leq 3.7$ eV, are qualitatively consistent with electroabsorption (Stark) spectra of blue-emitting polyfluorene-based polymers found in the literature[100,122]. The F8, TFB and PFB peaks are progressively red-shifted with respect to one another, consistent with the trend in HOMO LUMO energy gaps (see Figure 5.1). Furthermore, the $\Delta T/T(1\omega)$ signal is proportional to V_{dc} and V_{ac}, and the $\Delta T/T(2\omega)$ signal is constant as a function of V_{dc} and proportional to V_{ac}^2 (data not shown here). Such behaviour is consistent with the Stark response, and indicates (a) that the bulk of the polymer layer is free of significant concentration of space charge, and (b) that $\Delta T/T$ is dominated by the Stark response of the active layer.

5.4.2 V_{null} vs Photon Energy

The most striking feature of Figure 5.5 is the large variation of V_{null} with photon energy for the single polymers. As discussed in Chapter 4, if $\Delta T/T(1\omega)$ in the energy range $2.8 \leq h\nu \leq 3.1$ eV consisted only of the Stark response of the polymer layer, which was free of space charge (so that the field and dielectric susceptibility were spatially uniform), V_{null} would be expected to be constant with energy, and would equal V_{BI}. However, the presence of any trapped charge generates a small $\Delta T/T(1\omega)$ signal, and thus a variation of V_{null} with energy.

Experimentally, we find that the degree of variation depends on device types and components. For instance, as shown in Chapter 3, V_{null} is constant with energy in an ITO/polyfluorene/Al device. Here, interestingly, in the blend device, V_{null} is constant over a relatively wide energy range around the Stark response peak, even though the Stark response varies by more than three and a half times in magnitude. This means that the trapped charge signal has no significant influence on V_{null}, which supports the argument that the bulk of the polymer film is free of space charge. Thus, in the blend device, taking the constant V_{null} value to be equal to the

built-in voltage, we measure $V_{BI} = 2.81 \pm 0.05$ V.

In the F8 device, V_{null} instead changes by 0.16 V over the energy range in which the Stark response magnitude changes by more than nine times. This demonstrates that the influence of the trapped charge signal on V_{null} is limited, particularly near the Stark response peak. Thus, selecting the V_{null} values measured at energies near 2.96 eV (where $V_{null} = 3.15$ V), just below the Stark peak, as recommended by Campbell *et al.*[72] and Brown *et al.*[55], we consider that V_{BI} equals 3.15 V, with the maximum uncertainty of $\pm$ 0.1 V. In the PFB device, V_{null} equals 2.94 V at energies near the Stark peak, where the Stark response contributes close to 99 % of $\Delta T/T(1\omega)$[141]. Thus, we expect that the trapped charge signal there has little influence on V_{null}. In view of this, and considering the measured V_{null} variation between 2.82 and 3.03 eV, we estimate that V_{BI} in the PFB device equals 2.94 V, with the upper uncertainty limit of 0.05 V, and the lower uncertainty limit of 0.1 V. For the TFB device, as mentioned in the introduction, we consider that V_{BI} equals 3.1 V, with the upper uncertainty limit of 0.05 V, and the lower uncertainty limit of 0.1 V.

Thus, V_{BI} varies significantly between the devices, by as much as 0.3 V between the F8, TFB devices on the one hand, and the blend device on the other hand. The V_{BI} variation between devices whose electrodes are of the same type, and vary only in the composition of the active layer, suggests pinning of at least one of the electrode Fermi levels to a polymer bipolaron level. In the PFB device for example, we expect that the PEDOT:PSS work function (5.2 $\pm$ 0.1 eV[75]) is pinned to the polymer HOMO level (4.95 eV). Interestingly, the blend V_{BI} is even lower than in PFB, suggesting that pinning occurs at both blend/electrode interfaces. In this case, the anode Fermi level can only be pinned by a minority component, PFB or TFB, since the F8 HOMO level is positioned at 5.75 eV.

To test this, in the absence of any available blend HOMO and LUMO data, we used the cyclic voltammetry (CV) technique to investigate if the HOMO level in the tri-blend is determined by the majority component with a more negative HOMO level, or a minority component with a less negative HOMO level.

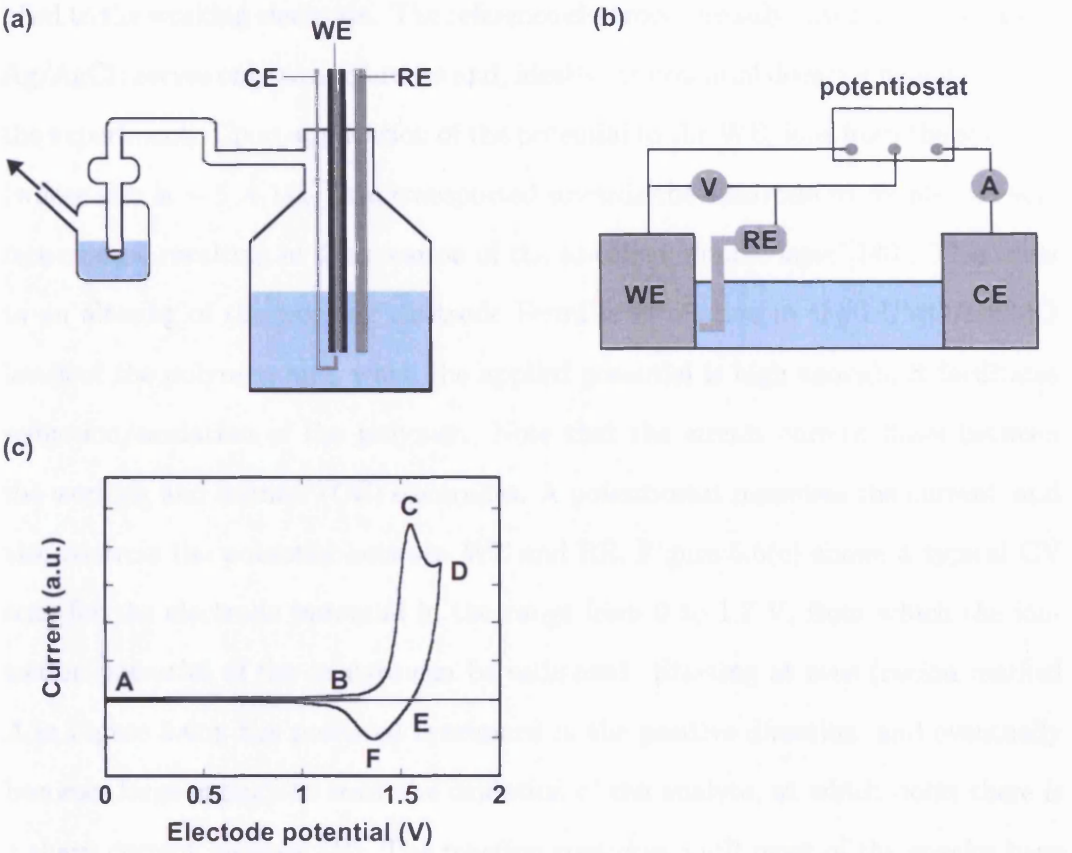

Figure 5.6: (a) Schematic of a typical experimental set-up for cyclic voltammetry measurements (adapted from [142]). WE is the working electrode, CE is the counter electrode, and RE is the reference electrode. (b) Schematic showing the connections between the potentiostat and the electrodes (from [143]). (c) A typical cyclic voltammetry scan (see text for discussion).

5.4.3 Cyclic Voltammetry Measurements

Cyclic voltammetry is a particularly useful electroanalytical tool[142,143], which can be used to probe the ionisation potential (I_p) and electron affinity (E_a) of conjugated polymers[144]. As illustrated in Figures 5.6(a) and (b), in a typical experimental set-up, three electrodes are immersed in an electrolyte solution, which conducts electricity as a result of ions dissolved in the solvent. To effectuate the removal of dissolved atmospheric gases, there is an additional provision for passing an inert gas through the solution. The main electrode is the working electrode (WE), which is insulated so that there is no electrical contact with the electrolyte, except at the top, which is covered by a thin film of the material to be analysed (the analyte). During the experiment, a potential specified relative to the reference electrode (RE) is ap-

plied to the working electrode. The reference electrode (usually silver/silver chloride, Ag/AgCl) serves only as a reference and, ideally, its potential does not change during the experiment. Upon application of the potential to the WE, ions from the solution (whose size is ~ 5 $\mathring{A}$[145]) are transported towards the electrode to counter its surface charge, resulting in the creation of the so-called 'double layer'[146]. This leads to an altering of the working electrode Fermi level relative to the LUMO/HOMO levels of the polymer, and, when the applied potential is high enough, it facilitates reduction/oxidation of the polymer. Note that the circuit current flows between the working and counter (CE) electrodes. A potentiostat measures the current, and also controls the potential between WE and RE. Figure 5.6(c) shows a typical CV scan for the electrode potential in the range from 0 to 1.7 V, from which the ionisation potential of the analyte can be estimated. Starting at zero (region marked A in Figure 5.6c), the potential is scanned in the positive direction, and eventually becomes large enough to start the oxidation of the analyte, at which point there is a sharp current increase (B). The reaction continues until most of the species have been oxidised so that, after reaching the peak (C), the current starts to decrease. The potential is then scanned in the opposite direction (D), towards zero, and below a certain potential the reduction of the (oxidised) analyte takes place, resulting in a negative current (E). As the concentration of oxidised species becomes significantly reduced, the current reaches its negative peak (F), and then decays towards zero as the potential is scanned to zero. A similar process occurs when the potential is scanned negatively (to probe the electron affinity), although the analyte first becomes reduced, resulting in a negative current, which reaches a peak and then decays.

In the measurements of conjugated polymers, using the Ag/AgCl reference electrode, the following relationship between I_p and the onset potential for oxidation E'_{ox} (corresponds to potential at B in Figure 5.6c), and between E_a and the onset potential for reduction E'_{red}, is applicable[144]:

$$I_p = (E'_{ox} + 4.4)eV \tag{5.3}$$

$$E_a = (E'_{red} + 4.4)eV. \tag{5.4}$$

The relationship is based on a detailed comparison between theoretical calculations and experimental electrochemical measurements. The onset potentials represent the minimum I_p and the maximum E_a for the inhomogeneous ensemble of polymer chains present in a typical sample[144].

In our CV measurements, we found that all of the tested polymer films could be both reversibly oxidised and reduced, in agreement with the findings by Janietz *et al.*[144], indicating that the samples were chemically stable and free from impurities. In Figure 5.7, we show a comparison of the measured cyclic voltammetry scans of the F8(60%)/TFB(20%)/PFB(20%) tri-blend, and the two components with the lowest oxidation onsets, PFB and TFB, in the electrode potential range from 0 to 1.25 V. In the forward potential scan, from 0 to 1.25 V, the blend shows two distinct oxidation peaks, at 0.81 V and 1.10 V. Another peak due to F8 (not shown here), was observed near 1.54 V. As expected, the oxidation peaks of PFB and TFB films occur at approximately similar potentials, at 0.85 and 1.08 V respectively[147], and we therefore ascribe the two oxidation peaks in the blend to the oxidation of PFB and TFB polymers respectively. These results therefore confirm the expectation that the blend HOMO level is determined by the component with the highest HOMO level, PFB.

5.4.4 The Built-in Voltage and Energy Level Alignment Across the PLED

We now consider if the measured built-in voltages can be accounted for by the basic theory of alignment of the chemical potential across the PLED heterostructure. In Figure 5.8 we show the relevant energy levels of the various components that are incorporated into our PLEDs. The anode work function is based on the work by Brown *et al.*[75], and the F8, TFB, PFB HOMO and LUMO levels have been provided by CDT. Based on our cyclic voltammetry results, we consider that the blend HOMO level is determined by PFB, and similarly, that the LUMO level is

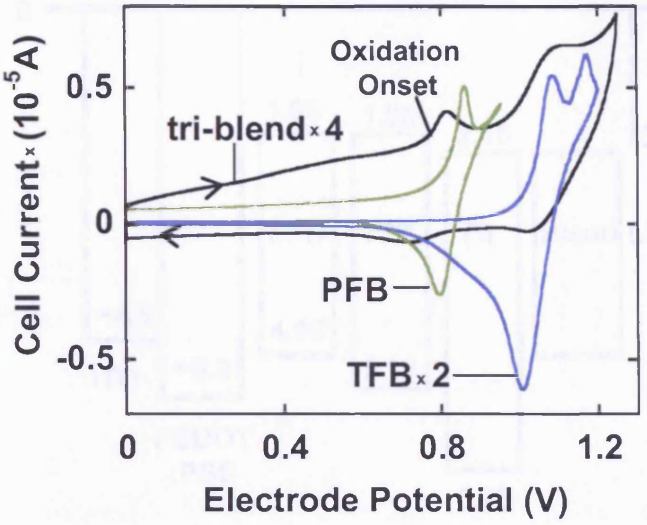

Figure 5.7: The cyclic voltammogram of the F8/TFB/PFB tri-blend (multiplied by 4), and of the two components with the lowest oxidation potentials, TFB (multiplied by 2) and PFB. The positions of the two lowest tri-blend oxidation peaks match those of PFB ($\sim$ 0.8 V) and TFB ($\sim$ 1.1 V). This indicates that PFB determines the tri-blend HOMO level. The scans were recorded at 20 mV/s.

determined by its majority component F8, since F8 has the lowest LUMO level (2.10 eV). Note that, regardless of the LiF/Ca/Al work function (but assuming it to be the same in all devices), the expected V_{BI} difference between TFB and PFB devices is 0.17 V, which is in excellent agreement with the observed difference of 0.16 V, and the expected V_{BI} difference between the F8 and blend device is 0.25 V, which is close (within the experimental error) to the observed difference of 0.34 V. Note that the reduction in V_{BI} of the blend device relative to the F8-only device is directly related to the decrease in the hole injection barrier, effectuated by the introduction of PFB and TFB components. As can be seen in Figure 5.3(a), the efficiency of the blend device is many times higher in the blend than in the F8-only device as a result (in part at least) of the reduced hole injection barrier.

Now, we do not know the LiF/Ca/Al work function, but we note that for the PFB built-in voltage of 2.94 V a value close to 2.0 eV would be required. Interestingly, this value fits excellently with our other V_{BI} results. For the TFB device, supposing that V_{BI} is determined by the difference between the TFB HOMO level and the effective cathode work function, we expect that $V_{BI} = 3.12$ V, which is very close

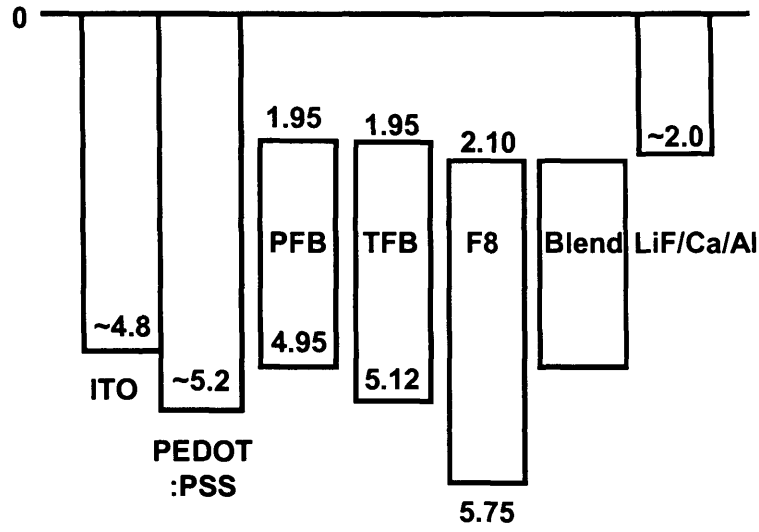

Figure 5.8: Energy levels of the different materials in ITO/PEDOT:PSS/polyfluorene/LiF/Ca/Al LEDs. ITO and PEDOT:PSS work function is based on the work by Brown *et al.*[75]. The single polymer HOMO and LUMO levels have been provided by CDT. The LiF/Ca/Al work function was chosen to fit our V_{BI} results. The data is given in eV, and the uncertainty in HOMO and LUMO levels is $\pm$ 0.05 eV.

to the measured value of 3.1 V. (Note that, due to the $\pm$ 0.05 eV uncertainty in the HOMO and LUMO values, the maximum uncertainty in the expected V_{BI} is $\pm$ 0.1 eV.) In the F8 device, for V_{BI} determined by the difference between the anode work function and the F8 LUMO level, we would expect V_{BI} = 3.10 V, which is very close to the measured value of 3.15 V. In the blend device, supposing that V_{BI} is determined by the difference between the PFB HOMO and F8 LUMO level, we would expect that V_{BI} = 2.85 V, which is very close to the measured value of 2.81 V. The comparison between V_{BI} values measured by electroabsorption (data represented by squares), and V_{BI} values expected from the energy levels shown in Figure 5.8 (represented by triangles), is plotted in Figure 5.9. The maximum uncertainty interval is also shown.

Now, to produce an effective cathode work function of 2.0 eV, the LiF layer would need to decrease the effective Ca work function, which is close to 2.8 eV[148], by approximately 0.8 eV. We note that previous studies have shown that a thin LiF layer does indeed decrease the cathodic work function. In a study by Brown *et al.*[99], also involving LiF/Ca/Al cathodes, the LiF layer decreased the electron injection

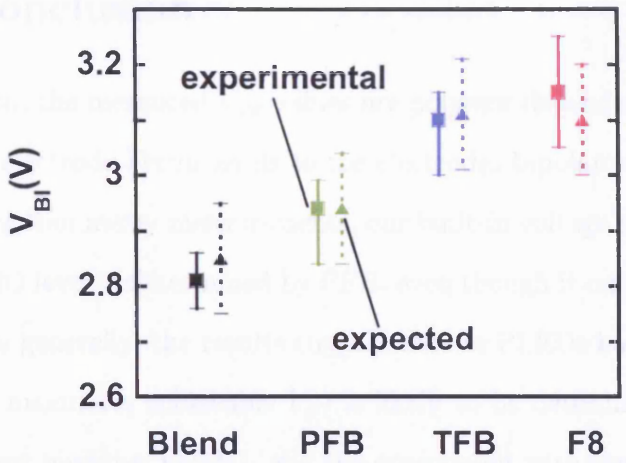

Figure 5.9: A comparison of the built-in voltage values measured by electroabsorption (shown in squares), and the built-in voltage values expected from the energy level diagram shown in Figure 5.8 (triangles). The maximum uncertainty interval is also shown.

barrier by at least 0.3 eV[149]. Another study by Brown *et al.*[150], involving LiF/Al cathodes, showed that a LiF layer decreased the effective Al work function (4.3 eV[100,148]) by 1.2 eV, to produce an effective work function of 3.1 eV. In another study involving LiF/Al cathodes, Shaheen *et al.*[151] reported that the fluoride layer decreased the Al work function by 1.8 eV, and produced an effective work function of 2.5 eV. Interestingly, the mechanism for the decrease is thought to involve either the generation of a dipole at the fluoride-metal interface[152], or dissociation of the fluoride to form a low work function contact[153], or a combination of the two[100]. Which mechanism dominates may depend crucially on evaporation and fabrication conditions[55]. Note that, since the Li work function is $\sim$ 2.3 eV (lowest found in literature[100,154]), the dipole mechanism is required to explain at least a part of the work function decrease.

In view of these considerations, it is conceivable that a thin LiF layer can decrease the effective Ca work function from 2.8 to 2.0 eV. Possibly, the degree of reduction may depend on the concentration of moisture[155] or other impurities during evaporation.

5.5 Conclusion

In conclusion, the measured V_{BI} values are polymer dependent, which suggests pinning of the electrode Fermi levels to the electrodes bipolaron levels. In conjunction with cyclic voltammetry measurements, our built-in voltage results indicate that the blend HOMO level is determined by PFB, even though it only makes up 20 % of the blend. More generally, the results suggest that in PLEDs based on similar polymer blends, the maximum achievable V_{BI} is likely to be determined by the component with the most negative LUMO, and the component with the least negative HOMO level. This implies that the anode Fermi level is pinned to the positive bipolaron level in the PFB, blend and TFB devices, and that the cathode Fermi level is pinned to the negative bipolaron level in the F8 and blend devices. Due to the differences in the polymer HOMO and LUMO levels, the blend device, and to a lesser extent the PFB device, has a lower built-in voltage than the TFB and F8 devices. In regard to the PLED efficiency, our results thus give a direct evidence for the reduction in the hole injection barrier brought about by the introduction of PFB into the F8 film, which is evident in the substantial increase in PLED efficiency. Finally, our results indicate that the effective LiF/Ca/Al work function in our devices is 2.0 $\pm$ 0.1 eV. We note that for this value of the work function the expected electron injection barrier is close to zero, which agrees with the existing knowledge about these devices[156].

Chapter 6

Degradation Effects in Blue Light-Emitting PLEDs

In this chapter, we employ electroabsorption (EA) spectroscopy in the study of degradation effects in blue light-emitting polymer diodes, that also incorporate a hole-injection layer, poly(3,4-ethylene dioxythiophene) doped with poly (styrene sulfonate) (PEDOT:PSS). We systematically compare the EA response of undriven and half-life driven devices, i.e. devices driven to half the initial luminance of 100 Cd/m^2. The measurements of the EA nulling voltage, and of the sub-gap electromodulated $\Delta T/T(1\omega)$ signal (which is believed to be generated by trapped electronic charge at the PEDOT:PSS/emitting-polymer interface), all point to the degradation of PEDOT:PSS, and in particular its interface with the emitting-polymer. This is corroborated by the evidence found in the literature. We also investigate the nature of the improvement in the performance, which we have frequently observed in these devices, when they are initially electrically driven for a period of a few minutes. For instance, when driven at a constant dc bias, the current (I) and electroluminescence (EL) intensity increase progressively, by up to $\sim$ 20 % (in the first $\sim$ 4 minutes*) in some cases. Interestingly, in all such cases, we find that the trapped charge $\Delta T/T(1\omega)$ signal increases concomitantly with I and EL, indicating that the increase is brought about by an improvement in the hole injection/transport across the PEDOT:PSS/emitting-polymer interface.*

6.1 Introduction

One of the key issues for the application of polymer light-emitting diodes (PLEDs) is their stability. Although the lifetime of the early devices was less than a few minutes, owing to the tremendous progress achieved over the last fifteen years, the lifetime of today's devices, especially the red- and green-emitting ones, is frequently in excess of 10,000 hours (sufficient for commercial applications). The lifetime of the blue-emitting diodes on the other hand, required for the development of full-colour displays, is often significantly shorter (for instance, ~4000 hours in a recent report[17,57]). Interestingly though, very recently, Cambridge Display Technology (CDT) has announced the development of blue-emitting PLEDs with projected lifetimes of 100,000 hours, and red- and green-emitting PLEDs whose projected lifetimes exceed 100,000 hours[157].

Polyfluorene (PF) and its derivatives have emerged as some of the most promising candidates for blue-emitting PLEDs[17]. They possess the right combination of properties, such as efficient electroluminescence (EL), pure blue colour, high charge-carrier mobility and good processability. The 9,9-alkyl chains ensure polymer solubility in organic solvents, but do not significantly affect the π-system electronic structure[158]. One concern with PLEDs based on PFs is that a low-energy emission band (2.2 - 2.3 eV) appears during operation, which shifts the emission colour from the desired blue ($\sim$ 2.9 eV), to an undesired blue-green[159]. Initially, this was attributed to the formation of aggregates and/or excimers[160,161], but List *et al.*[158,162], and Gong *et al.*[163], later gave evidence suggesting that such behaviour is generated by carbonyl defect states. A small concentration of keto defects can efficiently trap large number of excitons, and can act as guest emitters with a lowered emission energy[158,162]. Keto defects can be generated from the small amount of monoalkylated monomers (Figure 6.1a)[164], which are particularly susceptible to oxidation/photooxidation[158,162]. In the presence of oxygen, keto defect sites can also be formed from the more stable 9,9-dialkylated PF (DA-PF) monomers by photo- or electro-oxidative degradation[162]. Figure 6.1(b) shows the photoluminescence (PL) spectrum of a pristine DA-PF film (full line), whose emission, after

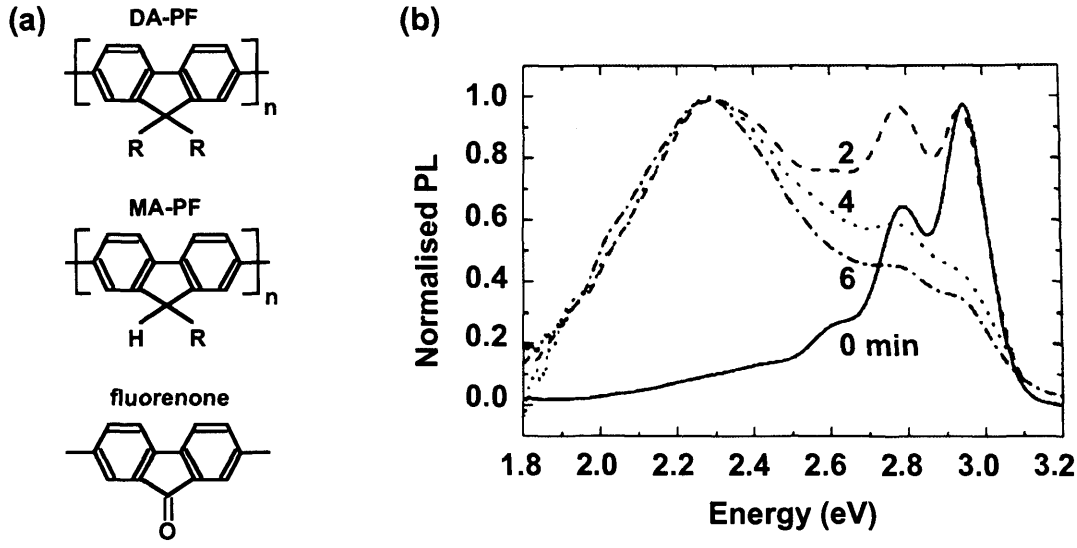

Figure 6.1: (a) Chemical structure of the 9-monoalkylated PF (MA-PF), the 9,9-dialkylated PF (DA-PF), and PF with a keto defect site. MA-PF is very susceptible to oxidation, and the formation of keto defects[158]. (b) PL emission spectrum of a pristine DA-PF film (full line), and after photooxidation with a 1000 W xenon lamp under air for 2, 4 and 6 minutes. (from [162])

exposure to intense light under air, shifts from higher energies (peaks near $\sim$ 2.8 and $\sim$ 2.9 eV) to lower energies (one broad peak near 2.3 eV)[162]. Similarly, under operation in air, the EL spectrum of PLEDs made with DA-PF shifts from higher energies to the 2.3 eV emission band[162].

The morphology of PF films can play an important role in determining the device performance. Apart from the glassy (α) phase, formed by simple spin-coating, PF films can also form another, so-called $\beta-$phase, if the films are treated thermally or exposed to solvent vapours[122,158,161,165]. At 77 K, the electroabsorption (EA) spectrum of the $\beta-$phase differs significantly from that of the $\alpha-$phase. Most notably, two additional sharp peaks, not present in the $\alpha-$phase, appear in the $\beta-$phase, in the narrow region around 2.8 - 2.9 eV[122]. $\beta-$phase, which has a smaller energy gap, is undesirable for PLED applications because it introduces additional energetic disorder which can stabilise polarons, and hence lead to the quenching of excitons[158].

Electroabsorption spectroscopy is a particularly useful tool for studying finished PLEDs, as it allows the probing of the Stark response of the active polymer film

buried between two electrodes[72,82]. The Stark response can provide valuable information about the general state of the polymer film and, importantly, it allows the probing of the built-in voltage, V_{BI}, generated through the equilibration of the chemical potential through the PLED heterostructure. When a voltage of the form $V = V_{dc} + V_{ac}\sin(\omega t)$ is applied across the diode, the intensity of the probing beam is modulated through the Stark effect[82], as discussed in more detail in Chapter 2, and an eletroabsorption signal, given by equation 6.1, is generated[72].

$$\Delta T/T(1\omega) \propto 2Im\{\chi^3(h\nu)\}V_{ac}(V_{dc} - V_{BI})\sin(\omega t + \theta), \tag{6.1}$$

$Im\{\chi^3(h\nu)\}$ is a function of the imaginary part of the third order dielectric susceptibility, h is Planck's constant, ν is the photon frequency, and θ is the phase of the signal with respect to the applied ac voltage. The built-in voltage can be measured by finding the dc voltage at which $\Delta T/T(1\omega)$ vanishes, which we here call the nulling voltage, or V_{null}.

In this chapter, we have employed electroabsorption spectroscopy to investigate degradation effects in ITO/PEDOT:PSS/emitting-polymer/LiF/Ca/Al light-emitting diodes, where PEDOT:PSS is poly(3,4-ethylene dioxythiophene) doped with poly(styrene sulfonate), and the emitting polymer is either poly(9,9-dioctylfluorene) (F8), poly(9,9-dioctyl-fluorene-co-bis-N,N'-(4-butyl-phenyl)-bis-N,N'-phenyl-1,4-phenylenediamine) (PFB), poly(9,9-dioctylfluorene-co-N-(4-butylphenyl)-diphenylamine) (TFB), or a blend of these three components (which we here call the tri-blend). We systematically compare the electroabsorption response and V_{null} characteristics of undriven and driven devices, and also investigate the effects of photodegradation by UV light in F8 and tri-blend devices. Our results strongly suggest the degradation of the PEDOT:PSS/emitting-polymer interface both during electrical driving and during exposure to UV light.

We also investigate the variation of the so-called excited state absorption (ESA) signal[102,103], which dominates $\Delta T/T(1\omega)$ at sub-gap energies (around 2.3 eV), with the driving time, in the F8 device. To remind the reader, the evidence presented and discussed in Chapter 4 suggests that the ESA signal is generated by the

trapped electronic charge at the PEDOT:PSS/polyfluorene interface. Interestingly, we find that there is a clear correlation between the variation of the ESA signal (measured at zero applied bias) on the one hand, and the current (I) and EL intensity (measured concurrently with ESA, but at a high forward bias) on the other hand, with the driving time. The results directly link device degradation to a specific region within the device, namely the PEDOT:PSS/F8 interface, in agreement with our other findings. The variation of the three parameters (ESA, I and EL intensity) with the driving time was also measured in the devices based on single component blends (SCBs). SCBs are state of the art blue-emitting polymers, and have very long lifetimes. They incorporate F8, TFB, PFB, and possibly other (non-disclosed) units into a single chain. In most SCB devices we have measured (all of which also contained a PEDOT:PSS layer), both the current and EL intensity increase as they are driven at a constant dc bias, in the initial few minutes. In all such cases, we found that the ESA signal increases concomitantly with I and EL, indicating that the increased performance is due to an improvement in the hole injection/transport across the PEDOT:PSS/SCB interface.

6.2 Experimental

The PLEDs used in the experiments for this chapter were provided by CDT. All of them were encapsulated, to protect from degradation by atmospheric oxygen and moisture, and they all contained an ITO/PEDOT:PSS anode. The devices based on F8, TFB, PFB and tri–blend polymers all came from the same batch, and had a LiF/Ca/Al cathode, with the layer thicknesses of 4/10/400 nm. The cathodes employed in SCB devices (which, incidentally, came from different batches) were[166]: LiF/Ca/Al (4/10/380), NaF/Al (4/200+), Ba/Ag/Al (10/68/164), BaF_2/Ca/Al (4/10/285), BaF_2/Ba/Al (4/10/305), where the numbers in the brackets indicate the thicknesses, given in nm. Each device had up to 8 pixels, and each could be investigated independently, allowing several different degradation experiments to be carried out on each device. One of the pixels in each device was driven by CDT, to half the initial luminance (L) of 100 Cd/m^2. We also measured the EL and PL

spectra of these devices, using the S2000-UV-VIS high sensitivity spectrometer.

In current-voltage-luminance (IVL) experiments (operated by the Labview software developed by the author), the current was measured using the HP34401A digital multimeter, and the relative EL intensity, detected by the Hamamatsu Photonics S1406 UV-enhanced silicon photodiode, was measured with the Keithley 199 digital multimeter. In IVL experiments where luminance characteristics were compared between undriven and driven pixels, the distance between the emitting pixel and the photodetector was always the same. Similarly, when comparing the EL intensity of a pixel before and after photodegradation, the photodetector-pixel distance, and also all the other experimental conditions, were not altered during the experiment. In photodegradation experiments, a high-power narrow-directivity Nichia UV LED (NSHU590), biased at 3.5 V, was used to degrade the pixels. The LED emission is centred at 375 nm, and has a full width at half maximum of 12 nm. It was positioned immediately next to the pixel, and the light was incident at 90^0 to the pixel surface. The surrounding pixels were protected from UV light by several layers of a thick black isolating tape.

6.3 Results

6.3.1 F8, TFB, PFB and Tri-Blend Devices Driven to Half-Life

Electroabsorption Spectra

The electroabsorption spectra of F8, TFB, PFB and tri-blend undriven and half-life driven devices are shown in Figures 6.2 and 6.3. The graphs on the left hand side show the spectra across the full energy range, from 1.7 to 3.8 eV, whereas the graphs on the right hand side are 'zoomed' in at the region between 1.7 and 2.9 eV. Near the lowest energy Stark peak (around $\sim$ 3 eV), the signal in the driven F8, TFB and PFB devices is visibly lower than in the undriven ones, by 15, 18 and 20 % respectively. In the tri-blend, the signal is reduced by only 1 %.

In the lower energy region, between 1.7 and 2.9 eV (where the signal is dominated

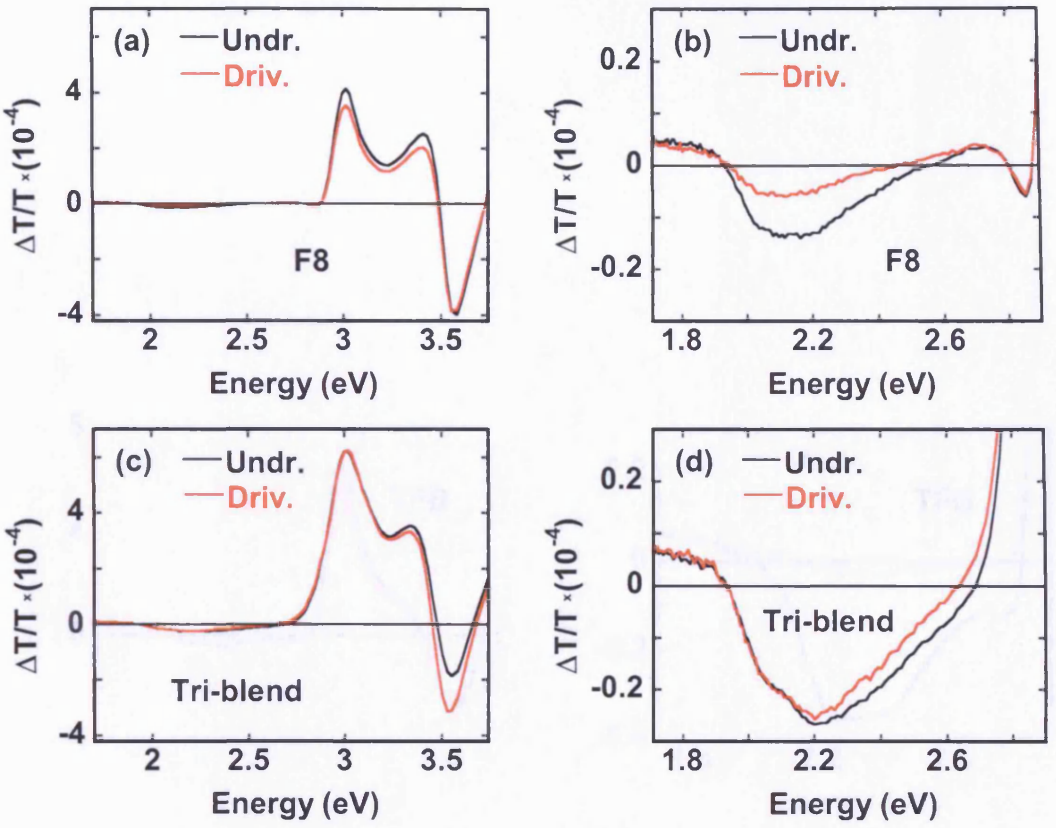

Figure 6.2: Comparison of the first harmonic $\Delta T/T$ spectra of undriven and half-life driven PLEDs, with (a)-(b) F8, (c)-(d) tri-blend polymers. The measurements were performed at $V_{dc} = 0$ V, $V_{ac} = 1$ V, and frequency $f = 2$ kHz.

by ESA), $\Delta T/T$ is drastically smaller in the driven devices, except in the tri-blend. The ESA peak is reduced by more than 90 % in TFB, and by 60 % in F8, but in both cases the peak position and shape are not significantly altered. In PFB on the other hand, there is a sizeable shift in the peak position, from 2.2 - 2.4 eV to 2.5 - 2.6 eV, and the magnitude of the response at the peak is lower by 70 %. In the tri-blend, only a relatively small reduction in $\Delta T/T$ occurs at energies above 2.2 eV, but the signal is otherwise the same.

The Nulling Voltage (V_{null}) vs Incident Photon Energy

In Figure 6.4 we compare the measured V_{null} dependence on the incident photon energy in undriven and half-life driven devices. (Note that the undriven results were already presented and discussed in Chapter 5.) In the driven F8 and TFB devices, in the energy range 2.92 to 3.11 eV, V_{null} is approximately constant, and equals 2.93

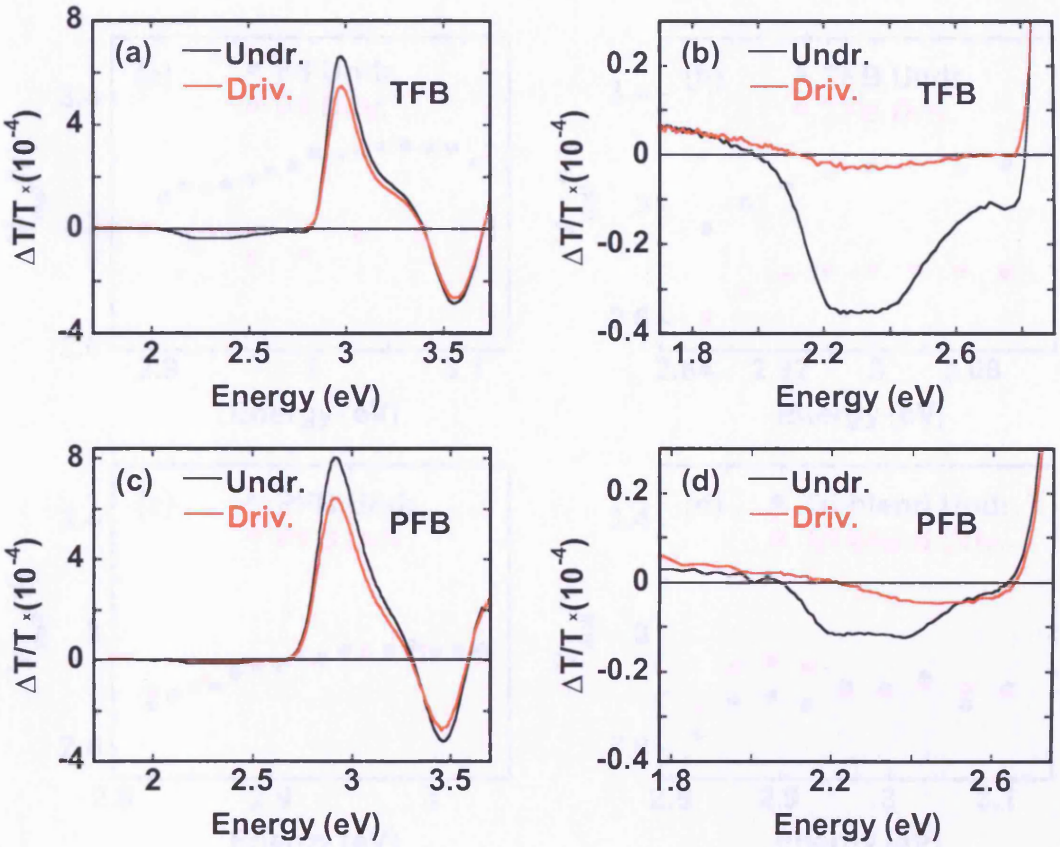

Figure 6.3: Comparison of the first harmonic $\Delta T/T$ spectra of undriven and half-life driven PLEDs, with (a)-(b) TFB, (c)-(d) PFB polymers. The measurements were carried out at $V_{dc} = 0$ V, $V_{ac} = 1$ V, and $f = 2$ kHz.

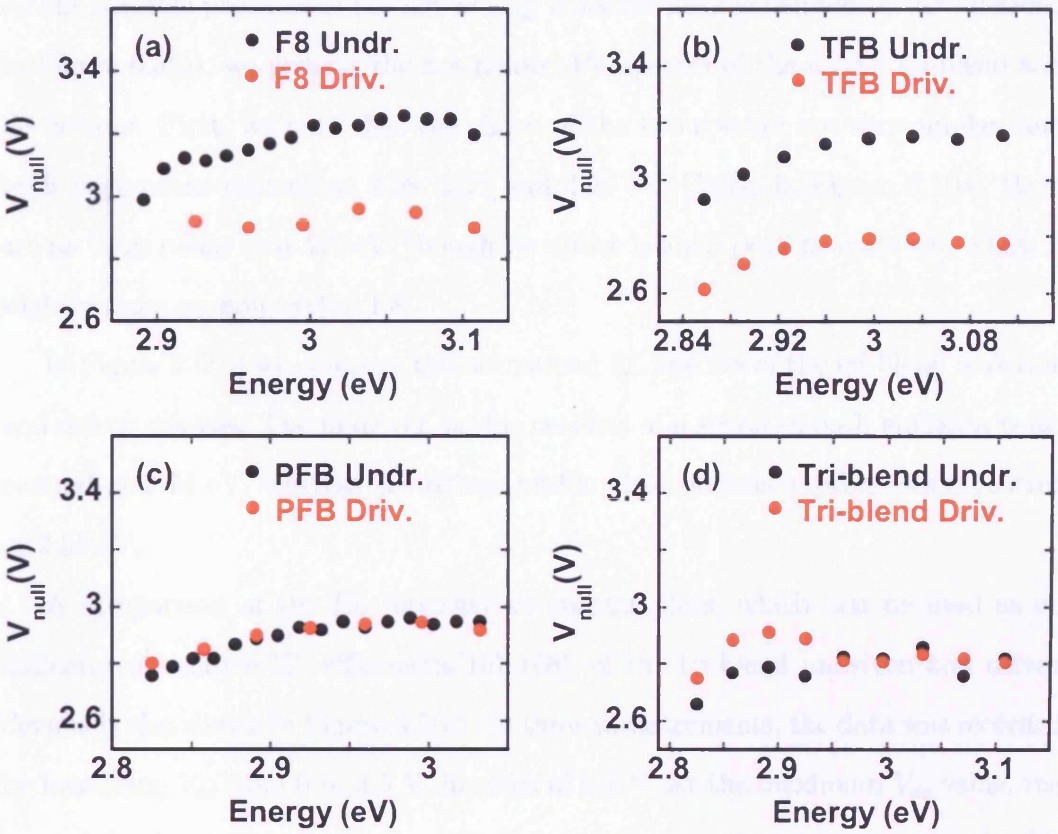

Figure 6.4: Comparison of V_{null} dependence on incident photon energy in undriven and half-life driven devices: (a) F8, (b) TFB, (c) PFB and (d) tri-blend.

$\pm$ 0.03 V and 2.75 $\pm$ 0.02 V, respectively. Interestingly, in F8, this is 0.2 - 0.3 V lower than in the undriven device, and the corresponding reduction in TFB is 0.3 - 0.4 V. In tri-blend and PFB, there is no significant V_{null} variation between undriven and driven devices.

Electroluminescence and Photoluminescence Spectra (Tri-Blend and F8)

We also measured the EL and PL spectra of the half-life driven devices, to probe for the possible presence of the low-energy emission peak generated by keto defects. In Figure 6.5(a), we present the normalised PL spectra of the driven tri-blend and F8 devices. First, we note that the shape of the two spectra are very similar, and both have peaks centred at 2.58, 2.77 and 2.95 eV. Unlike in Figure 6.1(b), there are no large peaks near 2.3 eV, though we notice a small peak near 2.4 eV, which is slightly more pronounced in F8.

In Figure 6.5(b) we compare the normalised EL spectra of the tri-blend undriven and driven devices. The undriven profile consists of a single smooth emission peak, centred at 2.74 eV, whereas the driven profile also contains another peak, centred at 2.55 eV.

A comparison of the EL intensity vs current plots, which can be used as an indicator of relative EL efficiencies[167,168], of the tri-blend undriven and driven devices is also shown in Figure 6.5(c). In these measurements, the data was recorded by increasing V_{dc} from 0 to 3.5 V, in steps of 0.1 V. At the maximum V_{dc} value, the current in the driven device is $\sim$ 70 % lower than in the undriven, and the EL intensity is lower by almost 90 %. Interestingly, the gradient in the half-life driven device is lower by 70 % as compared to the undriven one.

6.3.2 Photodegradation of Undriven Tri-Blend and F8 Devices

The changes in $\Delta T/T(1\omega)$ characteristics of undriven tri-blend and F8 devices, upon exposure to UV light for 30 hours, are shown in Figures 6.6 and 6.7 respectively. In both Figures the panel on the left hand side shows the Stark response vs dc bias,

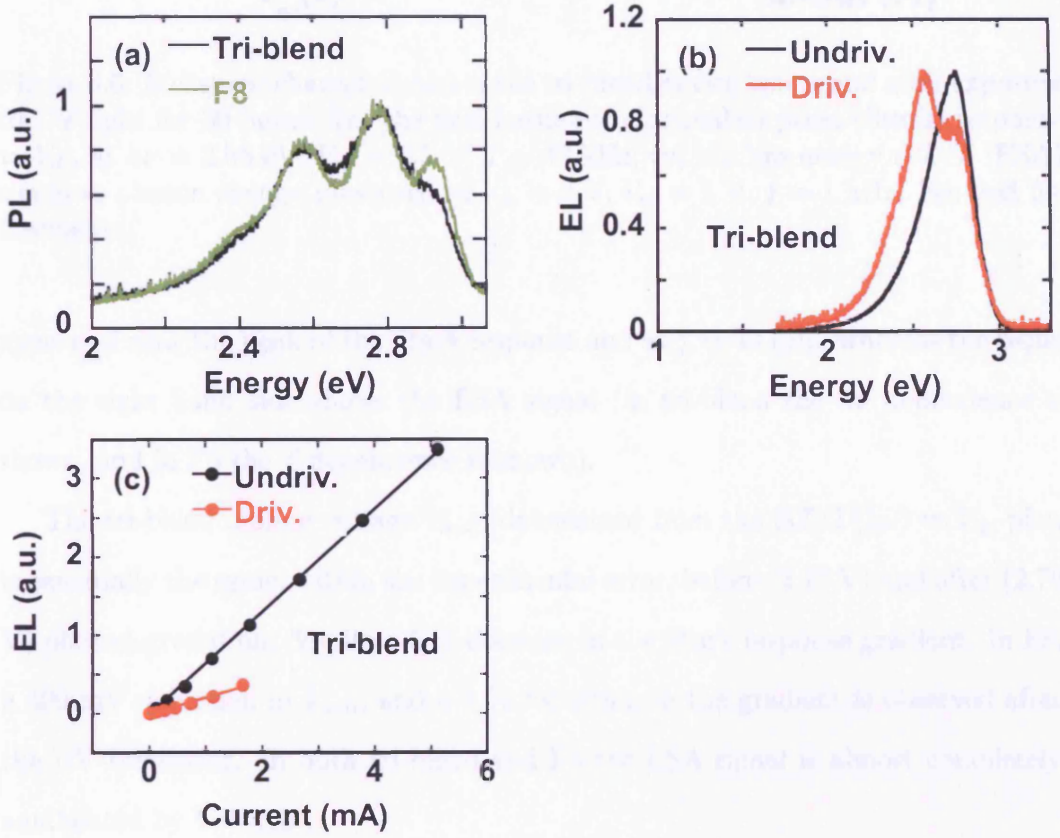

Figure 6.5: (a) Normalised PL spectra of the half-life driven tri-blend and F8 devices. (b) Normalised EL spectra of undriven and driven tri-blend devices. (c) EL vs current plots of undriven and driven tri-blend devices (both measured by increasing V_{dc} in steps of 0.1 V, from 0 to 3.5 V).

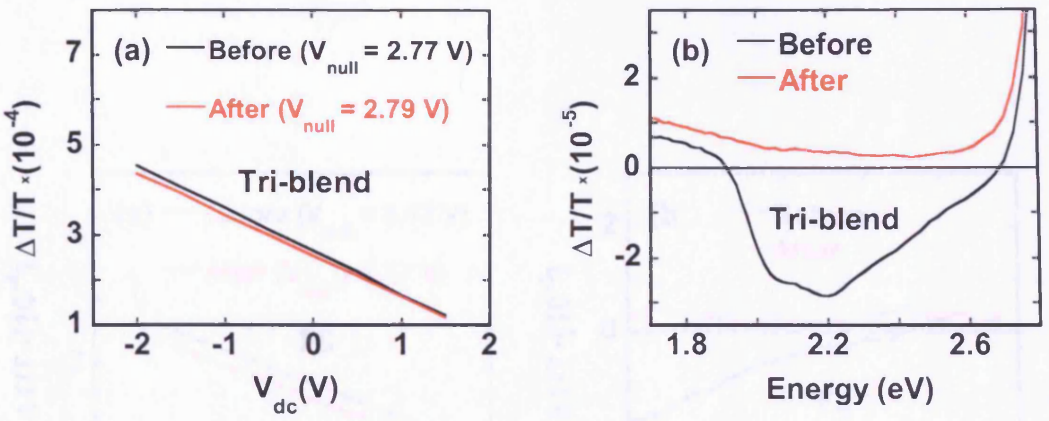

Figure 6.6: Measured characteristics of the tri-blend device before and after exposure to UV light for 30 hours: (a) the first harmonic electroabsorption (Stark) response vs V_{dc}, at $h\nu = 2.96$ eV, $V_{ac} = 0.5$ V, $f = 40$ kHz; (b) the low energy $\Delta T/T$ (ESA) signal vs photon energy, measured at $V_{dc} = 0$ V, $V_{ac} = 1$ V, $f = 1$ kHz. See text for discussion.

measured near the peak of the Stark response and at $f = 40$ kHz, whereas the panel on the right hand side shows the ESA signal (in tri-blend the $h\nu$ dependence is shown, and in F8 the f dependence is shown).

The tri-blend nulling voltage V_{null}, determined from the $\Delta T/T(1\omega)$ vs V_{dc} plot, is essentially the same, within the experimental error, before (2.77 V) and after (2.79 V) photodegradation, despite a 5 % decrease in the Stark response gradient. In F8, a 400 mV reduction in V_{null}, and a 4 % reduction in the gradient is observed after the UV treatment. In both tri-blend and F8 the ESA signal is almost completely annihilated by UV light.

6.3.3 The Variation of the Current, EL Intensity and ESA Signal with the Driving Time

F8

In F8, the measured variation of the current, EL intensity and ESA signal (measured between the driving steps, at $V_{dc} = 0$ V, and at $h\nu = 2.30$ eV) as a function of driving time (t_{dr}), is shown in Figure 6.8. The left hand panel shows the ESA signal and the current, and the right hand panel shows the EL intensity and the current. Surprisingly, both the ESA signal and the current (measured at $V_{dc} = 5.2$ V), have

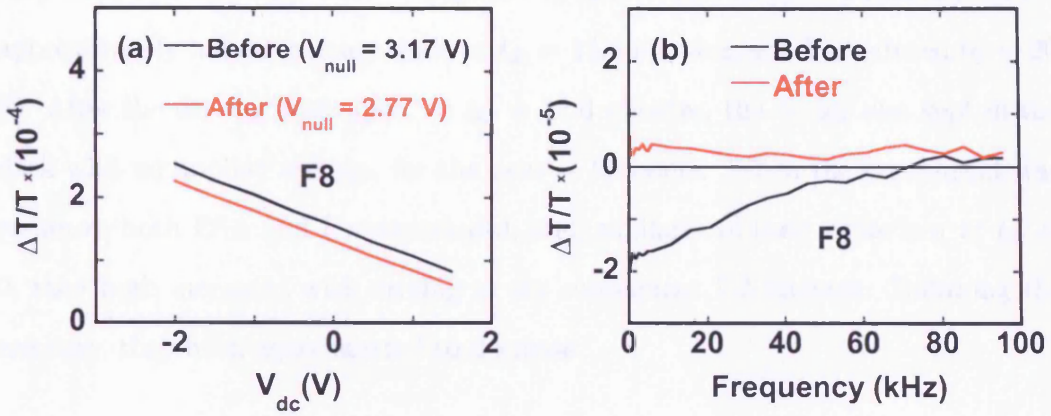

Figure 6.7: Measured characteristics of the F8 device, again before and after exposure to UV light for 30 hours: (a) the first harmonic electroabsorption (Stark) response vs V_{dc}, at $h\nu = 2.96$ eV, $V_{ac} = 0.5$ V, $f = 40$ kHz; (b) the low energy $\Delta T/T$ (ESA) signal vs frequency, measured at $h\nu = 2.14$ eV, $V_{dc} = 0$ V, $V_{ac} = 1$ V, $f = 1$ kHz.

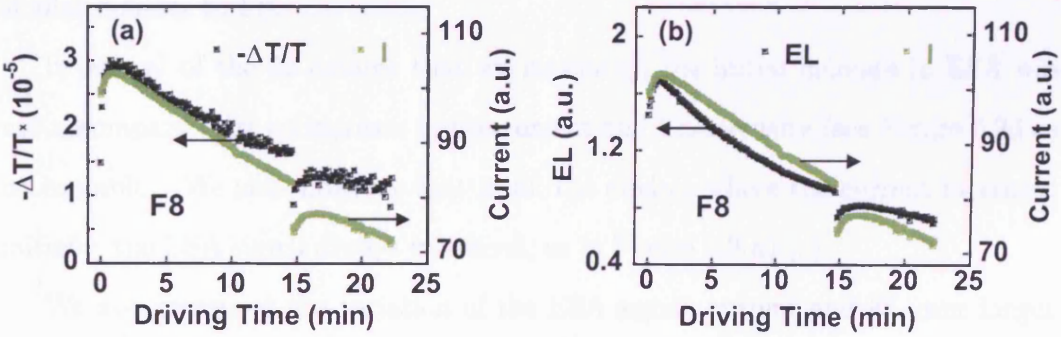

Figure 6.8: (a) ESA signal (at $h\nu = 2.30$ eV, $V_{ac} = 1$ V, $V_{dc} = 0$ V, $f = 1$ kHz) and the current as a function of driving time in F8, (b) EL and current vs driving time in F8, both measured at 5.2 V dc driving voltage.

a similar dependence on the driving time. When the device is initially switched on, both increase progressively until $t_{dr} \approx 1$ minute, and then, as the driving progresses, they both decrease with time. Compared to their values at $t_{dr} = 1$ minute, ESA is approximately halved in magnitude at $t_{dr} = 14.6$ minutes, and I is reduced by ~ 20 %. After the driving is stopped, at $t_{dr} = 14.6$ minutes, the device was kept in the dark with no applied voltage, for the next ~ 20 hours. When the experiment was resumed, both ESA and I were reduced, and, similarly to their behaviour at $t_{dr} = 0$, they both increased with driving in the subsequent 1-2 minutes. Following the recovery, they both again started to decrease.

SCB

The variation of the ESA signal, current and EL intensity with the driving time in SCB devices, was investigated with several different cathode types: NaF/Al, Ba/Ag/Al, BaF_2/Ba/Al, BaF_2/Ca/Al and LiF/Ca/Al. Figure 6.9 shows the measured variation in the first four minutes, of the ESA signal (left hand ordinate axis) and the current (right hand ordinate axis) in devices with (a) NaF/Al, (b) Ba/Ag/Al, (c) BaF_2/Ba/Al, and (d) LiF/Ca/Al cathodes. (The variation of the EL intensity was very similar to that of the current and is not shown here.) In all but the last case, the ESA signal and the current both increase with driving, in a very similar manner to F8.

In several of the 32 devices that we measured, the initial increase in ESA was not accompanied by an increase in the current and EL intensity (see Figure 6.9d as an example). We note however that in all the devices where the current increased initially, the ESA signal always increased, as in Figure 6.9(a)-(c).

We also measured the variation of the ESA signal, current and EL over longer driving periods in an SCB device (Figure 6.10). Here, BaF_2/Ca/Al was the cathode. As can be seen, all three parameters increase sharply, in a similar manner as before, and reach their maximum values in the initial few minutes of driving. Once the maximum is reached, the current and EL intensity decrease slowly with driving, whereas the ESA signal remains approximately constant. At $t_{dr} = 120$ minutes

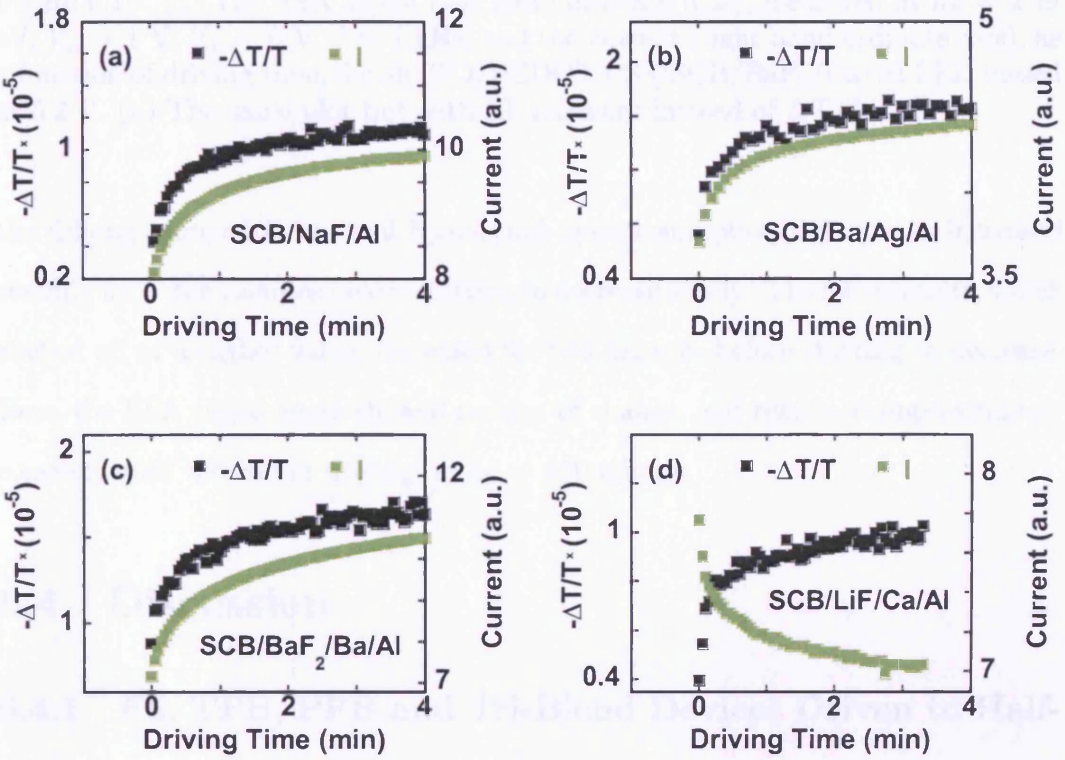

Figure 6.9: The variation of the ESA signal (left hand ordinate axis), and the current (right hand ordinate axis), with the driving time, in devices with (a) NaF/Al, (b) Ba/Ag/Al, (c) BaF_2/Ba/Al, and (d) LiF/Ca/Al cathodes. The ESA signal was measured between the driving steps, at $V_{dc} = 0$ V, $V_{ac} = 1$ V, $f = 1$ kHz and $h\nu = 2.49$ eV. All devices were driven at 4.5 V dc bias, and the current was measured at the end of each driving period. All devices had an SCB active layer.

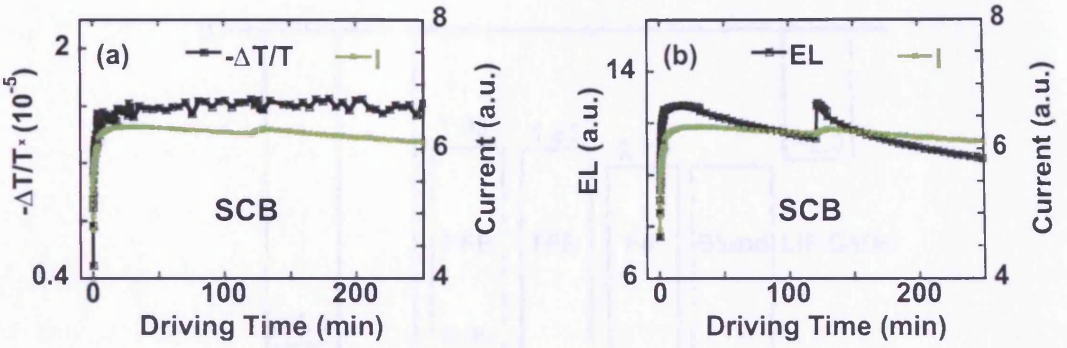

Figure 6.10: (a) The ESA signal (left hand ordinate axis), measured at $h\nu = 2.49$ eV, $V_{ac} = 1$ V, $V_{dc} = 0$ V, $f = 1$ kHz, and the current (right hand ordinate axis), as a function of driving time, for an ITO/PEDOT:PSS/SCB/BaF_2/Ca/Al LED biased at 5.2 V. (b) The same plot but with EL intensity instead of $\Delta T/T(1\omega)$.

the driving stopped for several hours, and upon resumption the current increased steadily for $\sim$ ten minutes before starting to decrease slowly. The EL intensity, which started off at a higher value, increased for two minutes before starting to decrease. Here, the ESA signal again showed no sign of change, and remained approximately constant until the end of driving, at $t_{dr} = 250$ minute.

6.4 Discussion

6.4.1 F8, TFB, PFB and Tri-Blend Devices Driven to Half-Life

One of the more notable findings here is the V_{null} decrease in F8 and TFB devices, and the absence of decrease in PFB and tri-blend devices. Since a change in V_{null} indicates a change in V_{BI}, our results indicate that the built-in voltage is reduced in the half-life driven F8 and TFB devices, but not in PFB and tri-blend devices. To explain these results, we refer to Figure 6.11 (taken from Chapter 5), which shows the relevant energy levels of the various components within the PLEDs.

We note that, if the LiF/Ca/Al work function was susceptible to degradation, so that the observed V_{null} decrease was due to an increase in the LiF/Ca/Al work function, we would expect to see a V_{BI} decrease in PFB as well as in TFB, and in tri-blend as well as in F8, contrary to the experimental findings. On the other

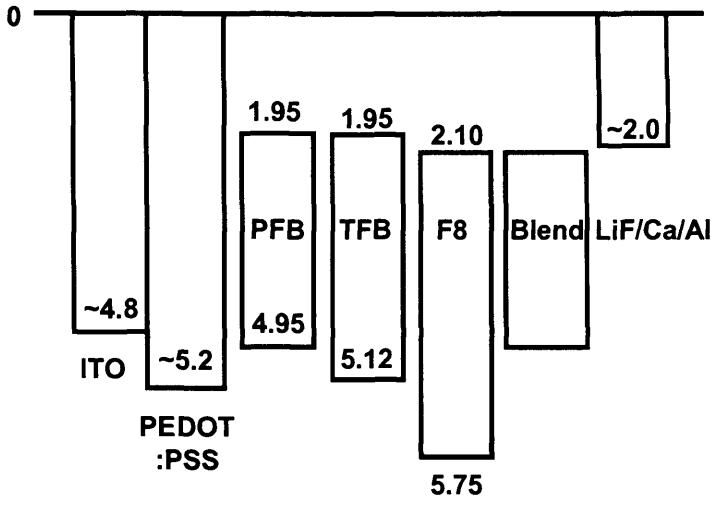

Figure 6.11: Energy levels (given in eV) of the different materials in ITO/PEDOT:PSS/polyfluorene/LiF/Ca/Al LEDs (from Chapter 5).

hand, a 0.1 - 0.3 eV reduction in the PEDOT:PSS work function would decrease F8 and TFB, but not PFB and tri-blend built-in voltage, since in the latter two the polymer HOMO level lies approximately 0.3 eV above the PEDOT:PSS work function[75,166]. The degradation of the PEDOT:PSS work function is thus fully consistent with our results.

The large reduction of the ESA signal in the region $1.8 < h\nu < 2.6$ eV also strongly indicates that PEDOT:PSS, and in particular its interface with the polymer, is degraded in half-life driven devices. We note that the ESA signal is more degraded in TFB than in F8, which could imply a larger degradation in TFB (this could also explain the larger V_{null} reduction in TFB).

From the measured V_{null} values, we estimate that the built-in voltage in F8 and TFB devices is reduced by 7 % and 11 % respectively. The reduction of the Stark response near 3 eV, in the driven F8 (15 % reduction), TFB (18 %) and PFB (20 %) devices cannot thus be explained by the degradation of the built-in field alone. The additional contributions could be the degradation of polymer chains, either in the polymer bulk or in the vicinity of the interfaces (particularly near PEDOT:PSS), and the formation of an interfacial resistive layer, observed in similar devices by Khan *et al.*[131]. Such layer can decrease the voltage drop across the active polymer layer (and thus reduce $\Delta T/T$). Interestingly, in further agreement with our

findings, Khan *et al.*[131] also reported that PEDOT:PSS work function decreases with electrical driving, probably due to chemical reactions between PEDOT:PSS and the polymer layer, or, following the findings of Kim *et al.*[130], due to de-doping of PEDOT:PSS[131].

There is other evidence which suggests that PEDOT:PSS may be susceptible to electrical degradation. For example, van der Gon *et al.*[129] showed that the passage of electrons through the PEDOT:PSS layer is likely to degrade it and release potentially damaging oxygen- and sulphur-containing moieties, which are free to move through the PLED structure. In addition, in a study of encapsulated 'hole-only' ITO/PEDOT:PSS/PFB/Al LEDs, Kim *et al.*[16] reported that the polymer near the anode interface is doped by holes, counterbalanced by anions from PEDOT:PSS. According to the authors, the charged species there develop slowly with electrical driving, and act as luminescence quenchers, and hinder hole injection across the interface.

We also note the PL/EL spectra results (Figure 6.5), which show that the measured devices are not prone to degradation by keto defects. This is in contrast to List *et al.*[158,162], who reported that keto defects in F8 are likely to be created in the presence of oxygen and electrical stressing. (Note that, apart from the atmosphere, the oxygen could also migrate, although in much smaller concentrations, from ITO[127,169] or from PEDOT:PSS[129].) Our results therefore indicate that the concentration of free oxygen in the devices is particularly small. The low energy EL emission peak in the driven tri-blend device however, centred at 2.55 eV, could be due to low-energy formations such as aggregates, which are known to provide non-radiative relaxation pathways and lower the emission efficiency[159,161]. This could also explain the decrease in EL efficiency suggested by Figure 6.5(c).

6.4.2 Photodegradation of Tri-Blend and F8 Devices

The almost complete obliteration of the ESA signal by UV light, in both tri-blend (Figure 6.6) and in F8 (Figure 6.7), indicates that the trapped electronic charge at the PEDOT:PSS/polymer interface has been removed. The concomitant V_{null}

reduction (by 0.4 V) in F8 could then be due the removal of the interface dipole, which is reportedly associated with the trapped charges[101]. Other effects, such as chemical degradation of PEDOT:PSS by UV light[132,170], could also contribute to the reduction of the effective PEDOT:PSS work function.

Our results, namely the $\sim$ 5 % reduction of the Stark $\Delta T/T$ vs V_{dc} gradient in both tri-blend and F8, also indicate the degradation of the emitting-polymer layer (possibly in the region near the PEDOT:PSS interface).

6.4.3 The Variation of the Current, EL Intensity and ESA Signal with the Driving Time

First Few Minutes of Driving

Since the ESA signal is (probably) generated by trapped electronic charge near the PEDOT:PSS/polyfluorene interface, the observed correlation between the increase in the current and the ESA signal, in the first few minutes of driving, in SCB devices with NaF/Al, Ba/Ag/Al, BaF_2/Ba/Al and BaF_2/Ca/Al cathodes, and in F8 devices with LiF/Ca/Al cathodes, indicates an improvement in charge injection/transport across the interface. Poplavskyy *et al.*[101] and van Woudenbergh *et al.*[137], who investigated F8-based LEDs with ITO/PEDOT:PSS anodes, reported a similar current increase when the devices are biased above the EL onset. In both reports, the effect was explained by electron trapping at the PEDOT:PSS/F8 interface, and (as already mentioned) the resulting generation of an interface dipole which lowers the hole injection barrier $\Phi_B(h)$. Our observation that the ESA signal, expected to be proportional to the trapped charge density[102,103], increases concomitantly with the current, thus strongly supports the trapped charge hypothesis suggested by the authors.

Although the reduction in $\Phi_B(h)$ may explain the current increase in the F8 device, where $\Phi_B(h)$ is larger than 0.5 eV, the same mechanism cannot explain the improvement in SCB devices, where the barrier is close to zero (since SCB HOMO level is comparable to that of PFB[166]). This is also supported by the results of our measurements of V_{null} and the current as a function of driving time, shown in Figure

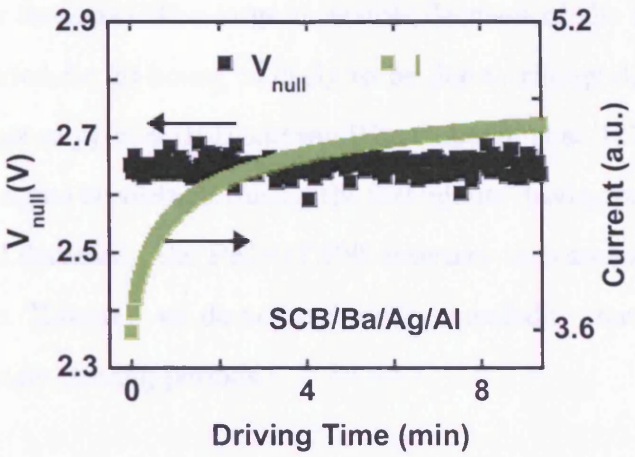

Figure 6.12: The measured variation of V_{null} and the current (at $V_{dc} = 4.5$ V) with the driving time in an ITO/PEDOT:PSS/SCB/Ba/Ag/Al device. V_{null} does not change with the driving time, indicating that the increase in the current is not due to an increase in the built-in voltage.

6.12. The plot shows that V_{null} remains constant despite an observed increase in the current. Aside from the energy barrier for hole injection, another feature of the PEDOT:PSS/emitting-polymer interface must affect its charge transport properties. In this regard, we note that X-ray and ultraviolet photoelectron spectroscopy studies have found evidence for segregation of the PSS dopant towards the PEDOT:PSS surface, and the formation of a PSSH surface layer with the thickness of a few nm[171]. Four-point probe conductivity measurements of PEDOT:PSS films have shown that, at the film surface, the conductivity is substantially lower due to the low concentration of PEDOT, the charge transporting species[172]. Thus, we speculate, similarly to Murata *et al.*[173] and Woudenbergh *et al.*[137], that when the device is first made, a thin tunnelling barrier may exist at the PEDOT:PSS surface, which impedes its hole transport properties. In this case, the current increase in SCB devices could be due to an improvement in the hole transport through this energy barrier, which is somehow brought about by the trapped interface electrons.

After the First Few Minutes

In the F8 device, the large irreversible decrease in the ESA signal during the $\sim$ 20 minute driving period that follows the initial increase (Figure 6.8), shows that the PEDOT:PSS/F8 interface is particularly vulnerable to degradation, in agreement

with our earlier findings. The large reversible decrease of the ESA signal, when the device is rested for 20 hours, is likely to be due to charge de-trapping, as also observed by Poplavskyy *et al.*[101] and van Woudenbergh *et al.*[137]. In SCB devices, where the ESA signal is constant during the 200 minute driving period (Figure 6.10) (after the initial decrease), the PEDOT:PSS interface thus seems more stable than in the F8 device. However, we do not exclude the possibility that the interface may degrade over longer driving periods.

6.5 Conclusion

In conclusion, we have investigated degradation effects in encapsulated blue light-emitting diodes that incorporate PEDOT:PSS as the hole injection layer. Apart from measuring the Stark response of the light-emitting polymer layer, which enabled us to probe the changes in the built-in voltage when the devices are driven to half-life, we also monitored the changes in the sub-gap $\Delta T/T(1\omega)$ signal (ESA), which is believed to originate from the trapped charge at the PEDOT:PSS/polymer interface. We found that, in the devices driven to half-life, V_{null} (and hence V_{BI}) is reduced by several hundreds of mVs in F8 and TFB devices, whereas the ESA signal is strongly reduced in F8, TFB and PFB devices. Such behaviour strongly points to the degradation of the PEDOT:PSS/polymer interface, and suggests a reduction of the PEDOT:PSS effective work function, which is in agreement with the evidence found in the literature[129-132,170]. In addition, the ESA signal can be almost completely annihilated by the exposure to UV light, which also results in the reduction of V_{null} in F8, presumably due to the removal of the trapped electronic charge and the associated interface dipole. The measured PL spectra of the driven devices show no large emission peaks that could be attributed to keto defects, which indicates low oxygen concentration in the active layer.

Our measurements also shed light on the nature of the observed current increase, at constant driving voltage, when the devices are initially driven for a period of a few minutes. In all such cases, we found that the ESA signal increases concomitantly with the current, suggesting that the behaviour is due to improved hole

transport/injection across the PEDOT:PSS/SCB interface. In F8 devices, where a large energy barrier exists at the PEDOT:PSS/polymer interface, Poplavskyy *et al.*[101] explained a similar improvement by the creation of an interface dipole which lowers the hole injection barrier. However, the same effect cannot explain the improvement in SCB devices, where the hole injection barrier is close to zero. We suggest that, in these devices, the improvement could be due to an enhancement in the conductivity of the low-conductivity PSS-rich surface region[137,171-173].

Lastly, we remark that the charges trapped at the PEDOT:PSS interface are likely to attract and quench excitons, and could play a part in its degradation, for example by initiating chemical and/or morphological changes.

Chapter 7

Conclusions

In this thesis, we have employed electroabsorption (EA) spectroscopy in the study of encapsulated polymer light-emitting diodes, PLEDs. In our experiments, we typically applied a voltage of the form $V = V_{dc} + V_{ac}\sin(\omega t)$ across the diode, and monitored the fractional change in the transmission, $\Delta T/T$, of an optical probe beam passing through the polymer film. In the Stark effect, as described in Chapter 2, the first harmonic $\Delta T/T(1\omega)$ signal, modulated at the frequency of the ac field, is given by

$$\Delta T/T(1\omega) \propto 2Im\{\chi^3(h\nu)\}V_{ac}(V_{dc} - V_{BI})\sin(\omega t + \theta), \tag{7.1}$$

where $Im\{\chi^3(h\nu)\}$ is a function of the imaginary part of the third order dielectric susceptibility, h is Planck's constant, ν is the photon frequency, θ is the phase of the signal with respect to the applied ac voltage, and V_{BI} is the built-in voltage. According to equation 7.1, $\Delta T/T(1\omega)$ varies linearly with V_{dc}, and passes through zero at $V_{dc} = V_{BI}$. In this thesis, since V_{null} did not always equal V_{BI} (for example in the presence of additional, non-Stark, signals), we generally referred to the dc bias at which $\Delta T/T(1\omega)$ vanishes as V_{null}.

In Chapter 3, after describing the EA experimental set-up, and the details of the measurement procedure, we tested the accuracy of the spectrometer by measuring the response of a simple one-layer PLED, in which an SCB (single component blend) emitting-polymer was sandwiched between indium tin oxide (ITO) anode, and alu-

minium cathode. Importantly, the experimental results were in full agreement with the Stark effect, which confirmed the validity of the experimental set-up, and its suitability for measuring the PLED characteristics. Also, in this device V_{null} was not found to be dependent on the incident photon energy, nor on the frequency of the applied ac voltage (as expected for $V_{null} = V_{BI}$).

In Chapter 4, we reported EA measurements of encapsulated PLEDs with the general structure ITO/PEDOT:PSS/emitting-polymer/LiF/Ca/Al, where PEDOT:PSS is poly(3,4-ethylene dioxythiophene) doped with poly(styrene sulfonate), and the emitting polymer was either poly(9,9-dioctylfluorene) (F8), poly(9,9-dioctylfluorene-co-bis-N,N'-(4-butyl-phenyl)-bis-N,N'-phenyl-1,4-phenylenediamine) (PFB), poly-(9,9-dioctylfluorene-co-N-(4-butylphenyl)-diphenylamine) (TFB), or a blend of these three polymers (tri-blend). Interestingly, in these devices the $\Delta T/T(1\omega)$ signal did not always obey equation 7.1, and there was a significant V_{null} dependence on photon energy and ac frequency. Upon investigating the frequency dependence of $\Delta T/T(1\omega)$ near the Stark peak (around 2.96 eV), it became clear that the signal is composed of at least two components. Apart from the expected Stark signal, whose magnitude is independent of frequency, we detected the presence of another signal, which, as in the report by Lane *et al.*[102], could be fitted to equation 7.2[136]. According to Lane *et al.*[102] and Brewer *et al.*[103], such a frequency dependence,

$$\Delta T/T(\omega) \propto 1/(1+\omega^2\tau^2) \tag{7.2}$$

together with other experimental and theoretical evidence, indicates that the signal is due to excited state absorption (ESA) by trapped electronic charge near the PEDOT:PSS/polymer interface[102,103]. Independently of these results, our investigations also suggest that the signal is generated near the PEDOT:PSS interface. Our current understanding is that the signal is a result of modulation of the trapped charge density at the interface, induced by a sinusoidal electric field[133].

Although at sub-gap energies (around 2.3 eV) $\Delta T/T(1\omega)$ is dominated by ESA, at energies near the Stark response peak and at high frequencies (around 50 kHz) ESA contributes only $\sim$ 1 % to the total $\Delta T/T(1\omega)$ signal. Because of this, at high

frequencies and energies around the Stark peak, V_{null} dependence on photon energy and frequency is substantially reduced, simplifying the measurement of the built-in voltage. We found that at $f = 50$ kHz, V_{null} in the tri-blend was least dependent of energy, and its V_{BI} could be estimated to within $\pm$ 0.05 V. In other devices, the dependence was not completely eliminated, but it was reduced, and V_{BI} could be estimated to within $\pm$ 0.1 V.

The measured V_{BI} values range from 2.81 V in the tri-blend and 2.94 V in PFB, to 3.10 V in TFB and 3.15 V in F8. Assuming an effective LiF/Ca/Al work function of $\sim$ 2.0 eV, which requires a 0.8 eV reduction of the effective Ca work function[148] by the LiF layer, these values are in excellent agreement with the basic theory of alignment of the chemical potential across the PLED heterostructure. Although we cannot ascertain that a LiF layer can bring about this reduction, we note that Shaheen *et al.*[151] and Brown *et al.*[150] reported that the fluoride layer decreases the Al work function by 1.8 eV and 1.2 eV respectively, which is comparable to the 0.8 eV reduction indicated by our results. Regardless of the cathode work function however, the V_{BI} variability between different polymers suggests pinning of an electrode Fermi level to a polymer bipolaron level. For example, in PFB and tri-blend devices the PEDOT:PSS Fermi level is expected to be pinned to the polymer HOMO level, which explains why their V_{BI} is smaller than in F8 and TFB devices.

In Chapter 6, electroabsorption was used to investigate degradation effects in F8, TFB, PFB and tri-blend devices with the PEDOT:PSS layer. First, we systematically compared the EA spectra and V_{null} dependence on photon energy of undriven and half-life driven devices. We found that, in the driven devices, V_{null} (and hence V_{BI}) was reduced by several hundreds of mVs in F8 and TFB, but not in PFB and tri-blend devices. Such behaviour, together with the observed large ESA reduction in the driven F8, TFB and PFB devices, strongly points to the degradation of PEDOT:PSS, and its interface with the emitting-polymer layer, in full agreement with the evidence found in the literature[129-132,170].

In the experiments involving UV photodegradation of F8 and tri-blend devices, the ESA signal could be almost completely annihilated by the exposure to UV light.

In F8, this also resulted in the reduction of V_{null}, presumably due to the removal of the trapped electronic charge and the associated interface dipole[101]. We remark that the PEDOT:PSS degradation mechanism could possibly involve the interface traps which, during operation, are repeatedly excited by the emitted light and then repopulated, and which in addition are likely to attract and quench excitons, whose energy could initiate chemical and/or morphological degradation.

We also investigated the nature of the improvement in the performance, frequently observed in many of these devices, when they are electrically driven initially for a period of a few minutes. Typically, when driven at a constant dc bias, the current (I) and electroluminescence (EL) intensity increase progressively in the first 1 - 5 minutes. Interestingly, in all such cases, we found that the ESA signal increases concomitantly with I and EL, indicating that the increase is brought about by an improvement in the hole injection/transport across the PEDOT:PSS/emitting-polymer interface. In F8 devices, where a large energy barrier exists at the PEDOT:PSS/polymer interface, Poplavskyy *et al.*[101] explained a similar improvement by the trapping of electronic charges at the PEDOT:PSS interface, and the creation of an interface dipole which lowers the hole injection barrier. However, the same effect cannot explain the improvement in SCB devices, where the hole injection barrier is expected to be close to zero[166]. In SCB devices, the effect could then be due to an improvement in the conductivity, brought about by the trapped electronic charges, of the low-conductivity PSS-rich surface region[171,172].

Appendix

A1: The Tight Binding Model of a 1-D Chain of Atoms

In this appendix we present a derivation of the electronic structure of a 1-D chain of atoms, using the tight binding model[154,174,175]. We consider a 1-D lattice of C atoms, separated by distance a from each other, each of which has a p_z orbital that can be treated as the atomic ground state. At this point, we assume that in the vicinity of each lattice point the crystal Hamiltonian can be approximated by the Hamiltonian of a single C atom (H_{at}), and that the bound levels of H_{at} are localised, so that the orbital wavefunction $\phi(x - x_n)$ is approximately zero on sites one lattice spacing away[154,174]. Here x is the spatial coordinate along the chain direction, and n identifies the site position (with n = 0, ± 1, ± 2,...., ± N′; 2N′ + 1 being equal to the number of C atoms on the chain), so that x_n equals na. Since atoms are very close together, electrons can quantum mechanically jump from state $\phi(x - x_n)$ to the same state on a nearby atom. We can write the one-electron wavefunction in Bloch form, as a linear combination of its possible states in the chain[154,174,175]:

$$\Psi_\pi(k,x) = \sum_n \exp(ik \cdot x_n)\phi(x - x_n) \tag{A1.1}$$

with k representing the electron's wavevector. To first order, the crystal Hamiltonian is

$$H = H_{at} + \Delta V(x), \tag{A1.2}$$

where $\Delta V(x)$ is the difference between the actual crystal potential and the potential of a single isolated atom. Using Schrödinger's equation, $H\Psi_\pi(k,x) = E(k)\Psi_\pi(k,x)$, we can evaluate $E(k)$. First we rewrite Schrödinger's equation using expressions A1.1 and A1.2:

$$(H_{at} + \Delta V(x)) \sum_n \exp(ik \cdot x_n)\phi(x - x_n) = E(k) \sum_n \exp(ik \cdot x_n)\phi(x - x_n),$$

and then multiply both sides by the atomic wavefunction $\phi^*(x)$, and integrate over

all x:

$$\begin{aligned} & \sum_n \exp(ik \cdot x_n) \int dx \phi^*(x) H_{at} \phi(x - x_n) \; + \\ & \sum_n \exp(ik \cdot x_n) \int dx \; \phi^*(x) \phi(x - x_n) \Delta V(x) \\ = \; & E(k) \sum_n \exp(ik \cdot x_n) \int dx \phi(x - x_n) \phi^*(x). \end{aligned} \tag{A1.3}$$

To evaluate the first term in equation A1.3, we use the expression:

$$\int \phi^*(x) H_{at} \phi(x - x_n) dx = E_{pz} \int \phi^*(x) \phi(x - x_n) dx,$$

where E_{pz} is the energy of the p_z orbital. Since $\phi(x)$ has a very short range, the integral for $n = 0$ is much larger than all other terms[154,174]. Thus, the first term becomes

$$E_{pz} \int \phi^*(x) \phi(x) dx = E_{pz},$$

where the function $\phi(x)$ is normalised. Similarly, the third term becomes equal to $E(k)$. In the second term, all the parts in the summation are zero for all values apart for $n = 0, \pm 1$, because the function $\phi(x)$ has a very short range[154,174,175]. Thus, the second term becomes:

$$\begin{aligned} & \exp(-ik \cdot a) \int dx \; \phi^*(x) \Delta V(x) \phi(x + a) + \int dx \; \phi^*(x) \Delta V(x) \phi(x) + \\ & \exp(ik \cdot a) \int dx \; \phi^*(x) \Delta V(x) \phi(x - a), \end{aligned}$$

and since the electron transfer integral $t = -\int dx \; \phi^*(x) \Delta V(x) \; \phi(x \pm a)$ is the same between any two neighbouring sites, we can write this as

$$\begin{aligned} & (e^{ik \cdot a} + e^{-ik \cdot a}) \int dx \; \phi^*(x) \Delta V(x) \phi(x + a) + \int dx \; \phi^*(x) \Delta V(x) \phi(x) \\ = \; & -2t \cos(ka) - \beta, \end{aligned} \tag{A1.4}$$

where $\beta = -\int dx\ \phi^*(x)\Delta V(x)\phi(x)$. Finally, we have[154,174,175]

$$E(k) = E_{pz} - \beta - 2t\cos(ka). \tag{A1.5}$$

The transfer integral t determines how easy it is to transfer an electron from one atom to the next; the smaller the transfer integral the harder it is to accelerate electrons. It also determines the width of the energy band (see Figure 1.5). In polyacetylene this bandwidth ($4t$) is about 10 eV[26].

A2: ΔT/T as a Sum of Stark and ESA Signals

The signal c_1'$\sin(\omega t + \theta)$ can be expanded as c_1'$\sin(\omega t)\cos(\theta) + c_1$'$\cos(\omega t)\sin(\theta)$. With the lock-in reference phase set to zero, and using the approximation $\theta \approx \tau_c\omega$, it would result in the following frequency dependence of the lock-in x- and y-channels:

$$\Delta T/T(\omega)_{x'} = c_1\text{'}\cos(\tau_c\omega) \tag{A2.1}$$

$$\Delta T/T(\omega)_{y'} = c_1\text{'}\sin(\tau_c\omega). \tag{A2.2}$$

In addition, for an excitation of the form $(1+\sin(\omega t+\theta))$, the density of the excited states $n(t)$ (that generate the ESA signal) in the steady state is expected to be given by[103,136]

$$n(t) = q + q[\sin(\omega t + \theta) - \omega\tau\cos(\omega t + \theta)]/(1 + \omega^2\tau^2), \tag{A2.3}$$

where q is a time-independent constant. Expanding sine and cosine terms yields

$$\begin{aligned} n(t) &= q + q[\sin(\omega t)\cos(\theta) + \cos(\omega t)\sin(\theta) \\ &\quad -\omega\tau\cos(\omega t)\cos(\theta) + \omega\tau\sin(\omega t)\sin(\theta)]/(1 + \omega^2\tau^2). \end{aligned} \tag{A2.4}$$

A probe beam intensity, modulated by absorption from excited states, follows the

density $n(t)$. Thus, the measurement of the modulated intensity by a lock-in amplifier (again, with the lock-in reference phase set to zero) is expected to give the following frequency dependence:

$$\Delta T/T(\omega)_{ESA\_x} = c_1[\cos(\tau_c\omega) + \omega\tau\sin(\tau_c\omega)]/(1+\omega^2\tau^2) \qquad \text{(A2.5)}$$

$$\Delta T/T(\omega)_{ESA\_y} = c_1[\sin(\tau_c\omega) - \omega\tau\cos(\tau_c\omega)]/(1+\omega^2\tau^2) \qquad \text{(A2.6)}$$

Finally, the total x-channel signal is given by the sum of equations A2.1 and A2.5,

$$\Delta T/T(\omega)x = c_1\text{'}\cos(\tau_c\omega) + c_1[\cos(\tau_c\omega) + \omega\tau\sin(\tau_c\omega)]/(1+\omega^2\tau^2) \qquad \text{(A2.7)}$$

and the total y-channel signal is given by the sum of equations A2.2 and A2.6,

$$\Delta T/T(\omega)y = c_1\text{'}\sin(\tau_c\omega) + c_1[\sin(\tau_c\omega) - \omega\tau\cos(\tau_c\omega)]/(1+\omega^2\tau^2). \qquad \text{(A2.8)}$$

A3: An Overview of PLED Degradation Mechanisms

Several distinct types of degradation are known to occur in PLEDs: (i) the decay of luminance, often accompanied by an increase in the driving voltage V[176], (ii) the appearance on non-emissive areas (dark spots)[177], and (iii) abrupt short circuit or electrical breakdown[57,178,179].

Despite the dramatic improvement in the device stability over the last fifteen years, degradation is still not very well understood. In general, the degradation mechanisms can be classified into four different categories: (1) thermally induced degradation[180], (2) electrochemically or charge-induced degradation, (3) light induced degradation, and (4) interfacial degradation[57,178,179].

(1) The first of these is related to morphological instability of amorphous polymer films. Heating of samples can cause chain aggregation or crystallisation, which in turn affect charge transport and photoluminescence (PL) efficiency[180]. One

approach to reduce quenching by crystallisation is to attach side chains, to prevent the chains from getting close to one another. Another is to increase the polymer glass transition temperature (T_g), or to dope the polymer, so as to stabilise the polymer film morphology[178,179] (the latter can also have undesirable effects, such as the formation of exciplexes which quench light emission[178]).

(2) The second mechanism arises due to electrochemical instability of polymer chains. A typical drive-current density in an organic light-emitting diode (OLED) is about 1 mA/cm^2, and in the passive matrix driving scheme[181] it can be much higher, close to 100 mA/cm^2[179]. The charges that pass through the device can cause a redox reaction in the polymer chain, and create new chemical species, especially in the presence of impurities such as oxygen and moisture, and thus affect both charge transport and the emission efficiency.

(3) The third mechanism involves photo-initiation of chemical reactions, which is particularly enhanced in the presence of impurities such as oxygen. This can be reduced by improving the light output coupling coefficient (see Chapter 1), and by reducing the amount of impurities and defects.

(4) The fourth mechanism involves the migration of impurities[183] from the electrodes into the emitting layer. The problem can be reduced by inserting a buffer layer between the electrode and the polymer. For example, at the anode, PEDOT:PSS can reduce the migration of oxygen from indium tin oxide (ITO) into the polymer[75,124,125]. If the devices are not encapsulated, migration of atmospheric oxygen and moisture can cause very fast degradation of electroluminescence.

In an interesting study by Parker *et al.*[182], involving PLEDs whose active layer consisted of a poly(phenylene vinylene) (PPV) derivative, both the decrease in luminance, and the increase in the driving voltage (in the constant-current mode), in the long term, were proportional to the total charge that passes through the device (Q), and to $\exp(-E_A/k_BT)$, where E_A is a thermal activation energy, k_B is the Boltzman constant, and T is the temperature. This indicated that the same mechanism is responsible for both the decrease in luminance and the increase in the operating voltage, and the authors suggested that it may be due to photooxidation

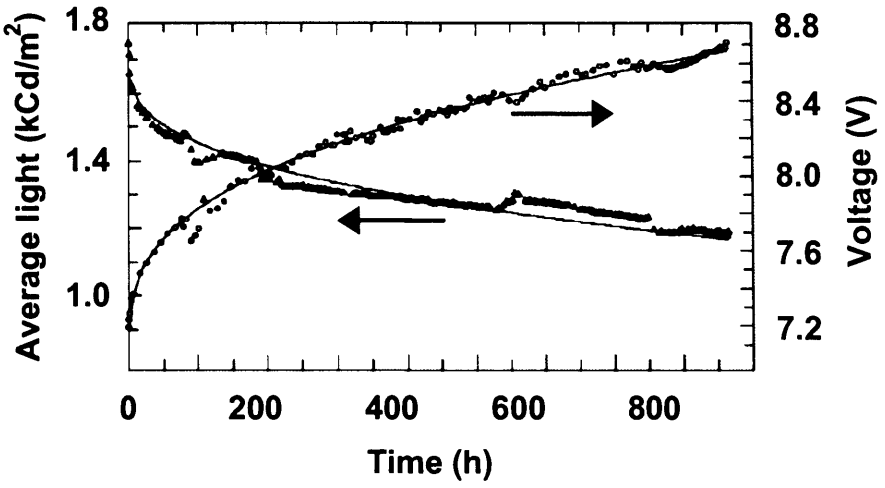

Figure 7.1: Voltage drift and degradation of luminance in a typical PLED device as a function of stressing time. (adapted from [176])

of the polymer which, in the presence of oxygen radicals, results in the formation of carbonyl groups. These can act as electron traps which reduce the electron mobility, and as efficient exciton splitting centres which reduce the EL efficiency. Silvestre *et al.*[176] also argued that the decrease in luminance and the increase in the driving voltage (e.g. see Figure 7.1) can both be explained by the same mechanism. They proposed that the energy released during non-radiative recombination (induced for example by traps), can generate more traps within the band gap of the polymer, which then decrease both the carrier mobility and PLED efficiency. In time, this leads to the increase in the operating voltage and the decrease in luminance.

Bibliography

[1] Bernius, M. T., Inbasekaran, M., O'Brien, J. & Wu, W. S. Progress with light-emitting polymers. Advanced Materials 12, 1737-1750 (2000).

[2] Friend, R. H. et al. Electroluminescence in conjugated polymers. Nature 397, 121-128 (1999).

[3] Bernanose, A., Comte, M. & Vouaux, P. Sur un nouveau mode d'émission lumineuse chez certains composes organiques. Journal De Chimie Physique Et De Physico-Chimie Biologique 50, 64-68 (1953).

[4] Pope, M., Magnante, P. & Kallmann, H. P. Electroluminescence in organic crystals. Journal of Chemical Physics 38, 2042-2043 (1963).

[5] Chiang, C. K. et al. Electrical-conductivity in doped polyacetylene. Physical Review Letters 39, 1098-1101 (1977).

[6] Partridge, R. H. Electro-luminescence from polyvinylcarbazole films.1. Carbazole Cations. Polymer 24, 733-738 (1983); Partridge, R. H. Electro-luminescence from polyvinylcarbazole films.2. Polyvinylcarbazole films containing antimony pentachloride. Polymer 24, 739-747 (1983); Partridge, R. H. Electro-luminescence from polyvinylcarbazole films.3. Electroluminescent Devices. Polymer 24, 748-754 (1983); Partridge, R. H. Electro-luminescence from polyvinylcarbazole films.4. Electro-luminescence using higher work function cathodes. Polymer 24, 755-762 (1983).

[7] Grell, M. Organic semiconductors and devices, Lecture Notes, Sheffield University.

[8] Tang, C. W. & Vanslyke, S. A. Organic electroluminescent diodes. Applied Physics Letters 51, 913-915 (1987).

[9] Burroughes, J. H. et al. Light-emitting-diodes based on conjugated polymers. Nature 347, 539-541 (1990).

[10] May, P. Polymer electronics - fact or fantasy. Physics World 8, 52-57 (1995).

[11] Bradley, D. Electroluminescent polymers: Materials, physics and device engineering. Current Opinion in Solid State & Materials Science 1, 789-797 (1996).

[12] Obtained from www.epson.co.jp (a), and www.cdtltd.co.uk (b and c).

[13] Friend, R. H. Conjugated polymers. New materials for optoelectronic devices. Pure and Applied Chemistry 73, 425-430 (2001).

[14] Prototypes have already been developed by Plastic Logic, together with E Ink. For example, visit www.plasticlogic.co.uk.

[15] Moons, E. Conjugated polymer blends: linking film morphology to performance of light emitting diodes and photodiodes. Journal of Physics-Condensed Matter 14, 12235-12260 (2002).

[16] Kim, J. S. et al. Electrical degradation of triarylamine-based light-emitting polymer diodes monitored by micro-Raman spectroscopy. Chemical Physics Letters 386, 2-7 (2004).

[17] Wu, W. S. et al. Recent development of polyfluorene-based RGB materials for light emitting diodes. Microelectronics Journal 35, 343-348 (2004).

[18] Atkins, P.,W., de Paula, J., Physical Chemistry, 7^{th} edition, Oxford University Press (2002).

[19] Atkins, P.,W., Molecular Quantum Mechanics, 2^{nd} edition, Oxford University Press, Oxford (1983).

[20] Pope, M., Swenberg, C., E., Electronic processes in organic crystals and polymers, 2^{nd} edition, Oxford University Press (1999), Chapter 1 (p.1-45), Chapters 7-9, and Chapter 15.

[21] Friend, R., Bradley, D. & Holmes, A. Polymer LEDs. Physics World 5, 42-46 (1992).

[22] Heeger, A. J., Kivelson, S., Schrieffer, J. R. & Su, W. P. Solitons in conducting polymers. Reviews of Modern Physics 60, 781-850 (1988).

[23] Su, W. P., Schrieffer, J. R. & Heeger, A. J. Solitons in polyacetylene. Physical Review Letters 42, 1698-1701 (1979).

[24] Roth, S. & Bleier, H. Solitons in polyacetylene. Advances in Physics 36, 385-462 (1987).

[25] Peierls, R., E., Quantum theory of solids, (Oxford, Clarendon Press), p. 108-112 (1955).

[26] Su, W. P., Schrieffer, J. R. & Heeger, A. J. Soliton excitations in polyacetylene. Physical Review B 22, 2099-2111 (1980).

[27] Bredas, J. L. Relationship between band-gap and bond length alternation in organic conjugated polymers. Journal of Chemical Physics 82, 3808-3811 (1985).

[28] Tabata, M., Satoh, M., Kaneto, K. & Yoshino, K. Electrochemical n-type doping of poly(para-phenylene) Film. Journal of Physics C-Solid State Physics 19, L101-L105 (1986).

[29] Fisher, A. J., Hayes, W. & Wallace, D. S. Polarons and solitons. Journal of Physics-Condensed Matter 1, 5567-5593 (1989).

[30] Wallace, D. S., Stoneham, A. M., Hayes, W., Fisher, A. J. & Testa, A. Theory of defects in conducting polymers.2. Application to polyacetylene. Journal of Physics-Condensed Matter 3, 3905-3920 (1991).

[31] Heeger, A. J. Nobel Lecture: Semiconducting and metallic polymers: The fourth generation of polymeric materials. Reviews of Modern Physics 73, 681-700 (2001).

[32] Conwell, E. M. & Wu, M. W. Contact injection into polymer light-emitting diodes. Applied Physics Letters 70, 1867-1869 (1997).

[33] We note that in some PLEDs the internal electric field may be zero in forward bias, in which case charges are driven by diffusion. For example, see Lane et al; Applied Physics Letters 83, 3611-3613 (2003).

[34] Note that hole and electron here refer to the associated polaronic particle.

[35] Fox, M. Optical properties of solids. Oxford University Press, Oxford (2001).

[36] Kohler, A. & Wilson, J. Phosphorescence and spin-dependent exciton formation in conjugated polymers. Organic Electronics 4, 179-189 (2003).

[37] Wilson, J. S. et al. Spin-dependent exciton formation in pi-conjugated compounds. Nature 413, 828-831 (2001).

[38] Kohler, A., Wilson, J. S. & Friend, R. H. Fluorescence and phosphorescence in organic materials. Advanced Engineering Materials 4, 453-459 (2002).

[39] Fukase, A., Dao, K. L. T. & Kido, J. High-efficiency organic electroluminescent devices using iridium complex emitter and arylamine-containing polymer buffer layer. Polymers For Advanced Technologies 13, 601-604 (2002).

[40] Patel, N. K., Cina, S. & Burroughes, J. H. High-efficiency organic light-emitting diodes. IEEE Journal of Selected Topics in Quantum Electronics 8, 346-361 (2002).

[41] Cao, Y., Parker, I. D., Yu, G., Zhang, C. & Heeger, A. J. Improved quantum efficiency for electroluminescence in semiconducting polymers. Nature 397, 414-417 (1999).

[42] Beljonne, D., Ye, A. J., Shuai, Z. & Bredas, J. L. Chain-length dependence of singlet and triplet exciton formation rates in organic light-emitting diodes. Advanced Functional Materials 14, 684-692 (2004).

[43] Barford, W. Theory of singlet exciton yield in light-emitting polymers. Physical Review B 70, 205204 (2004).

[44] Forrest, S. R. Exciton formation statistics under electrical injection in organic semiconductor thin films. Journal of Luminescence 110, 378-383 (2004).

[45] Baldo, M. A. et al. Highly efficient phosphorescent emission from organic electroluminescent devices. Nature 395, 151-154 (1998).

[46] Cleave, V., Yahioglu, G., Le Barny, P., Friend, R. H. & Tessler, N. Harvesting singlet and triplet energy in polymer LEDs. Advanced Materials 11, 285-288 (1999).

[47] Cleave, V. et al. Transfer processes in semiconducting polymer-porphyrin blends. Advanced Materials 13, 44-47 (2001).

[48] Higgins, R. W. T., Monkman, A. P., Nothofer, H. G. & Scherf, U. Energy transfer to porphyrin derivative dopants in polymer light-emitting diodes. Journal of Applied Physics 91, 99-105 (2001).

[49] Adachi, C., Baldo, M. A., Thompson, M. E. & Forrest, S. R. Nearly 100 % internal phosphorescence efficiency in an organic light-emitting device. Journal of Applied Physics 90, 5048-5051 (2001).

[50] Tsutsui, T., Yahiro, M., Yokogawa, H. & Kawano, K. Doubling coupling-out efficiency in organic light-emitting devices using a thin silica aerogel layer. Advanced Materials 13, 1149-1152 (2001).

[51] Windisch, R. et al. Light-emitting diodes with 31 % external quantum efficiency by outcoupling of lateral waveguide modes. Applied Physics Letters 74, 2256-2258 (1999).

[52] Yamasaki, T., Sumioka, K. & Tsutsui, T. Organic light-emitting device with an ordered monolayer of silica microspheres as a scattering medium. Applied Physics Letters 76, 1243-1245 (2000).

[53] Nakamura, T., Tsutsumi, N., Juni, N. & Fujii, H. Improvement of coupling-out efficiency in organic electroluminescent devices by addition of a diffusive layer. Journal of Applied Physics 96, 6016-6022 (2004).

[54] Sze, S. M. Physics of semiconductor devices (2^{nd} edition), Wiley, New York (1981).

[55] Brown, T. M., Electroabsorption investigations of polymer light-emitting diodes with efficient electrodes, PhD Thesis, Cambridge (2001).

[56] Davids, P. S., Campbell, I. H. & Smith, D. L. Device model for single carrier organic diodes. Journal of Applied Physics 82, 6319-6325 (1997).

[57] Shinar, J. (editor), Organic light-emitting devices (Ch. 1) , AIP Press (2004).

[58] Scott, J. C. Metal-organic interface and charge injection in organic electronic devices. Journal of Vacuum Science & Technology A 21, 521-531 (2003).

[59] Braun, D. Electronic injection and conduction processes for polymer devices. Journal of Polymer Science Part B-Polymer Physics 41, 2622-2629 (2003).

[60] Parker, I. D. Carrier tunneling and device characteristics in polymer light-emitting-diodes. Journal of Applied Physics 75, 1656-1666 (1994).

[61] Davids, P. S., Kogan, S. M., Parker, I. D. & Smith, D. L. Charge injection in organic light-emitting diodes: Tunneling into low mobility materials. Applied Physics Letters 69, 2270-2272 (1996).

[62] Arkhipov, V. I., Emelianova, E. V., Tak, Y. H. & Bassler, H. Charge injection into light-emitting diodes: Theory and experiment. Journal of Applied Physics 84, 848-856 (1998).

[63] Wolf, U., Arkhipov, V. I. & Bassler, H. Current injection from a metal to a disordered hopping system. I. Monte Carlo simulation. Physical Review B 59, 7507-7513 (1999).

[64] Barth, S. et al. Current injection from a metal to a disordered hopping system. III. Comparison between experiment and Monte Carlo simulation. Physical Review B 60, 8791-8797 (1999).

[65] Abkowitz, M. A. & Mizes, H. A. Emission limited injection by thermally assisted tunneling into a trap-free transport polymer. Applied Physics Letters 66, 1288-1290 (1995).

[66] van Woudenbergh, T., Blom, P. W. M., Vissenberg, M. & Huiberts, J. N. Temperature dependence of the charge injection in poly- dialkoxy-p-phenylene vinylene. Applied Physics Letters 79, 1697-1699 (2001).

[67] Hoofman, R., de Haas, M. P., Siebbeles, L. D. A. & Warman, J. M. Highly mobile electrons and holes on isolated chains of the semiconducting polymer poly(phenylenevinylene). Nature 392, 54-56 (1998).

[68] Blom, P. W. M., deJong, M. J. M. & Vleggaar, J. J. M. Electron and hole transport in poly(p-phenylene vinylene) devices. Applied Physics Letters 68, 3308-3310 (1996).

[69] Stoneham, A. M. et al. Understanding electron flow in conducting polymer films: injection, mobility, recombination and mesostructure. Journal of Physics-Condensed Matter 14, 9877-9898 (2002).

[70] Campbell, I. H., Davids, P. S., Smith, D. L., Barashkov, N. N. & Ferraris, J. P. The Schottky energy barrier dependence of charge injection in organic light-emitting diodes. Applied Physics Letters 72, 1863-1865 (1998).

[71] Campbell, A. J., Bradley, D. D. C. & Lidzey, D. G. Space-charge limited conduction with traps in poly(phenylene vinylene) light emitting diodes. Journal of Applied Physics 82, 6326-6342 (1997).

[72] Campbell, I. H., Hagler, T. W., Smith, D. L. & Ferraris, J. P. Direct measurement of conjugated polymer electronic excitation energies using metal/polymer/metal structures. Physical Review Letters 76, 1900-1903 (1996).

[73] Campbell, I. H. et al. Controlling charge injection in organic electronic devices using self-assembled monolayers. Applied Physics Letters 71, 3528-3530 (1997).

[74] Heller, C. M. & Campbell, I. H. Chemical potential pinning due to equilibrium electron transfer at metal/C-60-doped polymer interfaces. Journal of Applied Physics 81, 3227-3231 (1997).

[75] Brown, T. M. et al. Built-in field electroabsorption spectroscopy of polymer light- emitting diodes incorporating a doped poly(3,4-ethylene dioxythiophene) hole injection layer. Applied Physics Letters 75, 1679-1681 (1999).

[76] Brown, T. M. & Cacialli, F. Contact optimization in polymer light-emitting diodes. Journal of Polymer Science Part B-Polymer Physics 41, 2649-2664 (2003).

[77] Davids, P. S., Saxena, A. & Smith, D. L. Nondegenerate continuum model for polymer light-emitting-diodes. Journal of Applied Physics 78, 4244-4252 (1995).

[78] Campbell, I. H., Smith, D. L. & Ferraris, J. P. Electrical-impedance measurements of polymer light-emitting-diodes. Applied Physics Letters 66, 3030-3032 (1995).

[79] Aspnes, D. E. & Rowe, J. E. Resonant nonlinear optical susceptibility - electroreflectance in low-field limit. Physical Review B 5, 4022-4030 (1972).

[80] Edited by Wilardson, R. K., and Beer, A. C., Semiconductors and semimetals, Volume 9, Modulation techniques, Academic Press, New York (1972).

[81] Sebastian, L. & Weiser, G. Electric-field modulated spectra of polydiacetylene single-crystal. Chemical Physics Letters 64, 396-400 (1979).

[82] Sebastian, L., Weiser, G. & Bassler, H. Charge-transfer transitions in solid tetracene and pentacene studied by electro-absorption. Chemical Physics 61, 125-135 (1981).

[83] Phillips, S. D. et al. Electroabsorption of polyacetylene. Physical Review B 40, 9751-9759 (1989).

[84] Liess, M. et al. Electroabsorption spectroscopy of luminescent and nonluminescent pi-conjugated polymers. Physical Review B 56, 15712-15724 (1997).

[85] Horvath, A., Bassler, H. & Weiser, G. Electroabsorption in conjugated polymers. Physica Status Solidi B-Basic Research 173, 755-764 (1992).

[86] Campbell, I. H., Joswick, M. D. & Parker, I. D. Direct measurement of the internal electric-field distribution in a multilayer organic light-emitting diode. Applied Physics Letters 67, 3171-3173 (1995).

[87] Campbell, I. H. et al. Probing electronic state charging in organic electronic devices using electroabsorption spectroscopy. Synthetic Metals 80, 105-110 (1996).

[88] Bransden, B. H., Joachain, C. J., Physics of atoms and molecules (2^{nd} edition), Prentice Hall (2003).

[89] Horvath, A., Weiser, G., Baker, G. L. & Etemad, S. Influence of disorder on the field-modulated spectra of polydiacetylene films. Physical Review B 51, 2751-2758 (1995).

[90] Harrison, M. G. et al. Electro-optical studies of a soluble conjugated polymer with particularly low intrachain disorder. Physical Review B 60, 8650-8658 (1999).

[91] Bublitz, G. U. & Boxer, S. G. Stark spectroscopy: Applications in chemistry, biology, and materials science. Annual Review of Physical Chemistry 48, 213-242 (1997).

[92] Weiser, G. Stark-effect of one-dimensional Wannier excitons in polydiacetylene single-crystals. Physical Review B 45, 14076-14085 (1992).

[93] Horvath, A., Weiser, G., LapersonneMeyer, C., Schott, M. & Spagnoli, S. Wannier excitons and Franz-Keldysh effect of polydiacetylene chains diluted in their single crystal monomer matrix. Physical Review B 53, 13507-13514 (1996).

[94] Weiser, G. & Horvath, A. Variation with disorder of absorption and electroabsorption spectra of a pi-conjugated polymer: 4BCMU. Chemical Physics 227, 153-166 (1998).

[95] Rohlfing, F., Investigations of the non-linear Stark effect in conjugated molecular materials, PhD Thesis, Sheffield (1997).

[96] Campbell, I. H. et al. Controlling Schottky energy barriers in organic electronic devices using self-assembled monolayers. Physical Review B 54, 14321-14324 (1996).

[97] Hung, L. S., Tang, C. W. & Mason, M. G. Enhanced electron injection in organic electroluminescence devices using an Al/LiF electrode. Applied Physics Letters 70, 152-154 (1997).

[98] Brown, T. M. et al. LiF/Al cathodes and the effect of LiF thickness on the device characteristics and built-in potential of polymer light- emitting diodes. Applied Physics Letters 77, 3096-3098 (2000).

[99] Brown, T. M. et al. Efficient electron injection in blue-emitting polymer light-emitting diodes with LiF/Ca/Al cathodes. Applied Physics Letters 79, 174-176 (2001).

[100] Brown, T. M. et al. Electronic line-up in light-emitting diodes with alkali-halide/metal cathodes. Journal of Applied Physics 93, 6159-6172 (2003).

[101] Poplavskyy, D., Nelson, J. & Bradley, D. D. C. Ohmic hole injection in poly(9,9-dioctylfluorene) polymer light-emitting diodes. Applied Physics Letters 83, 707-709 (2003).

[102] Lane, P. A., deMello, J. C., Fletcher, R. B. & Bernius, M. Electric field screening in polymer light-emitting diodes. Applied Physics Letters 83, 3611-3613 (2003).

[103] Brewer, P. J., Lane, P. A., deMello, A. J., Bradley, D. D. C. & deMello, J. C. Internal field screening in polymer light-emitting diodes. Advanced Functional Materials 14, 562-570 (2004).

[104] van Woudenbergh, T., Blom, P. W. M. & Huiberts, J. N. Electro-optical properties of a polymer light-emitting diode with an injection-limited hole contact. Applied Physics Letters 82, 985-987 (2003).

[105] Pei, Q. B., Yu, G., Zhang, C., Yang, Y. & Heeger, A. J. Polymer light-emitting electrochemical-cells. Science 269, 1086-1088 (1995).

[106] Pei, Q. B., Yang, Y., Yu, G., Zhang, C. & Heeger, A. J. Polymer light-emitting electrochemical cells: In situ formation of a light-emitting p-n junction. Journal of the American Chemical Society 118, 3922-3929 (1996).

[107] deMello, J. C., Tessler, N., Graham, S. C. & Friend, R. H. Ionic space-charge effects in polymer light-emitting diodes. Physical Review B 57, 12951-12963 (1998).

[108] deMello, J. C., Halls, J. J. M., Graham, S. C., Tessler, N. & Friend, R. H. Electric field distribution in polymer light-emitting electrochemical cells. Physical Review Letters 85, 421-424 (2000).

[109] Gao, J., Heeger, A. J., Campbell, I. H. & Smith, D. L. Direct observation of junction formation in polymer light- emitting electrochemical cells. Physical Review B 59, R2482-R2485 (1999).

[110] Pei, Q. B. & Yang, Y. Solid-state polymer light-emitting electrochemical cells. Synthetic Metals 80, 131-136 (1996).

[111] Gao, J. & Dane, J. Visualization of electrochemical doping and light-emitting junction formation in conjugated polymer films. Applied Physics Letters 84, 2778-2780 (2004).

[112] Giebeler, C. et al. Optical studies of electric fields in poly(2-methoxy-5-ethyl(2(')-hexyloxy) para-phenylene vinylene) light-emitting diodes. Applied Physics Letters 74, 3714-3716 (1999).

[113] Giebeler, C., Whitelegg, S. A., Lidzey, D. G., Lane, P. A. & Bradley, D. D. C. Device degradation of polymer light emitting diodes studied by electroabsorption measurements. Applied Physics Letters 75, 2144-2146 (1999).

[114] Yoon, J., Kim, J. J., Lee, T. W. & Park, O. O. Evidence of band bending observed by electroabsorption studies in polymer light emitting device with ionomer/Al or LiF/Al cathode. Applied Physics Letters 76, 2152-2154 (2000).

[115] Michelotti, F., Bussi, S., Dominici, L., Bertolotti, M. & Bao, Z. Space charge effects in polymer-based light-emitting diodes studied by means of a polarization sensitive electroreflectance technique. Journal of Applied Physics 91, 5521-5532 (2002).

[116] Liess, M. et al. Charge injection into OLED's during operation studied by electroabsorption screening. Synthetic Metals 102, 1075-1076 (1999).

[117] Operating instructions, Xe 900, 450W Xenon Arc lamp, Issue 2, Edinburgh Instruments, UK (June 2000).

[118] Data sheet, Bentham M300, Bentham Instruments Limited , England, UK (downloaded from www.bentham.co.uk/pdf/M300.pdf).

[119] Silicon photodiodes with built-in op Amp S1406 Series, Technical data, Hamamatsu Photonics, Japan.

[120] Comar 435 IK Data sheet, Comar Instruments, Cambridge, UK.

[121] SR830 Lock-in amplifier, Operating manual and programming reference.

[122] Cadby, A. J. et al. Film morphology and photophysics of polyfluorene. Physical Review B 62, 15604-15609 (2000).

[123] Millman, J. Microelectronics: Digital and analog circuits and systems. McGraw-Hill, New York (1979).

[124] Karg, S., Scott, J. C., Salem, J. R. & Angelopoulos, M. Increased brightness and lifetime of polymer light-emitting diodes with polyaniline anodes. Synthetic Metals 80, 111-117 (1996).

[125] Carter, J. C. et al. Operating stability of light-emitting polymer diodes based on poly(p-phenylene vinylene). Applied Physics Letters 71, 34-36 (1997).

[126] Mason, M. G. et al. Interfacial chemistry of Alq(3) and LiF with reactive metals. Journal of Applied Physics 89, 2756-2765 (2001).

[127] de Jong, M. P., van Ijzendoorn, L. J. & de Voigt, M. J. A. Stability of the interface between indium-tin-oxide and poly(3,4-ethylenedioxythiophene)/poly(styrenesulfonate) in polymer light-emitting diodes. Applied Physics Letters 77, 2255-2257 (2000).

[128] Hung, L. S., Tang, C. W., Mason, M. G., Raychaudhuri, P. & Madathil, J. Application of an ultrathin LiF/Al bilayer in organic surface- emitting diodes. Applied Physics Letters 78, 544-546 (2001).

[129] van der Gon, A. W. D., Birgerson, J., Fahlman, M. & Salaneck, W. R. Modification of PEDOT-PSS by low-energy electrons. Organic Electronics 3, 111-118 (2002).

[130] Kim, J. S., Ho, P. K. H., Murphy, C. E., Baynes, N. & Friend, R. H. Nature of non-emissive black spots in polymer light-emitting diodes by in-situ micro-Raman spectroscopy. Advanced Materials 14, 206-209 (2002).

[131] Khan, R. U. A., Bradley, D. D. C., Webster, M. A., Auld, J. L. & Walker, A. B. Degradation in blue-emitting conjugated polymer diodes due to loss of ohmic hole injection. Applied Physics Letters 84, 921-923 (2004).

[132] Crispin, X. et al. Conductivity, morphology, interfacial chemistry, and stability of poly(3,4-ethylene dioxythiophene)-poly(styrene sulfonate): A photoelectron spectroscopy study. Journal of Polymer Science Part B-Polymer Physics 41, 2561-2583 (2003).

[133] Personal communication from J.C. deMello.

[134] Kim, J. S. et al. Indium-tin oxide treatments for single- and double-layer polymeric light-emitting diodes: The relation between the anode physical, chemical, and morphological properties and the device performance. Journal of Applied Physics 84, 6859-6870 (1998).

[135] The Pearson's coefficient R (least squares curve fit) is given by the following relation: $R = \sum_i (f_i - f_m)(y_i - y_m)/[\sqrt{\sum_i (f_i - f_m)^2}][\sqrt{\sum_i (y_i - y_m)^2}]$, where y_i is the actual value, y_m is the mean of actual values, f_i is the calculated y fit value, f_m is the mean of calculated y fit values. (from the KaleidaGraph Guide to Curve Fitting)

[136] Botta, C., Luzzati, S., Tubino, R., Bradley, D. D. C. & Friend, R. H. Photoinduced absorption of polymer-solutions. Physical Review B 48, 14809-14817 (1993).

[137] T. van Woudenbergh, J. Wildeman, P. W. M. Blom, J. Bastiaansen, and B. M. W. Langeveld-Voss, Advanced Functional Materials 14, 677-683 (2004).

[138] Grice, A. W. et al. High brightness and efficiency blue light-emitting polymer diodes. Applied Physics Letters 73, 629-631 (1998).

[139] Palilis, L. C. et al. Bright and efficient blue and green light-emitting diodes based on conjugated polymer blends. Synthetic Metals 111, 159-163 (2000).

[140] Generally, depending on the active layer, the Stark signal at the peak was 20 to 60 times higher than the trapped charge signal at its peak.

[141] Here, the Stark response equals $\sim 8\times10^{-4}$ whereas the trapped charge signal equals $\sim 0.1\times10^{-4}$.

[142] Noel, M., Vasu, K. I. Cyclic voltammetry and the frontiers of electrochemistry (Chapter 2). London (1990).

[143] Oldham, K.B., Myland, J.C. Fundamentals of electrochemical science (Chapter 6). Academic Press, San Diego (1994).

[144] Janietz, S. et al. Electrochemical determination of the ionization potential and electron affinity of poly(9,9-dioctylfluorene). Applied Physics Letters 73, 2453-2455 (1998).

[145] Mo, H., Pochapsky, T. C. Self-diffusion coefficients of paired ions. The Journal of Chemistry 101, 4485-4486 (1996).

[146] Brett, C. M. A., Brett, A. M. O., Electrochemistry (Chapters 1-4), Oxford University Press (1993).

[147] Note that the measured polymers, purchased from ADS, do not come from the same batch as the polymers used to make PLEDs, and therefore do not have exactly the same HOMO (and LUMO) levels.

[148] Michaelson, H. B. Work function of elements and its periodicity. Journal of Applied Physics 48, 4729-4733 (1977).

[149] We do not know the full extent of W_F decrease since the author did not provide the polymer LUMO data.

[150] Brown, T. M. et al. The influence of LiF thickness on the built-in potential of blue polymer light-emitting diodes with LiF/Al cathodes. Synthetic Metals 124, 15-17 (2001).

[151] Shaheen, S. E. et al. Bright blue organic light-emitting diode with improved color purity using a LiF/Al cathode. Journal of Applied Physics 84, 2324-2327 (1998).

[152] Schlaf, R. et al. Photoemission spectroscopy of LiF coated Al and Pt electrodes. Journal of Applied Physics 84, 6729-6736 (1998).

[153] Le, Q. T. et al. Photoemission study of aluminum/tris-(8-hydroxyquinoline) aluminum and aluminum/LiF/tris-(8-hydroxyquinoline) aluminum interfaces. Journal of Applied Physics 87, 375-379 (2000).

[154] Ashcroft, N., W., Mermin, N.,D., Solid state phyics, Philadelphia (1976).

[155] Greczynski, G., Fahlman, M. & Salaneck, W. R. An experimental study of poly(9,9-dioctyl-fluorene) and its interfaces with Li, Al, and LiF. Journal of Chemical Physics 113, 2407-2412 (2000).

[156] Personal communication from Dr. M. Roberts of CDT.

[157] Reported on www.cdtltd.co.uk, 23 May 2005.

[158] Scherf, U. & List, E. J. W. Semiconducting polyfluorenes - Towards reliable structure- property relationships. Advanced Materials 14, 477-487 (2002).

[159] Bliznyuk, V. N. et al. Electrical and photoinduced degradation of polyfluorene based films and light-emitting devices. Macromolecules 32, 361-369 (1999).

[160] Lemmer, U. et al. Aggregate fluorescence in conjugated Polymers. Chemical Physics Letters 240, 373-378 (1995).

[161] Grell, M., Bradley, D. D. C., Ungar, G., Hill, J. & Whitehead, K. S. Interplay of physical structure and photophysics for a liquid crystalline polyfluorene. Macromolecules 32, 5810-5817 (1999).

[162] List, E. J. W., Guentner, R., de Freitas, P. S. & Scherf, U. The effect of keto defect sites on the emission properties of polyfluorene-type materials. Advanced Materials 14, 374-378 (2002).

[163] Gong, X. O. et al. Stabilized blue emission from polyfluorene-based light-emitting diodes: Elimination of fluorenone defects. Advanced Functional Materials 13, 325-330 (2003).

[164] Incidentally, List *et al.* (see ref. [162]) suggested that the amount of monoalkylated impurities could account for the observed batch-to-batch differences in PL efficiency and EL lifetime.

[165] Ariu, M. et al. The effect of morphology on the temperature-dependent photoluminescence quantum efficiency of the conjugated polymer poly(9, 9-dioctylfluorene). Journal of Physics-Condensed Matter 14, 9975-9986 (2002).

[166] Data provided by CDT (courtesy of Dr. Matthew Roberts).

[167] Tada, K. & Onoda, M. Photoirradiation effects on light-emitting devices based on poly (p-phenylene vinylene) derivative. Ieice Transactions on Electronics E85C, 1227-1232 (2002).

[168] Tada, K. & Onoda, M. Photoirradiation effects on polymer light-emitting devices based on poly(3-alkylthiophene). Journal of Physics D-Applied Physics 35, 192-195 (2002).

[169] Scott, J. C. et al. Degradation and failure of MEH-PPV light-emitting diodes. Journal of Applied Physics 79, 2745-2751 (1996).

[170] Marciniak, S. et al. Light induced damage in poly(3,4-ethylenedioxythiophene) and its derivatives studied by photoelectron spectroscopy. Synthetic Metals 141, 67-73 (2004).

[171] Greczynski, G., Kugler, T. & Salaneck, W. R. Characterization of the PEDOT-PSS system by means of X-ray and ultraviolet photoelectron spectroscopy. Thin Solid Films 354, 129-135 (1999).

[172] Jonsson, S. K. M. et al. The effects of solvents on the morphology and sheet resistance in poly (3,4-ethylenedioxythiophene)-polystyrenesulfonic acid (PEDOT-PSS) films. Synthetic Metals 139, 1-10 (2003).

[173] Murata, K., Cina, S. & Greenham, N. C. Barriers to electron extraction in polymer light-emitting diodes. Applied Physics Letters 79, 1193-1195 (2001).

[174] J. Singleton. Chapter 4. Band theory and electronic properties of solids. Oxford University Press, Oxford (2001).

[175] Hook, J.,R., Hall, H.,E., Solid state physics, 2^{nd} edition, Manchester (1991).

[176] Silvestre, G. C. M., Johnson, M. T., Giraldo, A. & Shannon, J. M. Light degradation and voltage drift in polymer light-emitting diodes. Applied Physics Letters 78, 1619-1621 (2001).

[177] Savvateev, V. N. et al. Degradation of nonencapsulated polymer-based light-emitting diodes: Noise and morphology. Applied Physics Letters 71, 3344-3346 (1997).

[178] Nalwa, H.,S. (editor), Handbook of advanced electronic and photonic materials and devices (Ch. 1), Volume 10, Academic Press (2001).

[179] Mueller, G. (editor), Semiconductors and semimetals 64, Electroluminescence 1, Academic Press, San Diego (2000).

[180] Tessler, N., Harrison, N. T., Thomas, D. S. & Friend, R. H. Current heating in polymer light emitting diodes. Applied Physics Letters 73, 732-734 (1998).

[181] In passive matrix operation a pixel is activated by applying voltage to the corresponding row and column, whereas in active matrix operation each pixel can be addressed independently.

[182] Parker, I. D., Cao, Y. & Yang, C. Y. Lifetime and degradation effects in polymer light-emitting diodes. Journal of Applied Physics 85, 2441-2447 (1999).

[183] Cacialli, F., Friend, R. H., Moratti, S. C. & Holmes, A. B. Characterization of properties of polymeric light-emitting-diodes over extended periods. Synthetic Metals 67, 157-160 (1994).

List of Selected Symbols

α - Absorption

e - Electron charge

EA - Electroabsorption

EL - Electroluminescence

EM - Electromodulation

EP - Emitting polymer

ESA - Excited state absorption

E_g - Energy gap

f - The applied ac bias frequency

F8 - Poly(9,9-dioctylfluorene)

F_{BI} - The built-in electric field

F_0 - The total dc electric field in the polymer layer

F_{ac} - The sinusoidal electric field in the polymer layer

h - Planck's constant

HOMO - Highest occupied molecular orbital

LEP - Light-emitting polymer

LUMO - Lowest unoccupied molecular orbital

ITO - Indium tin oxide

OLED - Organic light-emitting diode

PEDOT:PSS - Poly(3,4-ethylene dioxythiophene) doped with poly(styrene sulfonate)

PF - Polyfluorene

PFB - Poly(9,9-dioctyl-fluorene-co-bis-N,N'-(4-butyl-phenyl)-bis-N,N'-phenyl-1,4-phenylenediamine)

PL - Photoluminescence

PLED - Polymer light-emitting diode

TFB - Poly(9,9-dioctylfluorene-co-N-(4-butylphenyl)-diphenylamine)

V_{ac} - Applied ac bias

V_{dc} - Applied dc bias

V_{BI} - The built-in voltage

V_{null} - The applied dc bias at which $\Delta T/T(1\omega)$ vanishes

W_F - Work function

ω - Ac bias frequency multiplied by 2π

ν - Photon frequency

$\mathrm{Im}\{\chi^3(\mathrm{h}\nu)\}$ - Imaginary part of the third order susceptibility

ϕ_B - Energy barrier at the polymer electrode interface

$\Delta T/T$ - The fractional change in transmission